Deployable Vibration Control Systems for Lightweight Structures

by

Kevin J. Goorts

A thesis
presented to the University of Waterloo
in fulfillment of the
thesis requirement for the degree of
Doctor of Philosophy
in
Civil Engineering

Waterloo, Ontario, Canada, 2019

Examining Committee Membership

The following served on the Examining Committee for this thesis. The decision of the Examining Committee is by majority vote.

External Examiner:	Shirley Dyke Professor of Mechanical and Civil Engineering Purdue University
Supervisor:	Sriram Narasimhan Professor, Department of Civil & Environmental Engineering University of Waterloo
Internal Members:	Carl Haas Professor, Chair, Department of Civil & Environmental Engineering University of Waterloo
	Giovanni Cascante Professor, Department of Civil & Environmental Engineering University of Waterloo
Internal-External Member:	Steven Waslander Associate Professor, University of Toronto Institute for Aerospace Studies and Adjunct Professor, Dept. of Mechanical & Mechatronics Engineering University of Waterloo

I hereby declare that I am the sole author of this thesis. This is a true copy of the thesis, including any required final revisions, as accepted by my examiners.

I understand that my thesis may be made electronically available to the public.

Abstract

The recent push towards lightweight, efficient, and innovative structural designs has brought forth a range of vibration control issues related to implementation, effectiveness, and control system design that are not fully addressed by existing strategies. In many cases, these structures are capable of withstanding day-to-day loads and only experience excessive vibrations during predictable peak-loading events such as large crowds or wind storms. At the same time, the use of lightweight material coupled with innovative construction methods has given rise to temporary structures which are designed to facilitate rapid implementation and intended for short-term applications. Both scenarios point towards a vibration control system that is suitable for immediate, short-term applications which motivates the concept of deployable autonomous control systems (DACSs).

The deployability aspect implies the control system is capable of being readily implemented on a range of structures with only minor customization to the structure or device while the autonomy aspect refers to the ability of the system to react to changes in the dynamic response and effectively control different structural modes of vibration. A prototype device, consisting of an electromagnetic mass damper (EMD) mounted on an unmanned ground vehicle (UGV) equipped with vision sensors and on-board computational hardware, is developed to study the vibration control performance and demonstrate the advantages of the DACS concept. Both numerical and experimental modelling techniques are used to identify system models for each component of the prototype device. Given the system models, the dynamic interaction between the device and underlying structure is derived theoretically and validated experimentally.

The use of an EMD and UGV introduce a number of practical challenges associated with controller design. These challenges arise due to the presence of physical operating constraints as well as uncertainty in the controller model. Three different candidate controllers, based on linear-quadratic Gaussian (LQG), model-predictive control (MPC), and robust H_∞ control theory, are formulated for the prototype device and comparatively assessed with respect to their ability to address these challenges. The MPC framework provides a systematic approach to incorporate physical operating constraints directly in the control formulation while robust synthesis of an H_∞ controller is well suited for addressing uncertainty in both the controller and structure models.

A key property of the prototype device is the ability to reposition itself at different locations on the structure. To study the impact of this mobility on the overall control performance, a

simultaneous localization and mapping (SLAM) solution is implemented for bridge structures. The SLAM solution generates a map of the structure that can later be used for autonomous navigation of the prototype device. In achieving autonomous mobility, the location of the control force can be added as an additional parameter in the controller formulation.

The overall performance of the prototype device is evaluated through a combination of numerical simulations and experimental studies. Real-time hybrid simulation (RTHS) is used extensively to study the dynamic interaction effects and evaluate the control performance of the prototype device on various structures. A full-scale modular aluminum pedestrian bridge is used to demonstrate autonomous navigation and assess the advantages of a mobile control device. The results from each study point towards DACSs as being a favourable alternative to existing control systems for immediate, short-term vibration control applications.

Acknowledgements

I am using this opportunity to reflect upon and express my gratitude to those who have supported, encouraged, and motivated the completion of this thesis.

First and foremost, I owe my deepest gratitude to my supervisor and mentor, Dr. Sriram Narasimhan. His guidance and expertise helped inspire and develop this research while his energy and mentorship provided steady motivation and prepared me for an academic career.

I am grateful to Dr. Oya Mercan for her insights and collaborations and would like to thank the committee members Dr. Shirley Dyke, Dr. Steven Waslander, Dr. Carl Haas, and Dr. Giovanni Cascante for their time in examining this work.

I am appreciative for the funding provided through the CGS-M and PGS-D programs sponsored by the Natural Sciences and Engineering Research Council (NSERC) that facilitated this research.

I would like to recognize the assistance and support from various past and current members of the Structural Dynamics, Identification, and Control (SDIC) lab; Mr. Ali Ashasi-Sorkhabi, for his assistance in experimental testing; Mr. Stephen Phillips, for his collaboration on implementing SLAM for the prototype device; Mr. Rajdip Nayek, for our countless theoretical discussions; Ms. Pampa Dey, for her encouragement and many shared commutes to campus; and of course my office mate, Mr. Guru Prakash who had a way of brightening any day. A special mention is also owed to Richard Morrison of the Structures Laboratory whose technical support and expertise in experimental testing is gratefully acknowledged.

Finally, I extend my sincerest gratitude to my family; my parents, who have supported, encouraged, and quietly prepared me to take on this journey right from the start; my three brothers, who kept me grounded and were always there when I needed a friend; and my parents-in-law, who shared positive energy and encouragement. I reserve my most heart-felt gratitude for my wife, Jacquelyn. Without her love, support, and patience, this journey would not have been possible.

Dedication

To Jacquelyn and my parents.

Table of Contents

List of Tables

List of Figures

Abbreviations

ACADO	automatic control and dynamic optimization
AMD	active mass damper
aMPC	adaptive model predictive control
AR	augmented reality
BIBO	bounded-input, bounded-output
cRIO	compact real-time input-output
CSI	control-structure interaction
DACS	deployable autonomous control system
DC	direct-current
DMA	direct memory access
DOF	degree-of-freedom
DSSF	discrete state-space formulation
EKF	extended Kalman filter
EMD	electromagnetic mass damper
ER	electrorheological
FPGA	field programmable gate array
FRF	frequency response function
GPS	global positioning system
HMD	hybrid mass damper
HSM	hydraulic service manifold

ICM	inverse compensation modelling
ICR	instantaneous center of rotation
IMU	inertial measurement unit
ISM	integrated systems modelling
LabVIEW	Laboratory Virtual Instrument Engineering Workbench
lidar	light detection and ranging
LQG	linear-quadratic Gaussian
LQR	linear-quadratic regulator
LTI	linear time invariant
LVDT	linear variable differential transformer
MDOF	multi-degree-of-freedom
MPC	model predictive control
MR	magnetorheological
NI	National Instruments
OpenNI	Open Natural Interaction
PAEI	phase-amplitude error indices
PD	proportional-derivative
PDF	probability density function
PI	proportional-integral
PIV	proportional-integral-velocity
RGB	red-green-blue
RMS	root mean square
RMSE	root mean squared error
ROS	robot operating system

RTHS real-time hybrid simulation

SDOF single degree-of-freedom

SDRE state-dependent Riccati equation

SEREP system equivalent reduction expansion procedure

SLAM simultaneous localization and mapping

SMC sliding mode control

TCP transmission control protocol

TMD tuned-mass damper

UGV unmanned ground vehicle

VI virtual instrument

Nomenclature

$\mathbf{A}$	state transition matrix
$\mathbf{B}$	input matrix
$\mathbf{C}$	damping matrix for MDOF structure
$\mathbf{C}$	output matrix
c_s	damping parameter of MDOF structure
c_u	UGV damping parameter
c_m	servo motor damping parameter
$\mathbf{D}$	direct feed-through matrix
$\boldsymbol{E}$	location vector indicating position of DACS
$\boldsymbol{F}_a$	Fourier transform of vector of applied forces
F_e	Fourier transform of EMD inertial force
F_t	Fourier transform of UGV tire force
f_e	EMD inertial force
f_t	UGV tire force
$G_{j,i}$	analytical transfer function model from i to j
$\mathbf{G}$	Jacobian of non-linear motion model
G_s	transfer function model for current loop in servo drive
H_I	transfer function model for feedback interaction dynamics
H_{LL}	lead-lag filter applied to experimental UGV transfer function model
$H_{j,i}^{min}$	minimum phase component of transfer function model from i to j

$\tilde{H}_{j,i}$ uncertain transfer function model from i to j

$H_{j,i}$ experimental transfer function model from i to j

$\mathbf{H}$ Jacobian of non-linear measurement model

h_{enc} measurement model for UGV encoder

h_{knct} measurement model for Kinect sensor

h_m control horizon for the MPC formulation

h_p prediction horizon for MPC formulation

$\mathbf{K}$ stiffness matrix for MDOF structure

$\tilde{K_f}$ estimated motor force constant

K_f motor force constant

$\mathbf{K}_s$ Kalman gain for EKF-SLAM

K_g controller model for generalized plant model in H_∞ control

K_{IV} integral gain for velocity loop

$\boldsymbol{K}_c$ LQG state-feedback control gain

K_{nn} H_∞ controller based on nominal structure model and nominal DACS model

K_{nr} H_∞ controller based on nominal structure model and uncertain DACS model

K_{PP} proportional gain for position loop

K_{PV} proportional gain for velocity loop

K_{rr} H_∞ controller based on uncertain structure model and uncertain DACS model

k_s stiffness parameter of MDOF structure

k_u UGV stiffness parameter

$\mathbf{M}$ mass matrix for MDOF structure

m_m servo motor mass

m_s mass parameter of MDOF structure

m_u UGV mass parameter

P_c Fourier transform of EMD position command

P_g generalized plant model for H_∞ control

$\mathbf{P}^{rr}$ covariance of the robot pose states

$\mathbf{P}$ covariance of the probability distribution on the state vector for EKF-SLAM

p_c EMD position command

$\mathbf{Q}$ covariance matrix for measurement noise

$\boldsymbol{R}_a$ vector of restoring forces from analytical substructure

$\mathbf{R}$ covariance matrix for process noise

R_e restoring force from experimental substructure

S_{p_c} sensitivity function on control input

$S_{j,i}$ weighting function for uncertainty in transfer function model from i to j

$S_{\boldsymbol{\omega}}$ sensitivity function on external input

$S_{\boldsymbol{\nu}}$ sensitivity function on measurement noise

$S_{\boldsymbol{y}_s}$ sensitivity function on structural output

$\bar{\boldsymbol{u}}$ optimal control input vector

$\boldsymbol{u}$ control input vector

$\boldsymbol{u}_g$ vector of control inputs for H_∞ control

$\boldsymbol{W}$ Fourier transform of external disturbance

$\mathbf{W}_f$ weighting matrix penalizing UGV tire force

$\mathbf{W}_\infty$ weighting matrix penalizing non-zero terminal states

$\mathbf{W}_{\boldsymbol{u}}$ weighting matrix on non-zero control input

$\mathbf{W}_{\boldsymbol{z}}$ weighting matrix on non-zero states

$\boldsymbol{w}$ vector of external disturbance

$\boldsymbol{X}_s$ Fourier transform of displacement vector for MDOF structure

X_u Fourier transform of UGV displacement when modelled as a SDOF system

$\bar{\boldsymbol{x}}^m$ known state vector of map features for EKF-SLAM

$\boldsymbol{x}^m$ state vector of map features for EKF-SLAM

$\bar{\boldsymbol{x}}^r$ known robot pose state vector for EKF-SLAM

$\boldsymbol{x}^r$ robot pose state vector for EKF-SLAM

x_g^i global x-coordinate of the i^{th} feature

x_g^r global x-coordinate of UGV's center of mass

$\hat{\boldsymbol{x}}^r$ mean robot pose state vector for EKF-SLAM

$\boldsymbol{x}$ state vector for EKF-SLAM

x_{ICR} projection of the ICR on the local x-axis

$\boldsymbol{x}_g$ generalized state vector for H_∞ control

$\hat{\boldsymbol{x}}$ mean of probability distribution on the state vector for EKF-SLAM

$\boldsymbol{x}_s$ displacement vector for MDOF structure

x_{u_r} relative displacement of UGV when modelled as a SDOF system

x_u displacement of UGV when modelled as a SDOF system

$\boldsymbol{Y}_s$ Fourier transform of structural response vector

y_g^i global y-coordinate of the i^{th} feature

y_g^r global y-coordinate of UGV's center of mass

$\boldsymbol{y}$ measurement vector for EKF-SLAM

$\boldsymbol{y}_g$ vector of measured outputs for H_∞ control

$\boldsymbol{y}_s$ structural response vector

$\hat{\boldsymbol{z}}$ estimate of state vector

$\boldsymbol{z}_g$ vector of regulated outputs for H_∞ control

$\boldsymbol{z}$	state vector
α_h	tunable rate parameter for the high utilization metric in the MPC scheme
α_l	tunable rate parameter for the low utilization metric in the MPC scheme
δ_x^i	global x-component of distance to the i^{th} feature
δ_y^i	global y-component of distance to the i^{th} feature
$^\circ$	degrees
γ_g	measure of optimality for sub-optimal H_∞ controller design
γ_b^i	sensor bearing measurement to the i^{th} feature
γ_r^i	sensor range measurement to the i^{th} feature
λ_h	EMD position defining threshold for high utilization
λ_l	EMD position defining threshold for low utilization
ψ_g^r	heading of UGV measured from global x-axis
ρ_{p_c}	gain for control input sensitivity weighting function
$\rho_{\boldsymbol{\omega}}$	gain for input sensitivity weighting function
$\rho_{\boldsymbol{\nu}}$	gain for measurement noise sensitivity weighting function
$\rho_{\boldsymbol{y}_s}$	gain for output sensitivity weighting function
θ_h	metric for monitoring high device utilization in MPC
θ_l	metric for monitoring low device utilization in MPC
ν_x	forward velocity command for UGV
$\boldsymbol{\nu}$	vector of measurement noise
ν_y	y-component of the UGV velocity in the local reference frame
ω_g	angular velocity command for UGV
$\boldsymbol{\omega}$	vector of process disturbances
$\boldsymbol{\omega}_g$	vector of exogenous input for H_∞ control

GHz	gigahertz
GPa	gigapascal
Hz	hertz
L/min	liters per minute
MPa	megapascal
N	newtons
kHz	kilohertz
kN	kilonewtons
kg	kilograms
m/s^2	meters per second squared
m/s	meters per second
m^2	square meters
mm	millimeters
ms	milliseconds
m	meters
pulse/m	pulses per meter
s	seconds

Chapter 1

Introduction

Over the past decade, a number of seemingly independent factors have synergized to produce the current momentum towards lightweight, efficient, and aesthetically pleasing structures. These factors include recent advances in lightweight materials, recognition for potential cost savings, innovations in construction techniques, and societal pressures regarding modern built environments. A well-known consequence of this shift is an increase in the complexity associated with structural design. In general, structures are designed based on a strength criterion intended to address the safety of the structure under extreme loads as well as a serviceability criterion focusing on the comfort of humans during everyday use. Unlike the design of traditional rigid structures which is generally governed by the strength criterion, the design of many lightweight, flexible structures is dictated by the dynamic behaviour and serviceability criterion. The reduced self-weight and increased flexibility - due to the use of lightweight materials and slender designs - reduces the inherent system level damping and decreases natural frequencies resulting in structures that are prone to excessive vibrations. Common approaches to reduce vibrations involve increasing the stiffness of the structure or enhancing the vibrational dissipation capacity. Increasing stiffness can be achieved through the use of additional or larger structural elements, however this directly opposes the direction of current design trends. Alternatively, auxiliary damping devices can be utilized to dissipate energy and thus increase the overall damping of the structure [1].

Existing auxiliary damping devices can be broadly categorized as passive, active, or semi-active systems [2]. Passive control devices impart control forces that are developed in response to the motion of the structure. A truly passive system does not require any external power

and cannot add energy to the system thereby ensuring bounded-input, bounded-output (BIBO) stability [3]. However, since energy dissipation is only achieved by responding to the motion of the structure, the effectiveness of passive devices is limited to a narrow frequency range of vibration [4]. Active control devices utilize an external power source to control actuators that apply forces to the structure according to a feedback and/or feed-forward control algorithm [3]. Relative to passive devices, active systems offer enhanced effectiveness and the ability to select a broader control objective; however, these systems are generally more expensive and less reliable [3, 5]. Semi-active devices are often described as passive systems with controllable properties. By using small amounts of external power, semi-active control devices can adjust certain properties allowing them to achieve higher control efficiency relative to similar passive devices [2]. Since external power is only used to tune the damper properties, no mechanical energy is added to the system thereby maintaining high reliability and guaranteeing stability [3]. In general, the performance of any auxiliary control device depends on a number of factors including loading conditions, structural properties, and control system design [4].

Structural control is a relatively mature field of research with a vast range of control devices and controller formulations covered in the literature [2, 3, 6, 7]. Nevertheless, the current trend towards lightweight, flexible structures has raised several new issues related to implementation, effectiveness, and control system design not fully addressed by existing strategies. In many cases, lightweight structures are capable of withstanding day-to-day loads and only experience excessive vibrations during predictable peak-loading events such as large crowds or wind storms. Designing such structures to sustain extreme loading events without the use of auxiliary vibration control greatly diminishes the design efficiency. Furthermore, although the use of existing vibration control devices may facilitate more economical designs, these devices are likely to suffer from under-utilization, particularly if the devices are only triggered by the specific design level event. On the other hand, the use of lightweight materials coupled with recent innovations in construction methods has given rise to temporary structures, such as modular aluminum pedestrian bridges, which are specifically designed to facilitate rapid implementation and are intended for short-term applications. In this case, the need for vibration mitigation depends on the end-use of the structure and as such, existing permanent vibration mitigation measures may be considered uneconomical or impractical. These scenarios highlight two new vibration control problems fueled by the recent push towards lightweight, flexible structures. In both cases, the underlying structure would benefit greatly from a vibration control system suitable for immediate, short-term applications.

1.1 Motivation

The suitability of existing structural control strategies for immediate, short-term applications is hindered by the time and effort associated with the design process, the need for a fixed, rigid connection, and the nature of the devices to be permanently integrated with the structure. For example, the construction of a pre-designed modular structure requiring auxiliary damping given the particular usage would be delayed by the time required to design a suitable control device. Furthermore, given existing control devices rely on a rigid connection to impart control forces, the pre-designed structure will likely need to be modified to accommodate the device which is uneconomical for short-term applications. These limitations motivate the concept of deployability. A deployable control system is one which is readily available to be implemented on a range of structures with relatively minor customization such as tuning and sizing of the device. Achieving deployability nearly eliminates design time, reduces costs, and facilitates rapid construction of temporary structures.

The high dynamic sensitivity of lightweight structures requires special attention in control system design as minor changes in loading conditions or structural properties could have significant impacts on the dynamic response [8]. The ideal control strategy will have sufficient robustness and adaptability to respond to these changes accordingly. Despite considerable efforts to increase the adaptability of control devices, the common limitation across all existing applications stems from the fact that the device is fixed in position on the structure and thus has restricted controllability on certain structural properties. The need for adaptability and the desire to have a single device control different structural properties (i.e., modes of vibration) motivates the concept of autonomy. An autonomous control system is one which has the capacity to suppress a relatively wide bandwidth of vibrations and the mobility to change positions on the structure based on the dynamic response.

In summary, the vibration mitigation challenges brought forward by flexible or temporary structures motivate the novel concept of deployable autonomous control systems (DACSs). Recent advances in emerging fields such as robotics and technology present a unique opportunity to develop this concept and advance the state-of-the-art of structural control.

1.2 Research aims

Given the aforementioned background and motivation, the overarching research aims of this thesis are summarized as follows:

- Establish the notion of DACSs as a favourable alternative to existing control devices when targeting immediate, short-term vibration control applications.
- Address the theoretical and practical challenges associated with DACSs including controller formulation in the presence of physical constraints and/or model uncertainty, accurate representation of dynamic interaction effects, and achieving autonomous navigation on unknown structures.
- Demonstrate, through the use of a prototype system, the advantages of deployability and mobility when controlling various structural properties on a range of full-scale structures.

1.3 Overall methodology

The overall methodology for achieving these objectives is summarized in the following five-step procedure:

1. Identify the physical requirements for achieving deployability and autonomy in vibration control systems.
2. Develop a small-scale prototype DACS for experimental testing and validation.
3. Investigate various controller formulations to address the unique challenges brought on by the DACS concept.
4. Implement a suitable autonomous navigation algorithm for the prototype device to assess the impact of mobility on control systems.
5. Conduct experimental testing to investigate the overall control performance of DACSs and validate the controller formulations.

By establishing definitions for deployability and autonomy in the context of vibration control systems, the central components required for any DACS can be identified. Equipped with this information, a prototype device is developed by integrating a number of off-the-shelf components to minimize customization. The prototype DACS plays a central role in this thesis and is used to investigate controller formulations, study dynamic interaction effects, demonstrate autonomous navigation, and ultimately evaluate the advantages of deployability and autonomy in control devices. Based on a survey of existing controller formulations, three candidate controllers are formulated to address the challenges associated with DACS. The suitability and limitations of each control method are assessed through theoretical and experimental studies. Given this set of controllers, the impact of autonomy is then assessed by augmenting the control design to account for device mobility. A combination of full-scale experiments and hybrid testing is conducted to reveal the overall control performance of the prototype device. Finally, the results from this testing are used to make inferences regarding the advantages and suitability of the DACS concept.

1.4 Thesis organization

This thesis contains eight chapters and is organized as follows:

- **Chapter 1** provides a brief introduction and motivation for the DACS concept along with a summary of the research aims and methodology followed in this thesis.
- A detailed literature survey on the state-of-the-art of structural control, specifically related to active vibration control systems is presented in **Chapter 2**. The various classes of existing vibration control devices are reviewed first, followed by commonly used feedback control methods for active systems. The use of robotic systems in civil engineering applications is also reviewed in this chapter with particular emphasis on vibration control applications. The chapter concludes by highlighting specific gap areas in the existing literature to underscore the importance of the proposed research objectives.
- **Chapter 3** provides definitions for deployability and autonomy and details the development of the prototype DACS. Potential applications and possible implementations for the prototype are discussed to further motivate the DACS concept.

- The methodology used to characterize the dynamics of the prototype DACS is presented in **Chapter 4**. The system models – needed for controller design – are identified through experimental testing and analytical derivation. An experimental study is conducted to evaluate the accuracy of the identified models.

- **Chapter 5** provides an overview of the general control strategy. After establishing a model for the dynamic coupling between the structure and prototype control device, the theoretical formulation of three different feedback control algorithms is presented along with specific implementation details and limitations.

- In order to study mobility in vibration control systems, **Chapter 6** presents an augmented control strategy to include device positioning as well as the theoretical formulation for achieving autonomous navigation. The proposed method for autonomous navigation on unknown structures is demonstrated on a full-scale pedestrian bridge.

- **Chapter 7** details the numerical simulations and experimental testing conducted to evaluate the overall control performance of the prototype device and compare the effectiveness of the various control formulations.

- Finally, the main conclusions from this research are discussed in **Chapter 8**. The main contributions of this thesis are summarized and several recommendations are provided to extend the present work.

Chapter 2

Background

This chapter provides relevant background information on vibration control and robotic systems to position the research objectives in the context of existing practices and the current state-of-the-art. First, an overview of the current state-of-the-art of structural control is presented. This review is divided into two parts such that the different types of control devices are presented first followed by a discussion on the various control methodologies that have been successfully implemented in structural control applications. Next, the control-structure interaction (CSI) phenomenon is described and the various modelling approaches that have been developed to address these interaction effects are discussed. Finally, a summary of the current implementations of robotic systems for civil engineering applications is provided. This discussion places emphasis on vibration control devices that have utilized robotics and is extended to provide relevant background information on autonomous navigation in unknown environments.

2.1 State-of-the-art of structural control

Nearly three decades ago, the concept of structural control became widely accepted as a promising technology in the design of new structures and retrofitting of existing structures subjected to earthquakes and/or wind loads [3, 9]. Since then, wide-spread efforts have been undertaken to develop the structural control concept into a workable technology [2]. The roots of structural control originated in aerospace related problems involving flexible space structures. Once es-

tablished, the technology transitioned quickly to issues related to civil infrastructure such as the protection of buildings and bridges against extreme loads and ensuring human comfort [3]. The rapid progress of structural control for civil infrastructure was driven by simultaneous research in multiple fields including development of control strategies [5, 10–12], advancing technology for control devices [3, 13], techniques for structural system modelling, and experimental testing methods [14, 15]. Despite the successful implementation of various control devices and adoption of numerous control methodologies, the control of civil engineering structures is still an open and active field to theoretical research and practical application.

Since the initial conceptual study by Yao [16] in 1972, researchers have collectively formulated a wide range of control strategies and amassed a vast collection of devices. These efforts have resulted in the successful implementation of numerous types of control devices to address the design needs of both buildings and bridges. The current research in structural control is largely focused on leveraging recent technological advancements to enhance control strategies and to develop new control devices [17, 18]. As civil infrastructure continues to evolve, the vibration control problem must be revisited to ensure that both current and future needs and issues are addressed.

The past and present research on structural control can be sorted into four categories: passive control, where energy is dissipated by responding to the motion of the structure, active control, in which external energy is applied to the structure, semi-active control where low levels of energy are used to improve the overall energy dissipation, and hybrid control which combines the properties of two or more categories. The advantages, limitations, and current-state of each category are discussed next.

2.1.1 Passive control systems

Passive systems are characterized by their capability to enhance energy dissipation in the absence of an external energy source. The two general approaches used in passive devices for dissipating vibrational energy are based on the conversion of kinetic energy to heat and transfer of energy amongst other vibrational modes. Devices that involve frictional sliding, yielding of metals, or deformation of viscoelastic materials fall under the energy conversion approach while the method of moving fluid through orifices or the use of additional oscillating devices are categorized as energy transfer approaches. The tuned-mass damper (TMD) is the most commonly used passive

device [3]. This oscillatory system dissipates energy by producing a relative motion within the control device with respect to the structure motion and as such does not impact the overall system stability. In its simplest form, a TMD is an auxiliary mass connected to the structure via tuned stiffness and damping elements. The damper is generally tuned to be out of phase with a particular structural frequency such that energy in the given mode of vibration is transferred to the motion of the oscillating mass [1]. TMDs are commonly tuned to the structure's dominant modal frequency to protect the structure from resonance. While energy is reduced at the tuned frequency, the response may increase at other frequencies, effectively turning a single lightly-damped mode into two coupled and highly damped modes [1]. A limitation shared by all TMD systems is the lack of robustness to detuning [4, 19]. As a result, the effectiveness of TMDs at reducing vibrations diminishes rapidly outside of a narrow frequency band centered on the frequency in which the device is tuned. Even small deviations from the optimal tuning frequency can deteriorate the performance significantly and thus there is considerable importance associated with the initial design.

Despite this limitation, passive TMD systems are still widely used largely because they are relatively inexpensive systems that perform well when property tuned [17]. Furthermore, the absence of an external power source means there are no additional operating costs and minimal maintenance requirements once the system is installed. The use of TMD systems is particularly useful in structures such as tall buildings or suspension bridges, where resonant conditions coincide with external excitation frequencies. Presently, TMDs have been implemented on a number of well-known structures. For example, the John Hancock tower in Boston employs translational TMDs on the fifty-eighth floor to suppress wind-induced sway and torsion [1]. Similarly, Taipai 101 – a 101-storey tower in Taiwan – reduces vibrations using a 5000 tonne pendulum TMD suspended in the center of the building [20]. Furthermore, landmark bridges such as the Millennium bridge in London [21] and the Akashi Kaikyo bridge in Japan [22] employ multiple TMDs to suppress traffic and wind-induced vibrations.

Other passive control systems that have been implemented for vibration control of civil infrastructure include tuned liquid dampers which absorb energy through viscous actions of the fluid and wave breaking [23], viscoelastic dampers that dissipate energy through shear deformation [24], and viscous fluid dampers which consist of a piston immersed in a viscoelastic fluid [25]. Metallic yield dampers and friction dampers have also been implemented for seismic protection purposes [3].

2.1.2 Active control systems

Active control systems are characterized by the use of an external power source to control one of more actuators that apply forces to the structure in a prescribed manner [3]. A typical active control system consists of three main components: (i) a monitoring system to measure the global structural response and/or external excitation; (ii) a control algorithm to process the measured information and determine the control force; and (iii) an actuation device to apply the control force to the structure. The working principle of active control systems is that given measurements of the structural response, the control algorithm will determine the optimal control signal to attenuate the vibration. Based on this control signal, control actuators placed in pre-determined locations on the structure generate a secondary vibrational response which in effect reduces the overall structural response [26]. Unlike passive systems which only generate forces in response to the structure's motion, active systems are capable of exerting forces that can be used to both add and dissipate energy in the structure. As such, system stability is an important consideration in controller design.

Active devices have demonstrated superior control performance compared to passive systems. This is largely due to their capacity to effectively suppress a wide frequency range and also control the transient vibration response [4]. Nevertheless, in order to achieve this increased performance, more complex control strategies involving sensors and controller hardware must be designed. In all active devices, a trade-off exists between the level of control performance and system stability. This trade-off addresses the fact that incorrectly modelled dynamics or changes to the structural properties may lead to an unstable condition whereby unbounded energy is specified by the controller [27]. In some cases, the effectiveness of active systems is further limited by the energy available to develop the magnitude of forces required to control civil infrastructure. The dependence on external power also draws criticism regarding reliability. During a power outage, which commonly occurs during seismic events, active devices are rendered useless.

Active mass dampers (AMDs) and active tendons are examples of active devices that have been used for vibration control of civil infrastructure. These devices have been developed with many different actuators including hydraulic or pneumatic pistons, electromagnetic motors, and ball-screw drives [3]. The first full-scale application of active control was in 1989 and involved two AMDs to reduce wind induced transition and torsion of the Kyobashi Seiwa building in Tokyo, Japan [28]. More recently, the use linear and torsional servo motors in AMDs has been

given particular attention due to their fast response and effectiveness in seismic applications [29, 30]. Nevertheless, aside from a small number of AMD applications, the implementation of purely active systems has been limited due to the increased complexity and large costs. For example permanent installations require a continuous power supply and routine maintenance to ensure proper operation. In light of these limitations, much of the effort on active control shifted to hybrid mass dampers (HMDs) which incorporate an active device with a passive TMD to increase the overall reliability and efficiency of the controlled structure [2]. Although the use of relatively small active components may reduce the costs and overall complexity, some large-scale HMDs still suffer from the drawbacks associated with active devices. Further details on HMDs are provided later in the discussion on hybrid control systems. It is worth noting that the major drawbacks of active control systems, namely cost, and complexity are much less significant in short-term control applications.

2.1.3 Semi-active control systems

Semi-active control systems combine the best features of both passive and active control devices to yield an attractive alternative to fully passive or fully active systems. By definition, semi-active control devices cannot inject mechanical energy into the structure but do make use of external power to tune various properties of the device in an effort to increase performance [9]. In many cases the external power requirements for semi-active systems can be achieved using batteries making these devices more reliable than active systems. Furthermore since energy is not injected directly into the system, semi-active devices do not have the potential for destabilizing the structure from an unbounded control perspective. The working principle of semi-active control devices is to dissipate energy in a similar fashion to passive devices yet maintain the ability to adapt or modify certain properties to improve performance. The reliability and effectiveness offered by the passive component coupled with adaptability facilitated by an active component was the main motivation driving the development of semi-active devices.

The adaptable properties allow semi-active systems to perform significantly better than passive devices and create the potential to reduce a wide frequency bandwidth of structural responses [4, 9, 13]. In some cases the performance of semi-active devices approaches that of fully active systems with considerably less energy requirements. Examples of semi-active devices that have been developed for vibration control of civil infrastructure include: variable-orifice fluid dampers

[3], variable-stiffness devices [3], semi-active TMDs [2], electrorheological (ER) dampers [31], and magnetorheological (MR) dampers [32].

2.1.4 Hybrid control systems

Hybrid control strategies are motivated by the potential to increase the overall reliability and efficiency of the controlled structure by combining passive and active devices [3, 33, 34]. Since multiple control devices are operating simultaneously towards a common goal, hybrid control systems alleviate a number of the limitations that arise when each system acts independently. For example, in the event of power failure, vibration control will still be provided by the passive component. A key advantage of hybrid systems is that a portion of the vibrational energy is transferred to the passive device which reduces the power requirement for the active component. The trade-off with hybrid control systems comes in the form of controller complexity. Although higher levels of performance are achievable, the required control system design is often more complicated. The vast majority of full-scale implementations involving some form of active control have been hybrid control systems, and more specifically, HMDs [2]. The HMD consists of a TMD and an active control actuator. The premise of this design is to use forces from the control actuator to increase the efficiency of the HMD and improve its robustness to changes in the dynamic characteristics of the structure. Since the natural motion of the TMD is the primary source of energy dissipation, the energy and forces required to operate an HMD are considerably less than those associated with a fully active system of comparable performance [3]

A well-known example of a HMD is the active-passive composite tuned mass damper referred to as DUOX [35]. The DUOX system was developed at Kajima Corporation in Tokyo, Japan and consists of an AMD mounted on a TMD [35]. In this configuration, the active system is intended to improve the sluggish response time and reduce the braking time of the passive system.

2.2 Structural control algorithms

While a number of researchers focused on the development of various control devices, considerable attention was also given to the formulation of various control algorithms which play a central role in active, semi-active, and hybrid systems. Some of this work involved the direct

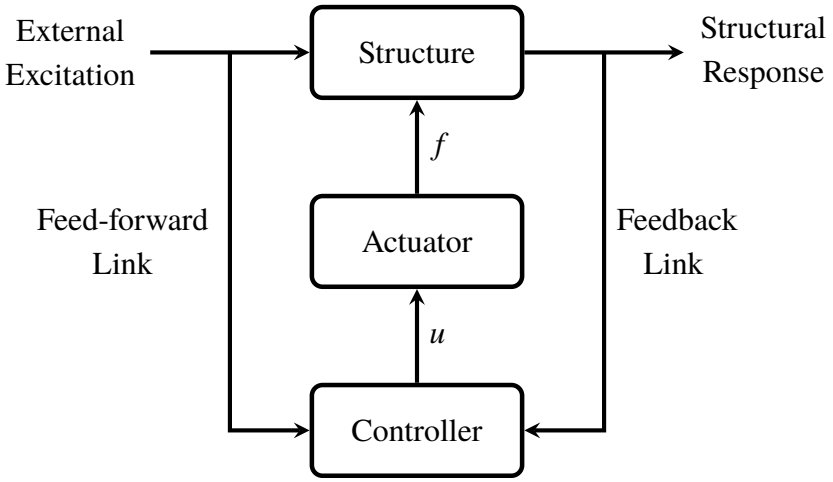

Figure 2.1: Overview of the active structural control problem

application of established control theory from other engineering disciplines while other works proposed new algorithms designed specifically for vibration control of civil infrastructure [6]. In general, structural control algorithms use measurements of the structure's response and/or knowledge of the excitation to determine the input for the control device. Figure 2.1 provides a schematic of the general active control problem for civil infrastructure. Both control paradigms, referred to as feed-forward control and feedback control, are shown in the schematic; however, the implementation of either loop depends on the ability to measure the external excitation and structural response respectively. In most cases, the external excitation is unknown and thus only the feedback loop is present. Nevertheless, a common exception is the case of seismic protection where the ground acceleration can also be measured. The suitability of a given control algorithm depends on many factors including the type of structure, presence of uncertainty in the controlled system models, and availability and accuracy of sensor measurements. In an effort to address these factors, many different control algorithms have been developed, each with their respective advantages and limitations. Despite the wide range of algorithms, most controllers are derived based on one of three control approaches: optimal control, predictive control, and robust control. The premise of each control approach and their respective applications in civil infrastructure is presented next.

2.2.1 Optimal control

Generally speaking, the term *optimal control* can apply to any stabilizing controller that is optimal based on some arbitrary criterion; however, in the context of structural control, optimal control usually refers to controllers that minimize a quadratic performance index (i.e., objective function). In most cases, the objective function is designed to maximize performance with consideration for the required control effort. The most fundamental and widely used optimal controller is the linear-quadratic regulator (LQR) [36]. When implementing an LQR controller for structural control applications, the system states and control input are used as parameters in the performance index which takes the following form:

$$J = \int_0^\infty \left(\boldsymbol{z}^T(t)\mathbf{W}_z \boldsymbol{z}(t) + \boldsymbol{u}^T(t)\mathbf{W}_u \boldsymbol{u}(t) \right) dt \tag{2.1}$$

The matrices $\mathbf{W}_z$ and $\mathbf{W}_u$ represent penalty weights on the state vector $\boldsymbol{z}$ and control input $\boldsymbol{u}$ respectively. The weighting matrices are tuned to obtain the desired control performance under the condition that $\mathbf{W}_z$ is positive semi-definite and $\mathbf{W}_u$ is positive definite. An objective function of this form is minimized using state-feedback control. As such, the optimal control input is a linear function of the state vector defined by the gain matrix $\boldsymbol{K}_c$ as:

$$\bar{\boldsymbol{u}}(t) = \boldsymbol{K}_c \boldsymbol{z} \tag{2.2}$$

A limitation of LQR optimal control is the requirement that all states are available to determine the control input. In structural control applications this is often impractical given the required number of sensors and difficulty in measuring displacements and/or velocities. In most cases, the states of the structure can be estimated indirectly from a subset of acceleration measurements by implementing a Kalman filter [37]. The addition of a Kalman filter to an LQR control algorithm leads to the linear-quadratic Gaussian (LQG) optimal controller. The principle of separation of estimation and control (i.e., separation principle) plays a key role in LQG optimal control by guaranteeing that these two systems, namely the Kalman filter (i.e., linear quadratic estimator) and LQR controller can be designed independently and combined [36]. In LQG control, the estimated states $\hat{\boldsymbol{z}}$ are treated as the actual states for the minimization resulting in optimal control inputs given by:

$$\bar{\boldsymbol{u}}(t) = \boldsymbol{K}_c \hat{\boldsymbol{z}}(t). \tag{2.3}$$

An important distinction between LQR and LQG is the assumption of additive Gaussian white noise disturbance in the LQG controller formulation that can be scaled to represent external

forces. In practical applications the frequency content of the excitation is generally unknown *a priori*; however, in the event a structure is subjected to narrow-band excitation, a band-pass filter can be incorporated into the structure model to improve the overall performance. This process is analogous to the implementation of Kanai-Tajimi filters which are used to account for the frequency content of seismic excitation [38]. The main criticism of the LQG optimal control algorithm is the challenge associated with tuning the objective function to achieve the designed performance. Although the framework is set up to balance the trade-off between control performance and robust stability, identifying appropriate weighting matrices is complex and often performed using a trial-and-error approach. Furthermore, in addition to maximizing control performance, consideration must be given to ensure the control device operates within its physical limitations. These operating constraints are not formally addressed in the optimal control algorithm and thus must be accounted for indirectly by tuning the weighting matrices accordingly. Despite these short-comings, the simplicity of the formulation and high performance when properly tuned has motivated the use of LQG controllers in several active and semi-active structural control applications [6, 39].

2.2.2 Predictive control

The concept of predictive control, introduced in the mid 1970's, gained considerable popularity through various applications in the processing industry before being applied to civil engineering applications in 1987 [40, 41]. The premise of predictive control is to apply the appropriate control action such that the predicted output of the system approaches a pre-determined desired response. When a model of the system dynamics is used explicitly to predict the future behaviour of the system, the method is referred to as model predictive control (MPC) [40]. Given a model of the system, a sequence of optimal control inputs is determined by solving a constrained finite-horizon optimization problem where the finite horizon is equal to the length of the predicted response. Although the solution to the optimization problem yields a sequence of control inputs, a receding horizon approach is generally adopted in which only the first control action is applied to the system and the optimization is repeated in the subsequent time step after incorporating new measurement information. Given the optimization is based on the predicted response, the prediction model and state estimator, used to forecast the future behaviour of the system, are central to the effectiveness of the MPC scheme. Furthermore, a key feature of MPC is that the prediction for the instant

$k+1$, necessary to establish the control action $\boldsymbol{u}(k+1)$, is made based solely on the measured response and control input at the previous time instant k. In structural control applications, the optimization problem is typically characterized by a quadratic performance index subject to constraints [42]. As such, MPC is often viewed as an extension to the LQG control problem [43]. In fact, the use of a linear objective function in the absence of constraints reduces the solution of the MPC problem to an LQG controller. Nevertheless, the ability to formally address operating constraints directly in the controller formulation is a distinct advantage of MPC.

Several studies have investigated the performance of various MPC configurations for structural control applications. For example, Mei et al. [44] combined feed-forward and feedback components to improve performance under earthquake excitation and later demonstrated an application of MPC with acceleration feedback on a scaled 2-storey model [45, 46]. More recently Johnson et al. [47] studied the performance and robustness of hybrid MPC for controllable dampers in building models. Nevertheless, the heavy computational requirements is a significant drawback which has limited the application of MPC to relatively small systems with slow dynamics. The computational demands have recently garnered attention from various researchers aiming to implement MPC on large-scale structures. Yang et al. [48] proposed a direct output feedback method based on the modified predictive controller by Chung [49] which reduces online computation by deriving linear relationships between control actions and predictive output signals. The trade-off in this case is the inability to handle operating constraints since the linear relationships are determined *a priori*. Other studies have proposed alternative formulations to the quadratic programming problem however these have yet to be verified experimentally [50, 51]. Despite these efforts, the practical challenges of implementing MPC for structural control applications have yet to be fully resolved with only a few cases demonstrating experimental validation [45, 52]. Furthermore, nearly all applications of MPC for structural control have, at most, incorporated constant hard constraints on controlled variables and the use of soft constraints on system states or outputs has yet to be explored.

2.2.3 Robust control

In all practical applications, there is some level of uncertainty associated with the mathematical model of the controlled plant and the exogenous inputs to which it is subjected. This is certainly true for civil infrastructure which is often modelled based on a number of simplifying assumptions

and has dynamic properties that may change over time due to aging or variation in operating conditions. As such, the premise of robust control is to address the issues of performance and stability in the presence of uncertainty through controller design. The uncertainty is generally expressed as bounds on the variation in frequency response or as parametric variations of the plant model. A system is robustly stable if the closed-loop system is stable for any plant model that lies within the specified uncertainty set. Similarly, the controller is said have robust performance if the closed-loop system satisfies a given performance criterion for any and all plant models in the uncertain set [53]. Most implementations of robust control for structural applications are based on H_∞ control theory. The basic principle of the H_∞ design method is to find a control law such that the infinity norm of the transfer function from exogenous inputs to regulated outputs is below a prescribed value. As such, any uncertainty in the plant model can be addressed directly in the controller formulation. Since the H_∞ design method is based in the frequency domain, frequency-dependent weighting functions are added to the plant model to achieve the desired performance [27]. For example, applying weighting functions on the structure's response and control input make it possible to control a specific frequency range and balance the trade-off between control performance and robust stability. Nevertheless, the frequency domain modelling increases the complexity of achieving time domain specifications such as saturation constraints and still requires tuning through trial-and-error to ensure the control devices operates within the specified physical constraints.

H_∞ controllers have been applied to several active structural control applications dating back to 1990 [54]. Some of the earliest applications of H_∞ control theory involved large structures subjected to earthquakes [55–57] and wind-excited buildings [58, 59]. More recently, researchers have attempted to overcome some of the challenges associated with frequency domain modelling. For example Li and Adeli [60] has proposed a new H_∞ algorithm using linear matrix inequalities such that the uncertainties of structural parameters can be considered in the time domain opposed to the frequency domain. Meanwhile, Zhou et al. [61] studied the combination of H_∞ control theory with MPC to incorporate physical operating constraints in the optimization.

2.2.4 Alternative control methods

Several other control algorithms have been implemented for various structural control applications. In most cases, these algorithms are extensions of the optimal or robust control framework

and target specific aspects of the control problem. A few of the more popular methods include clipped control, bang-bang control, sliding mode control, state-dependent Riccati equation (SDRE) control, as well as fuzzy logic control and neural network control. A brief summary of each method is provided next.

Sliding mode control: Sliding mode control (SMC) is a form of robust control where the controller is designed to drive the system response on to a sliding surface. The sliding surface is obtained by minimizing a performance function and defined such the response is stable on the surface. The studies by Singh et al. [62] and Adhikari and Yamaguchi [63] were key in introducing SMC to structural control applications. Recent research efforts aim to enhance performance and robustness through various modifications [64, 65].

Clipped-optimal control: Initially proposed by Dyke et al. [32] for use with the MR damper, the clipped-optimal control approach involves designing a linear optimal controller that calculates the desired control force based on the measured force applied to the structure in addition to the measured structural responses. This approach has been shown to be effective for semi-active systems, particularly MR dampers where the force generated in the damper is dependent on the responses of the structural system [66].

Bang-bang control: The premise of bang-bang control is abruptly switching the device states between two extreme cases (i.e., off and on) to achieve a specified control objective. The advantage of a bang-bang algorithm is that maximum control efforts can be exploited since the control force always takes its maximum values. However, there are practical limitations when it comes to structural control since many existing devices, specifically servo-hydraulic actuators, can't follow this high-speed switching. Nevertheless, ER and MR dampers are well suited for bang-bang control applications due to their fast response times [67, 68].

State-dependent Riccati Equation methods: SDRE techniques are general controller design methods that provide a systematic and effective means for designing non-linear controllers [69]. In general, the SDRE method involves solving the traditional LQR control problem at each time iteration (i.e., in real-time) such that the weighting matrices, prescribed in the LQR objective function, can be updated to more heavily penalize state variables as they approach predefined limits. This approach ultimately results in state-dependent gain matrices, or in other words, non-linear control strategies [70]. The main limitation of the SDRE approach is the inability to directly incorporate constraints on the control input [69]; however, this method has been adopted to address the issue of actuator saturation [70, 71].

Neural networks and fuzzy logic: In recent years, considerable efforts have been dedicated to developing non-model based techniques for structural control applications. Both neural networks and fuzzy logic facilitate model-free algorithms that can handle non-linearity, accommodate a high degree of parallel implementation and tolerate uncertainty in the system [72]. The main advantage of neural network controllers is their ability to learn on-line. Although most existing studies in structural control using neural networks require computationally intensive off-line training, this leads to online adaptability which can handle system uncertainties or respond to actuator failures. Fuzzy control theory has the advantage of rather simple computations for the controller that can be easily implemented into a fuzzy chip [6]. The distinguishing feature of fuzzy logic control is the ability to use terms that are easily understood. The review studies by Venanzi [72] and Datta [6] summarize the past and current applications of neural networks and fuzzy logic to structural control problems.

2.3 Control-structure interaction

The use of active devices leads to the potential for undesirable dynamic interaction between the control system and underlying structure, known as control-structure interaction (CSI). If left unaccounted for, this interaction can severely limit the performance and robustness of control systems [73]. This section provides a brief overview of the CSI problem and discusses the various research efforts focused on addressing these effects.

2.3.1 Overview of control-structure interaction

To demonstrate the role of this interaction in control system design, consider the schematic block diagram of a general active control problem in Figure 2.2. When mechanical actuators are used, dynamic coupling exists between the actuator and structure as signified by the dotted line. The presence of this coupling indicates that is it not possible to separate the dynamics of the actuator and structure and model them as two independent systems connected in series [73]. The simple case of a linear system controlled by a single actuator with command input u and output force f is shown in Figure 2.3. Following Dyke et al. [73], the dynamic coupling is modelled as feedback from the structure output to actuator input and is assumed to have associated dynamics

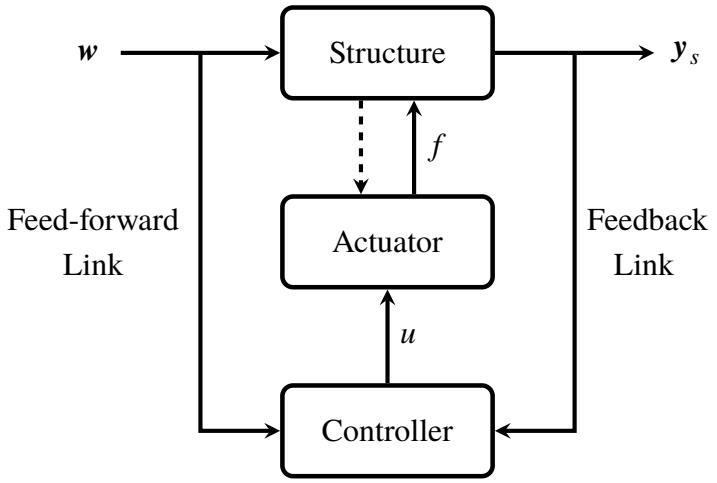

Figure 2.2: Schematic of general active structural control problem with CSI

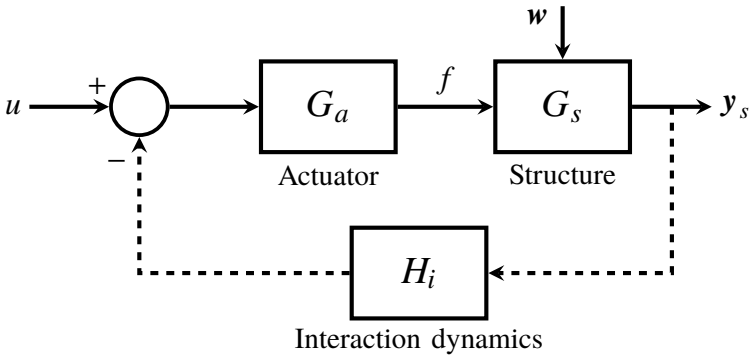

Figure 2.3: Block diagram representation of interaction between actuator and structure

represented by H_i. Given models for the actuator and structure, denoted G_a and G_s respectively, the overall transfer function from the control input u to the system response $\boldsymbol{y}_s$ is given by:

$$G_{yu} = \frac{G_s G_a}{(1 + G_s G_a H_i)} \tag{2.4}$$

Similarly, the transfer function from the control input u to the generated force f is given by:

$$G_{fu} = \frac{G_a}{(1 + G_s G_a H_i)} \tag{2.5}$$

By representing the dynamic systems as polynomial fractions, Equations 2.4 and 2.5 become

$$G_{yu} = \frac{n_s n_a d_i}{(d_s d_a d_i + n_s n_a n_i)} \tag{2.6}$$

$$G_{fu} = \frac{d_s n_a d_i}{(d_s d_a d_i + n_s n_a n_i)} \tag{2.7}$$

where $G_s = \frac{n_s}{d_s}$, $G_a = \frac{n_a}{d_a}$, and $H_i = \frac{n_i}{d_i}$. Unless pole-zero cancellation occurs – which is considered to be unlikely – the transfer functions G_{yu} and G_{fu} have the same poles and the poles of the structure are zeros of the transfer function G_{fu}. As such, the magnitude and phase characteristics of G_{fu} vary depending on the structure thereby coupling the two systems. Moreover, the presence of the structure's poles as zeros in G_{fu} indicate a limited ability to apply forces at the structure's natural frequencies [73]. This ability is greatly limited in lightly damped structures and removed in undamped systems.

2.3.2 Addressing interaction effects

Prior to 1995, the effects of CSI in structural control applications were not well understood and often misrepresented in literature as a time delay associated with the generation of control forces. The effects became clear in the seminal paper by Dyke et al. [73] which presented the general framework for studying CSI and proposed a model, specifically for hydraulic actuators, to account for these effects. Building on this work, Battaini et al. [74] demonstrated the use of bench-scale models to study control implications including control-structure interaction and actuator/sensor dynamics. This allows important aspects of full-scale structural control implementations to be studied using scaled models and aided in the understanding of interaction effects. Much of the

subsequent research efforts have focused on accounting for the interaction effects for various active control devices. For example, the role of CSI was studied for torsional servo motors [75] and experimentally investigated to validate proposed models for an electromagnetic mass damper system [76]. More recently, CSI effects have been considered in practical applications such as implementing active control in large-scale wind turbines [77] and the control of micro-vibrations using a giant magnetostrictive actuator [78].

Inherent to the DACS concept is an aspect of mobility which presents a unique challenge in addressing CSI effects. The typical coupling between the structure and actuator is impacted by additional dynamics that are present in order to facilitate mobility and thus warrants a separate investigation.

2.4 Robotics in civil engineering

Over the past two decades, the use of robotic systems and technologies for civil engineering applications has experienced considerable growth. This progress – motivated by the recent advances and increasing affordability of technological systems – has led to significant advances in construction methods and structural health monitoring techniques. Although the most notable advances have been relatively recent, research efforts on the use of robotics for automation of construction, maintenance, and inspection of civil infrastructure dates back to the early 1980's [79]. For the specific case of mobile robotics applied to civil engineering applications, most of the research is related to automated bridge inspection and health monitoring techniques. For example, a mobile robot equipped with a camera was used to collect high-resolution images of a concrete box-girder structure facilitating a visual assessment of the structure without entering the confined space [80]. A mobile robotic platform was also developed for non-destructive bridge deck inspection and evaluation [81]. In this application, the robotic system was used to transport sensing equipment and featured the ability to autonomously traverse a rectangular bridge area. Recently, a ground vehicle with a variety of sensor modalities was developed for generating high quality 3-dimensional point cloud maps to facilitate automated defect detection [82]. In addition to ground-based vehicles, many researchers have investigated the use of aerial vehicles for image collection to enhance traditional inspection practices [83–85]. Despite these wide-spread efforts, the use of mobile robotic systems has yet to be demonstrated in structural control applications.

2.4.1 Autonomous navigation of unknown structures

Nearly all demonstrated applications of mobile robotics in civil engineering require human intervention to navigate the robot. These applications include the remote control of drones for bridge inspection or steering of ground robots for box girder inspections. While this approach may be deemed suitable for structural inspections, it is not practical for structural control purposes. Eliminating the dependence on human intervention requires implementing autonomous navigation. This requires two of the most central tasks in mobile robotics: localization, the process of estimating the robots position as it navigates through a known environment, and mapping, the process of constructing a map of the environment based on estimated locations of features [86]. When faced with an unknown environment (i.e., the first time deployed on a structure), the two processes must be completed concurrently. That is, the robot must build a map of the environment while using the same map to localize itself [87, 88]. This problem – referred to as simultaneous localization and mapping (SLAM) – has been formulated and solved in many different forms in the literature dating back to the early 1990s [89]. Although considerable advancements have been made in the past decade to improve SLAM solutions, a 2008 survey by Aulinas et al. [90] summarizes the most common approaches that are still used today. Despite drawing considerable attention from a wide range of disciplines, the application of SLAM to map existing structures is still an open problem and is associated with unique challenges not directly addressed by existing implementations. These challenges stem from the sparsity and repeated nature of structural elements coupled with restricted navigation that limits the ability to observe features from different viewpoints.

2.5 Gap areas in current state-of-the-art

Structural vibration control is a well-established field dating back to the early 1970's and as structures evolved considerably over the past four decades, so too have the vibration control devices that support them. The resulting literature is therefore dense with an array of devices and various control methodologies that have been largely effective at serving their intended purpose. Despite these efforts, the current state-of-the-art is lacking a solution for immediate, short-term vibration control applications. Scenarios requiring short-term vibration control, such as structures subjected to predictable peak loading events or temporary structures, are becoming increasingly

common with the growing use of lightweight materials and continual push towards more efficient designs. A summary of the gap areas needing to be addressed and thereby motivating this research follows.

1. **Deployability:** Existing passive, active, and semi-active control devices are designed as permanent components of the structure and rely on a fixed, rigid connection through which forces are transferred. In addition to a lengthy design process - often involving detailed finite-element modelling - existing devices require considerable time and effort for installation. Although some devices are becoming standardized and requiring only slight modifications or tuning for different applications, a system suitable for rapid implementation on a range of structures is not available in the literature.

2. **Mobility:** A key aspect influencing the effectiveness of vibration control devices is their relative position on the structure. Existing devices are fixed in a predetermined location to achieve a specific control objective. In cases where a single device is insufficient to achieve the desired performance, multiple fixed devices are used. For example, the use of multiple TMDs is common in vibration control of bridges. A control device capable of changing position on the structure has yet to be studied. Nevertheless, this aspect is required in order to allow a single device to effectively control different structural properties. This is particularly important in controlling lightweight structures where the dominant mode of vibration can change depending on the applied loading. Furthermore, having a mobile control device adds an additional variable, namely the device location, to the controller formulation which could improve overall performance.

3. **Controller Design:** The literature exhaustively covers a wide range of controller formulations for active and semi-active devices. However, the novel concepts of deployability and mobility presented in this research create new control challenges yet to be addressed in other applications. The central challenges involve additional system dynamics and physical operating constraints inherent to the mobile platform. Although control-structure interaction has been studied in great detail for various active control devices, it has yet to be addressed when an additional layer exists between the actuator and structure. Furthermore, the literature largely focuses on actuator stroke constraints and does not cover other constraints present in deployable systems.

4. **Adaptability:** A considerable amount of research has focused on making control devices adaptable. These efforts were inspired by the desire to improve performance and enhance robustness to changes in the structural properties or expected loading. Nevertheless, the extent of adaptability in existing devices is limited by the fact they are fixed in location and intended to control a particular structure. The degree of adaptability increases considerably with a mobile control device, the extent to which has yet to be uncovered in the literature.

2.6 Specific research objectives

Based on the identified limitations in the state-of-the-art, the specific objectives of this research are as follows:

1. Formally define the notion of DACSs and identify the specific components required to achieve deployability and autonomy in control systems.
2. Develop a prototype DACS suitable for immediate, short-term vibration control of a range of structures.
3. Identify the role of control-structure interaction in DACSs and account for these effects within the control formulation.
4. Implement and evaluate various control formulations using the prototype DACS to address challenges of uncertainty in system modelling and physical operating constraints.
5. Address the challenges associated with mobile vibration control systems and demonstrate autonomous navigation of pedestrian bridges using the prototype DACS.
6. Experimentally demonstrate the feasibility and control performance of the prototype DACS for controlling full-scale structures.

Chapter 3

Deployability and autonomy in vibration control systems

This section formalizes the terms deployability and autonomy in DACSs and motivates the concept through specific applications and implementations. Details pertaining to the development of a prototype DACS are presented along with comprehensive descriptions of the various components.

3.1 Requirements for deployability and autonomy

Deployability means that the control system is capable of being readily implemented on a range of structures with only minor customization to the structure or device. This aspect is needed to circumvent the large amounts of time and effort consumed during the design and installation phases of typical devices that inhibit an immediate vibration control solution. In addition to needing a wide control bandwidth in order to be effective on a range of structures, a deployable system requires a simple, standard method for imparting control forces on the structure. Autonomy refers to the ability of the system to react to changes in the dynamic response and effectively control different structural modes of vibration. These properties are important when the intended use or expected response of the structure changes and the control objective needs to be revised. An autonomous control device must have an element of mobility allowing the location of the control force to change as well as sufficient on-board computational hardware to monitor the structural

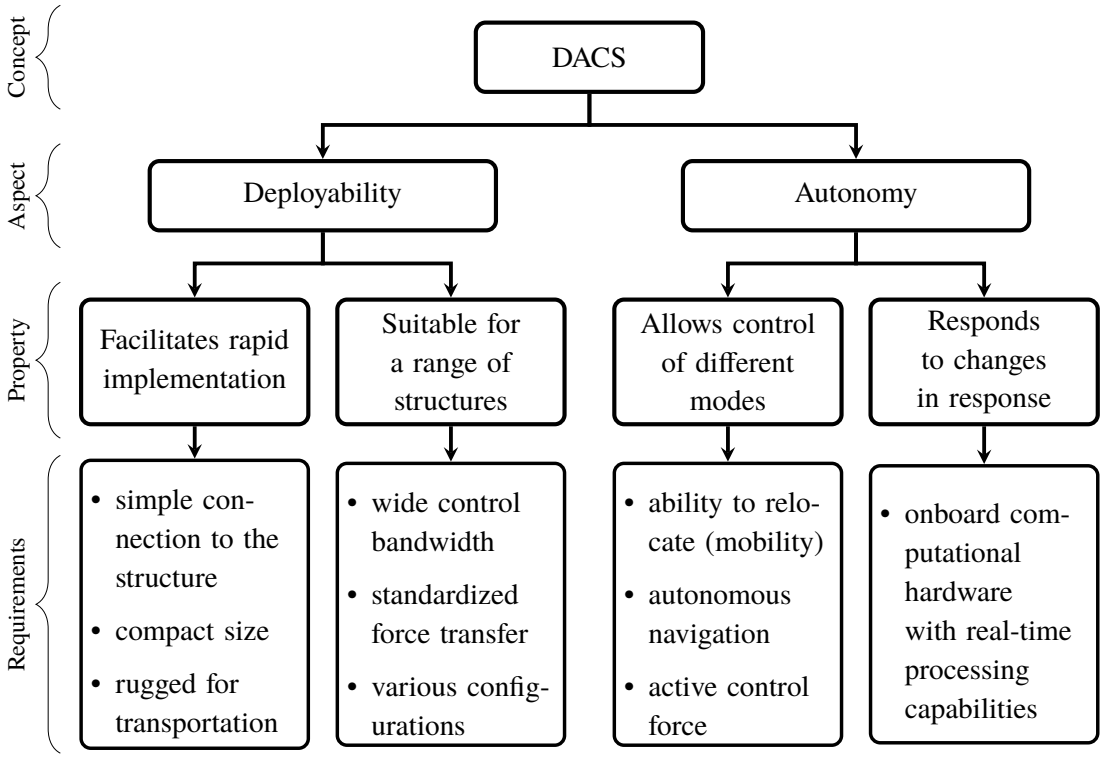

Figure 3.1: Overview of properties and requirements for deployability and autonomy

response, execute control algorithms, and communicate with various hardware components. Given these descriptions, a structured list of the properties and requirements for each aspect of DACSs is presented in Figure 3.1. Based on the requirements in Figure 3.1, the two central challenges associated with developing a DACS are as follows:

1. Designing and implementing a standardized method to impart forces on a generic structure while permitting mobility of the device.

2. Designing and implementing a controller formulation that accounts for additional system dynamics and interaction effects caused by making the system deployable and mobile.

3.2 Potential applications and possible implementations

DACSs embody features that are advantageous in a number of vibration control applications, particularly those where immediate, short-term vibration suppression is needed. For example, the *MakeABridge* system by Maadi Group Inc. [91] is a weld-free pedestrian bridge design that is comprised of aluminum structural elements connected at prefabricated joints. Figures 3.2a and 3.2b show examples of the *MakeABridge* system implemented for military applications and set up for experimental testing at the University of Waterloo respectively. The modular design allows for bridges of various lengths to be built rapidly with minimal design effort and thus yields a cost-effective solution that is suitable for both permanent and temporary applications [91]. Although the use of aluminum provides many benefits in terms of construction and implementation, the associated reduction in self-weight increases the dynamic sensitivity of the bridge structure which in some cases leads to excessive vibrations that exceed specified serviceability limits [92]. The need for auxiliary damping depends primarily on the length of the bridge and applied loading. For example, a bridge installed to provide remote access for one or two pedestrians will experience drastically different pedestrian loads compared to a bridge deployed for a marathon event or military training. A DACS tailored to this class of pedestrian bridges would allow the modular design to remain lightweight, efficient, and be deployed over longer spans by adding the necessary damping on an as-needed or case-by-case basis.

Stadium seating, aluminum bleachers, and concert hall floors are other examples of lightweight or flexible systems that are known to experience issues related to human-induced vibrations [94, 95]. In most cases, the structures only experience excessive vibrations during scheduled events and thus permanent control devices would be under-utilized. Moreover, different events or occupancies may lead to different control requirements that can't be achieved with a permanent device fixed in location. Given the short-term and predictable nature of the vibration control needs, applications such as these would benefit considerably from DACSs. The deployability aspect of a DACS makes it easy to implement the control device during large events and subsequently store it or have it deployed elsewhere while the stadium or concert hall are unoccupied. Furthermore, the concept of DACSs can be leveraged in the design of new structures. In cases where the design is governed by the serviceability criteria, the designer could assume a DACS will be deployed to suppress vibrations under peak loading conditions provided the loading is predictable and well understood. This would relax the design requirements and lead to more efficient designs.

(a) Military application
(Photo Source: Maadi Group Inc. [93])

(b) Experimental testing setup

Figure 3.2: Examples of the *MakeABridge* system

A DACSs can take on many different configurations provided the requirements in Figure 3.1 are achieved. For bridge applications, the system could take the form of a rail-mounted system on the underside of the bridge deck or utilize a mobile platform positioned on a catwalk or sidewalk. Figure 3.3 shows two possible configurations for DACSs on pedestrian bridges. For stadiums or concert hall floor applications, either similar rail mounted systems could be used or a cable-based system could be designed to provide mobility in two directions.

3.3 Development of prototype device

A prototype device is developed to study the feasibility of the DACS concept and demonstrate the advantages of deployability and autonomy in vibration control systems. The prototype system is needed to address a number of practical implementation challenges and experimentally validate controller formulations. Given the requirements for deployability and autonomy, the prototype device consists of three main components: a mobile platform, an actuator, and on-board computation hardware.

(a) Rail-mounted system (b) Mobile platform based system

Figure 3.3: Possible DACS configurations for pedestrian bridges

The need for a wide control bandwidth within a relatively small footprint coupled with the desire to eliminate mechanical moving parts such as gears motivates the use of an electromagnetic mass damper (EMD) as the actuation device. EMDs utilize the driving technology of linear electric motors to transform supplied electric energy into kinetic energy of the moving mass. As such, nearly any linear motor can be adopted for use as an EMD. A customized unmanned ground vehicle (UGV) equipped with vision sensors is used as the mobile platform. UGVs offer the greatest amount of versatility in terms of mobility and provide a large flat surface for mounting the EMD. The use of a UGV also facilitates rapid deployment on a range of structures by transferring inertial control forces through static friction of the pneumatic tires and thus eliminating the need for a rigid connection. Computational hardware is required to complete all monitoring and processing tasks, as well as the execution of control algorithms for the EMD and navigation procedures for the UGV. The prototype DACS employs a National Instruments (NI) compact real-time input-output (cRIO) controller that resides on-board the UGV. The cRIO line of controllers are compact devices with real-time processing capabilities and a field programmable gate array (FPGA) facilitating high-speed, deterministic, and secure data transfer between the sensors and components.

The overall prototype DACS is presented in Figure 3.4. When selecting the various components, special attention is given to the availability of the product and extent of modification needed for integration. This is done to achieve a system that can be easily reproduced and provide an off-the-shelf solution for vibration control. It should be noted the relatively small-scale prototype

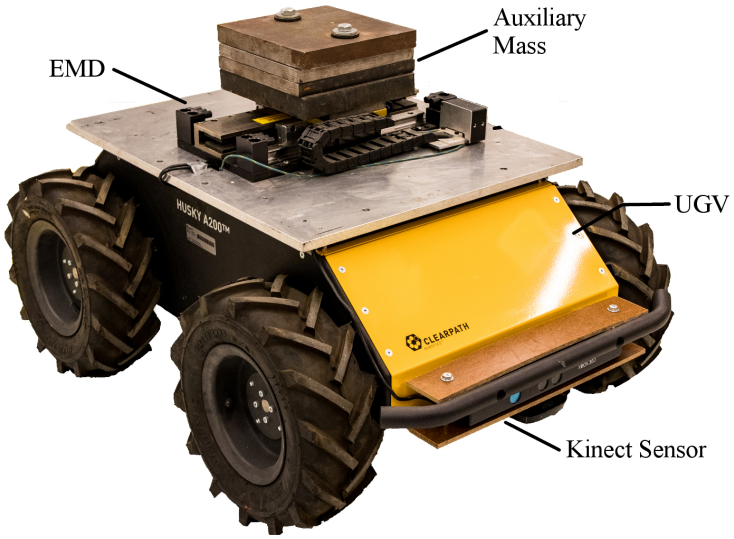

Figure 3.4: Overall DACS prototype for lightweight structures

is designed to target lightweight structures with an approximate mass of 2000 kg and that the prototype is considered to be fully scalable for use with larger structures. Specific properties of the UGV, EMD, and cRIO selected for the prototype DACS are described below.

3.3.1 Mobile platform

A modified Husky A200 UGV built by Clearpath Robotics in Kitchener, Ontario is utilized as the mobile platform [96]. Figure 3.5a shows a 3D rendering of the rugged, yet compact skid-steered vehicle which has a low profile and has been customized to achieve a peak linear velocity of 1.0 m/s. The large 300 mm lug tread tires provide sufficient static friction in the lateral direction to prevent sliding and generate control action. Experimental testing on the UGV reported control forces up to 400 N prior to the onset of tire slippage [97]. As a skid-steered vehicle, there are no axles to connect the left and right wheels. Instead, the front and back wheels on each side are connected and driven independently of the other side. Skid-steered systems are known for providing greater traction and do not require a steering mechanism which is beneficial for transferring control forces. The UGV has a self-weight of 50 kg and features an additional payload capacity of 75 kg which is sufficient for the EMD, sensors, and computational hardware. The

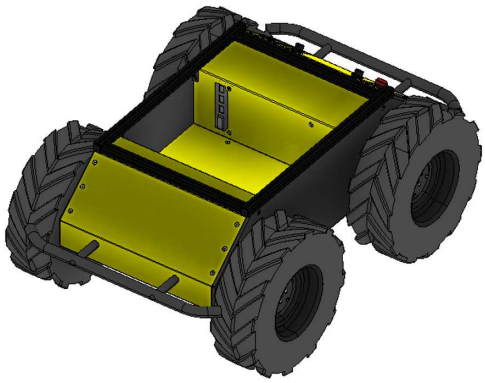

(a) Husky A200 UGV by Clearpath Robotics

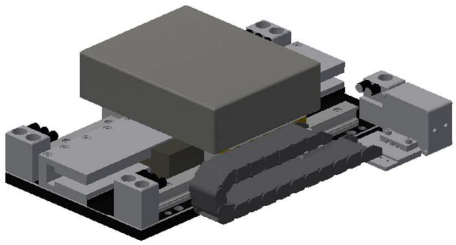

(b) T3D I-force linear motor (EMD)

(c) Microsoft Kinect vision sensor

(d) NI cRIO 9035 controller

Image source: Test Dynamics [98]

Figure 3.5: Main components of the DACS prototype

vehicle design also includes an internal compartment, ideal for housing computational equipment.

Regarding mobility, this UGV is equipped with high-resolution quadrature encoders (200,000 pulse/m) and can be controlled using multiple parameters including direct voltage, wheel speed, or kinematic velocity. The vehicle also provides ready integration with the open-source robot operating system (ROS) which enables the use of several sensor types and position-control algorithms. Autonomous navigation in unknown environments is facilitated by forward and rear-facing Microsoft Kinect sensors mounted on the UGV bumper bars. These sensors, shown in Figure 3.5c, can detect known features on the structure and provide the associated range and bearing measurement information needed for mapping and localization. The Kinect consists of several sensors including a red-green-blue (RGB) sensor to provide colour images of the environment and a 3D depth sensor with infrared transmitter to detect the depths of the corresponding objects in the

RGB image. Since the RGB and depth sensors are not located at the same position, calibration is required to remove distortions and align the images [99]. Open Natural Interaction (OpenNI) – an open-source framework in ROS to interact with digital devices – includes an automated calibration procedure. This method, based on viewing a checker-board pattern in various orientations, is used to calibrate both Kinect sensors. Although Microsoft has not released official hardware specifications for the sensor, the PrimeSense micro-controller used to process the image reports a operating range of 0.8 m – 3.5 m with a field of view of 58° horizontal, 45° vertical, and 70° diagonal. The spatial resolution and depth resolution at a distance of 2 m from the sensor are 3 mm and 10 mm, respectively.

It should be emphasized that a wide range of sensor modalities can be used to facilitate autonomous navigation on unknown structures and the use of Kinect sensors for the prototype system is motivated primarily due to their cost-effectiveness and suitability for indoor use which is where the development and testing takes place. Kinect sensors do not perform well in outdoor lighting conditions and should be replaced with a more suitable vision sensor for practical applications. Moreover, additional sensors such as a global positioning system (GPS), inertial measurement unit (IMU), and/or light detection and ranging (lidar) can also be incorporated to improve autonomous navigation in practical applications.

3.3.2 Actuator

A Parker Automation T3D I-force ironless linear motor positioner powered by a Gemini Gv6K servo drive is utilized as the EMD. The linear motor positioner consists of a carriage attached to a current-carrying coil which moves through a magnetic field created by a series of permanent magnets. The carriage is fitted with a mounting plate for adding auxiliary mass up to a maximum payload of 54 kg. Inertial control forces up to 410 N are generated by moving the carriage which can reach speeds up to 7 m/s. The position of the carriage along the 150 mm stroke is measured using a linear magnetic encoder with 0.005 mm resolution. For use with the prototype DACS, a series of steel plates, totaling 33.6 kg, are mounted on the carriage as auxiliary mass and the effective stroke length is defined as ±65 mm for increased safety. Saturation blocks are designed for the position commands in order to ensure the device operates within the physical limitations. Figure 3.5b shows a rendering of the linear motor with auxiliary mass.

Existing control applications utilizing EMDs rely on electro-mechanical models to predict

the force-voltage relationship [100, 101]. In this way, the desired force command signal is converted directly to a voltage signal which is applied to the motor. However, the T3D linear motor positioner and servo drive are configured to operate under position-feedback. As such, a digital quadrature encoder signal is issued to the servo drive and the computed error between the commanded and measured position is used within a feedback loop to determine the voltage signal. This feedback configuration offers improved motion profile tracking and direct control over end-of-stroke limits as well as higher noise robustness with the use of digital command signals. However, the challenge associated with position feedback for this application is developing the necessary relationship between the desired force and controller input. Details pertaining to the identification of such models are presented in the next chapter.

3.3.3 Computational hardware

The prototype DACS employs a NI cRIO controller (model 9035) that resides on-board the UGV. The cRIO, shown in Figure 3.5d has a 1.33 GHz dual-core processor and FPGA for high-speed, deterministic, and secure data transfer. Programming for the device is achieved using NI Laboratory Virtual Instrument Engineering Workbench (LabVIEW) software, a graphical user interface to configure the FPGA and real-time control loops. Up to eight individual NI modules can be added to the cRIO chassis to facilitate data acquisition and communicate with external hardware. For practical implementations, only two modules are needed to aquire acceleration measurements and communicate with the EMD servo drive; however, for experimental testing and development, additional modules are used to acquire various signals and interface with a dynamic shake table. Table 3.1 provides a complete list of the modules used in this research. In addition to the cRIO, a ROS-enabled laptop is deployed with the system to control the position of the UGV and process Kinect sensor information. A transmission control protocol (TCP) data link is used to establish communication between the cRIO and laptop. This link is responsible for sending and receiving the desired and predicted UGV position and ensuring actuation is not being applied while the UGV is in motion.

Table 3.1: National Instruments C-series modules used with the cRIO 9035

Module	**Function**	**Purpose**
NI 9234	Vibration Input	Acquire acceleration measurements from sensors
NI 9237	Strain/Bridge Input	Acquire control force signal from load cells
NI 9239	Voltage Input	Acquire shake table displacement signal from LVDT
NI 9263	Voltage Output	Send displacement command signal to shake table
NI 9401	Digital I/O	Communicate with the Gv6K servo drive

Chapter 4

System modelling

This chapter presents the general approach to system modelling for the prototype DACS and details the various requirements for two different control system design approaches. The experimental and theoretical studies involved in characterizing the dynamics of the UGV and EMD components are also discussed.

4.1 Overview of the system model

Given the physical components used in the prototype device, various system models can be developed to characterize the system behaviour. Specifically for controller design, the model of interest is one in which the relationship between the EMD position command (i.e., input) and the UGV tire force (i.e., output) is characterized. To simplify system modelling, the UGV and EMD components are treated separately and connected in series. This approach allows for one of the components to be interchanged or modified without having to remodel the entire system. When treated as two separate systems, the EMD inertial force becomes the link between the two components. Figure 4.1 provides a schematic block diagram describing the components included in the prototype system model.

Assuming the UGV dynamics can be captured by an n^{th} order proper transfer function[1]

[1] A transfer function is said to be proper if the order of the numerator is less than or equal to the order of the denominator.

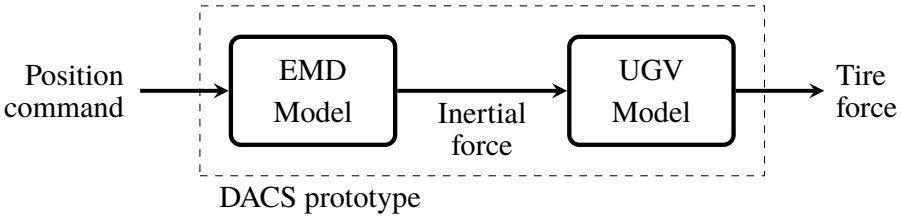

Figure 4.1: Schematic block diagram of prototype system model

denoted $H_{F_tF_e}$, the relationship between the EMD inertial force and UGV tire force can be expressed in the Laplace domain as:

$$F_t(s) = H_{F_tF_e}(s)F_e(s) \tag{4.1}$$

where F_e and F_t denote the EMD inertial force and UGV tire force respectively and the UGV transfer function model with arbitrary coefficients is given by:

$$H_{F_tF_e}(s) = \frac{b_m s^m + \cdots + b_2 s^2 + b_1 s + b_0}{s^n + a_{n-1}s^{n-1} + \cdots + a_2 s^2 + a_1 s + a_0} \tag{4.2}$$

Similarly, assuming the EMD dynamics can be represented by a p^{th} order proper transfer function denoted $H_{F_eP_c}$, the relationship between the EMD command position and EMD inertial force is given by:

$$F_e(s) = H_{F_eP_c}(s)P_c(s) \tag{4.3}$$

where P_c denotes the EMD position command and the EMD transfer function model takes the following form:

$$H_{F_eP_c}(s) = \frac{d_q s^q + \cdots + d_2 s^2 + d_1 s + d_0}{s^p + c_{p-1}s^{p-1} + \cdots + c_2 s^2 + c_1 s + c_0} \tag{4.4}$$

Combining Equations 4.1 and 4.3 is equivalent to connecting the two components in series and thus yields the the overall relationship between the position command and tire force:

$$F_t(s) = H_{F_tF_e}(s)H_{F_eP_c}(s)P_c(s) \tag{4.5}$$

4.2 Control system modelling

Nearly all practical implementations of active structural control are closed-loop systems utilizing force-feedback; however, since the prototype device is both deployable and mobile, establishing a

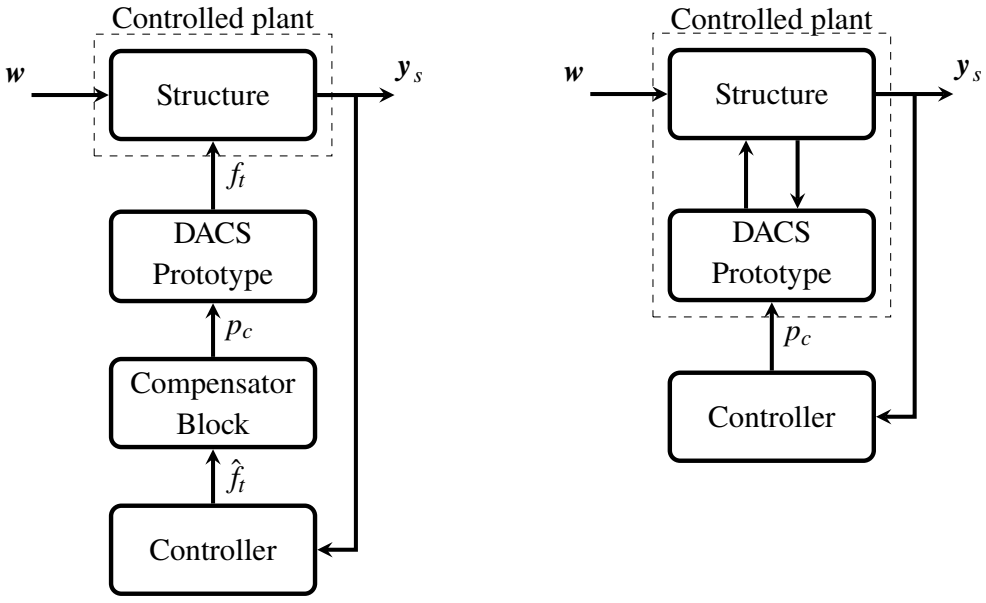

(a) ICM approach

(b) ISM approach

Figure 4.2: Conceptual block diagrams of the ICM and ISM controller modelling approaches

connection that can be used to measure interfacial forces is impractical. Given this constraint, two different control system modelling approaches – referred to as inverse compensation modelling (ICM) and integrated systems modelling (ISM) – are considered in this thesis. Conceptual block diagrams for each approach are provided in Figure 4.2. These approaches are briefly discussed next since the each approach imposes specific constraints and requirements on the EMD and UGV dynamic models.

4.2.1 Inverse compensation modelling

The premise of the ICM approach is to maintain the general controller formulation for active control of structures and compensate for the additional dynamics using an inverse model of the prototype DACS. As shown in Figure 4.2a, the controller design is based solely on the structure model without consideration for the dynamics associated with the prototype device. As such, the use of a DACS will not impose any restrictions on the selection of control algorithms nor increase the complexity. Given the controlled plant contains only the structure model, the

resulting controller output is the desired control force. To achieve this force in the UGV tires, the appropriate input to the control device (i.e., EMD position command) must be determined. As shown in Figure 4.2a, the control input can be computed using a compensation block that contains the inverse DACS model to account for the addition system dynamics. Mathematically, the compensation block is represented by:

$$P_c(s) = \left\{ \left\{ H_{F_t F_e}(s) \right\}^{-1} \left\{ H_{F_e P_c}(s) \right\}^{-1} \right\} F_t(s) \tag{4.6}$$

By relying on the inverse of the prototype model to account for the additional dynamics, the ICM approach minimizes the controller model order and does not impact the level of complexity (i.e., model order and complexity depend solely on the structure model). Nevertheless, the immediate consequence of this approach is the added requirement that both the UGV and the EMD models are invertible. Furthermore, since the prototype model is isolated from the structure model, additional modelling will be required to account for the interaction effects between the DACS and structure.

4.2.2 Integrated systems modelling

The ISM approach accounts for the additional DACS dynamics by integrating the prototype model and structure model into a single plant. Figure 4.2b shows the general concept of the ISM approach. By combining both systems into a single plant, a controller formulation can be developed to directly compute the EMD position command. This eliminates the need for a separate compensation block and provides a framework for addressing interaction effects internally. However, the trade-off in this approach is the increase in controller model order due to additional states from the control device. This may complicate or limit the use of particular control algorithms and thus preference should be given for DACS models of lower orders. Nevertheless, by augmenting the system with the UGV and EMD model, there is no longer a need to compute the corresponding inverse models. As a result, strictly proper transfer functions[2] are valid for this approach.

[2]A transfer function is said to be strictly proper when the order of the numerator is less than the order of the denominator.

4.3 Characterization of UGV dynamics

Accurate characterization of the UGV dynamics is critical for effective control since all inertial forces generated by the EMD are filtered through the vehicle before being applied to the structure. Furthermore, the UGV dynamics will also be excited by the structural response which directly impacts the effective control force and reinforces the need for a reliable model in order to account for these effects. Modelling the UGV dynamics is achieved using two approaches. The first approach, referred to as parametric modelling, assumes a standard analytical form for the model and subsequently tunes the model by estimating the corresponding parameters. The second approach involves fitting a polynomial transfer function model to experimental input-output data. Experimental curve fitting increases flexibility by removing constraints on the model order and treating each coefficient as an independent variable. Nevertheless, this flexibility may result in transfer function models that are not minimum phase[3] which may lead to challenges with model inversion for the ICM approach. In the context of transferring forces, the UGV is an inherently non-linear system due to the presence of pneumatic tires. However, as will be later verified experimentally, linear models are adequate to approximate the dynamics over the frequency range of interest (i.e., 0 – 5 Hz). Furthermore, the implications of using a linear system to approximate the inherently non-linear dynamics are studied through robust controller formulations where approximation errors are treated as model uncertainty.

4.3.1 Parametric modelling

In parametric modelling, the form of the model is predetermined based on knowledge of the system and the number of parameters that are either known *a priori* or can be estimated to fit the model. The simplest parametric model for the UGV is that of a single degree-of-freedom (SDOF) system. In this case, the entire system is represented by only three parameters, namely mass, damping, and stiffness. The well-known force transmissibility function for a generic SDOF oscillator determines the fraction of applied force that is transferred to the base. In terms of the UGV, this is equivalent to the relationship between the EMD inertial force and UGV tire force.

[3] A system is said to be minimum-phase if the system and its inverse are causal and stable.

Table 4.1: Estimated UGV model parameters for different impulse magnitudes

Impulse Force (N)	Frequency (Hz)	Damping Ratio (%)	Mass (kg)	Damping (Ns/m)	Stiffness (N/m)
100	6.49	6.83	50	278	83,163
200	6.39	8.39	50	337	80,705
300	6.24	9.12	50	357	76,918

Thus, a parametric model for the UGV dynamics, denoted $G_{F_t F_e}$, is given by:

$$G_{F_t F_e}(s) = \frac{c_u s + k_u}{m_u s^2 + c_u s + k_u} \tag{4.7}$$

where m_u, c_u, and k_u represent the mass, damping, and stiffness parameters of the UGV respectively. Although the UGV mass can be reasonably estimated (i.e., 50 kg for the prototype), the stiffness and damping parameters must be identified experimentally. Given the inherent nonlinearity stemming from the pneumatic tires, the resulting stiffness and damping properties are expected to be amplitude dependent. Thus, to estimate these parameters various magnitudes of impulsive forces are applied to the top of the UGV while the resulting tire force is measured in four shear-type load cells. A total of five trials are conducted for each of the impulse magnitudes which are set at 100 N, 200 N, and 300 N. Natural frequencies and damping ratios are estimated from each measured free vibration response and averaged across the given impulse magnitude. The averaged frequencies and damping ratios are subsequently used to compute the corresponding stiffness and damping parameters. Table 4.1 summarizes the parameter estimation results for each of the impulse force magnitudes.

Figure 4.3 compares the transfer function models for each case. Although the models vary significantly as they approach the natural frequency, they all lie within ± 5 % of one another over the frequency bandwidth of interest (i.e., 0 to 5 Hz). Opting to use the parameters from the 200 N force trial, the parametric UGV model, is given by:

$$G_{F_t F_e} = \frac{337s + 80,705}{50s^2 + 337s + 80,705} \tag{4.8}$$

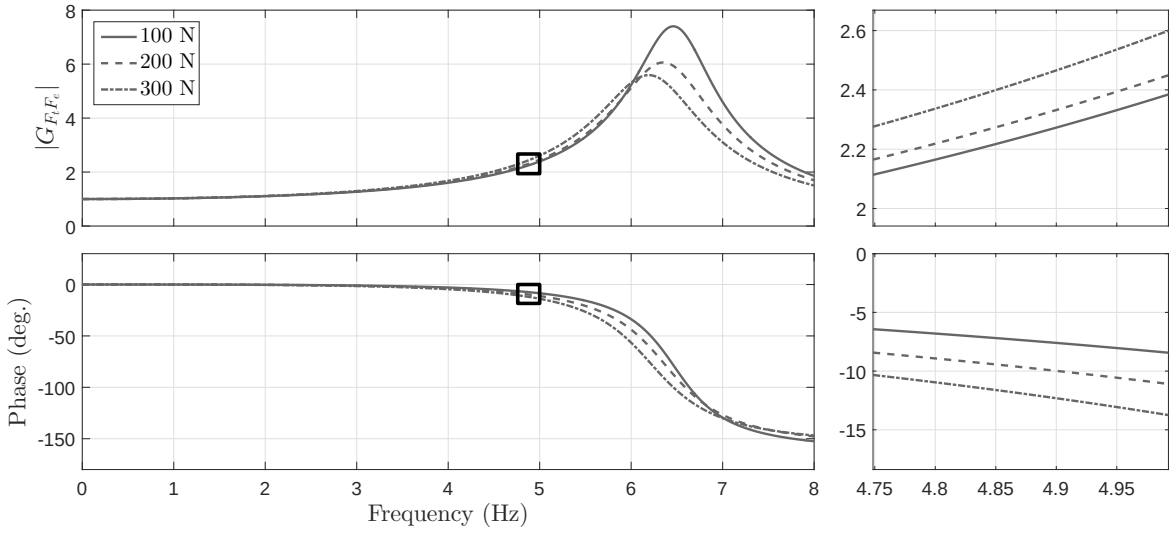

Figure 4.3: Comparison of parametric UGV models

4.3.2 Experimental identification

The main advantage of experimental modelling is the flexibility in model form that allows irregularities such as stiffness eccentricities or complex damping to be intrinsically accounted for. The experimental test setup consists of positioning the UGV atop four shear-type load cells and applying a constant amplitude sine-sweep of inertial forces encompassing the anticipated spectral control bandwidth of 0 to 5 Hz. The input-output data used for estimation are the applied force at the top of the UGV and measured tire force respectively, which is consistent with the parametric model. To investigate the amplitude dependence, a total of six trials are conducted with increasing inertial force amplitudes up to 150 N. Cyclical inertial forces greater than 150 N are amplified to tire forces greater than 400 N which cause the UGV to slip. Frequency response functions (FRFs) are computed for each trial and presented in Figure 4.4. The non-linearity is evident in the magnitude plot, particularly at frequencies greater than 3 Hz where there is significant variation in the force amplification factor for different magnitudes of excitation. This result is expected and consistent with the findings from the parametric identification approach.

Second order transfer function models are fit to each experimental FRF through curve fitting. Second order models sufficiently captured the magnitude and phase properties and achieve higher fit percentages compared to first and third order models; however, none of the obtained models

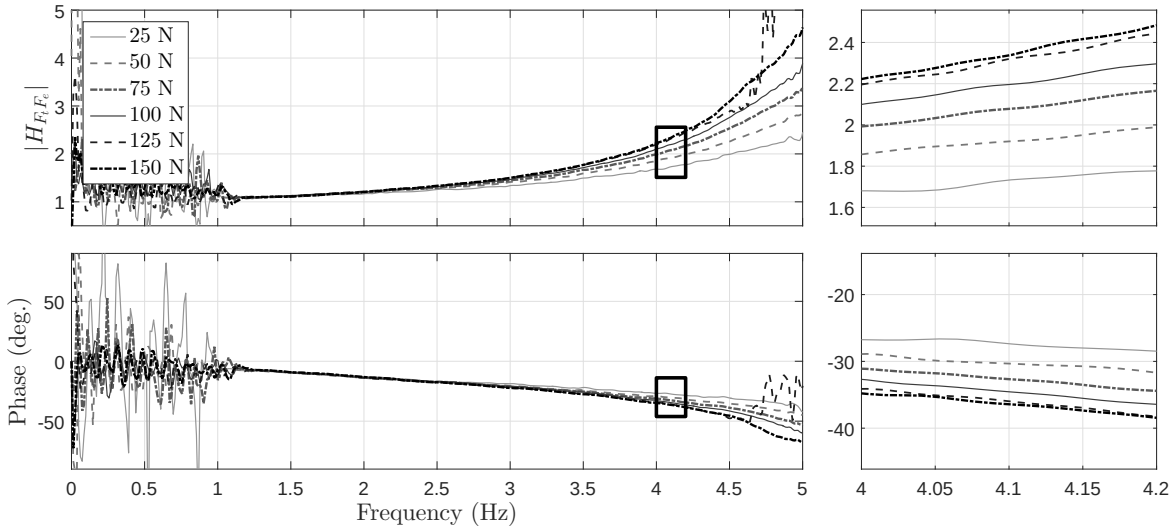

Figure 4.4: Bode plot of experimental FRFs for UGV modelling

are minimum phase and thus the inverse needed for the ICM approach is unstable. To overcome this, each model is decomposed into a minimum-phase portion[4] and an all-pass filter. The inverse model can then be derived through manipulation (i.e., adding appropriate filters to ensure the transfer function is proper) of the minimum-phase portion. Details on this decomposition are provided in Appendix C. The estimated model corresponding to an input amplitude of 75 N is selected as it falls close to the middle of the range and will minimize errors over the full frequency range of operation. The minimum-phase portion of this model is given by:

$$H^{min}_{F_tF_e}(s) = \frac{15.04s + 1428}{s^2 + 6.592s + 1358} \tag{4.9}$$

Important phase information contained in the all-pass filter is lost after separation. However, incorporating a first-order lead-lag compensator, with a cut-off frequency ten times greater than the range of interest (i.e., 50 Hz), can correct the phase errors considerably with negligible impact on the magnitude. The lead-lag compensator, designed based on the phase difference between the estimated model and minimum-phase portion is given by:

$$H_{LL}(s) = \frac{1.04}{0.02s + 1} \tag{4.10}$$

[4]The minimum phase portion is defined as having all poles and zeros contained in the left-half plane but is not necessarily a minimum phase system, as the inverse is not necessarily causal.

Combining the lead-lag compensator with the minimum phase portion yields the experimentally identified model for the UGV dynamics:

$$H_{F_t F_e}(s) = \frac{15.64s + 1485}{0.02s^3 + 1.132s^2 + 33.75s + 1358} \tag{4.11}$$

For consistency, this model will be used for both the ICM and ISM approaches. It should be noted that for the ICM approach, the direct inverse of $H_{F_t F_e}$ results in an improper transfer function[5] In this case, a second order low-pass filter is appended to the inverse model to make it rational. By setting the filter cut off to 50 Hz, there is negligible impact on the magnitude and only a small phase shift over the frequency range of interest. Nevertheless, for the ISM approach no inversion is necessary as the plant model is augmented with the UGV model during controller formulation.

4.3.3 Comparing UGV models

Figure 4.5 compares the identified parametric and experimental UGV models given in Equations 4.8 and 4.11 respectively with the experimental FRFs which are represented by a shaded region encompassing the full range of the models. In terms of magnitude, the models are largely consistent for frequencies up to 2.5 Hz. As the frequencies increase, the parametric model tends towards the lower limit of the experimental range while the experimental model tracks closer to mid-range as designed. Despite both falling within the range of experimental FRFs, the error in magnitude between the two modelling approaches increases from less than 8 % at 3 Hz to nearly 20 % at 5 Hz. By comparing the phase properties, it is clear the parametric model is less accurate in capturing the true damping behaviour compared to the experimental model after adding a lead-lag compensator. Quantitatively, the difference between the two models equates to 14 ms of delay at 3 Hz increasing to 17 ms of delay at 5 Hz. The phase properties of the parametric model could be improved by adjusting the damping parameter; however this will also impact the magnitude. In any case, the implications of fitting linear transfer function models to the non-linear range of FRFs will be studied experimentally. Moreover, the magnitude of variation between the estimated model and range of responses will be modelled as uncertainty in a robust controller formulation.

[5] A transfer function is said to be improper when the order of the numerator is greater than that of the denominator.

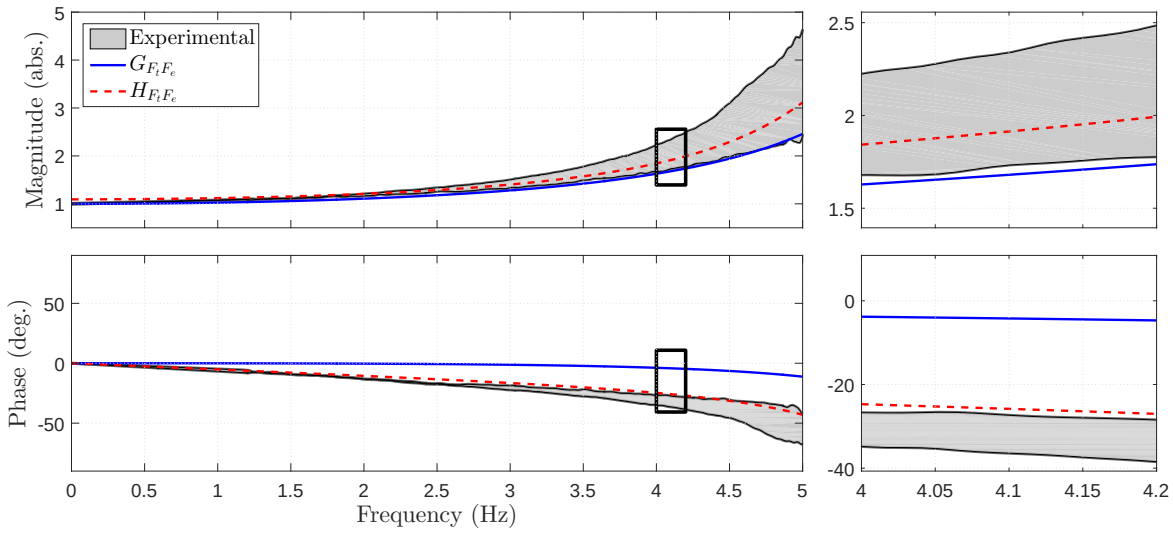

Figure 4.5: Comparison of experimental and parametric UGV transfer function models

4.4 Characterization of EMD dynamics

In general, EMDs can be controlled using force or position feedback. Although it is generally difficult to measure the inertial force directly, relationships based on direct-current (DC) motor principles can be used to relate the motor force to applied voltage. A major drawback with force control of linear motors is the inability to directly account for stroke limitations. Unlike rotary motors, linear motors are vulnerable to interference with end of stroke limits during low frequency or large amplitude motion. Specifically for DACSs, EMDs operating in force control will also suffer from unwanted interaction with the UGV dynamics. Since the generated force is inertial based, that is, relative to an inertial reference frame, any relative motion of the UGV will directly impact the effective force. An alternative to force feedback is position control. Position control addresses the stroke limitations by directly monitoring the position of the carriage and applying saturation when needed. Furthermore, position commands are relative to the base of the EMD meaning the UGV response need not be considered within the EMD control algorithm. It is worth noting however that the response of the UGV acts as a disturbance and may impact the position tracking performance. The drawback of position control is the rather complex relationship between command position and inertial force which is influenced by the closed-loop dynamics of the servo controller including all feedback gains and motor parameters. For the prototype

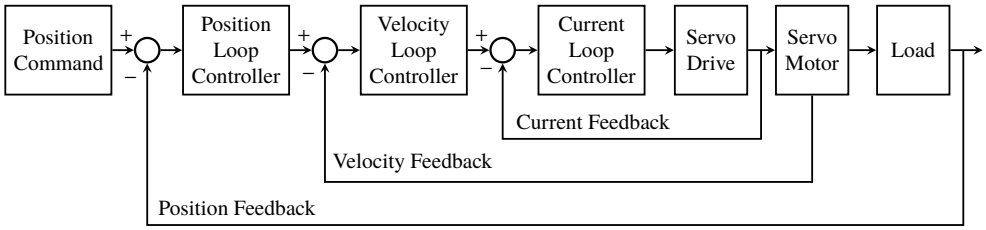

Figure 4.6: Overview of general servo control system

system, position feedback control is implemented for the EMD and as such, a model relating the command position to the inertial force is required. This model can be derived analytically by modelling the closed-loop dynamics or identified experimentally by curve fitting input-output data. Both of these modelling approaches are discussed next.

4.4.1 Closed-loop system modelling

The Gemini GV6K servo controller by Parker Automation uses a combination of three types of control loops, namely position, velocity, and current, to achieve the desired performance. Figure 4.6 shows a schematic of a general servo control system. The inner-most loop is the current control which regulates the power supplied by the drive. In most cases, the current loop is set automatically by the manufacturer to achieve maximum performance. In this case, the bandwidth of the current loop (800 Hz) is much higher than the other control loops and can be approximated as a linear transfer function over the low frequency range of motion. The velocity control loop consists of a proportional-integral (PI) controller that enables the system to respond rapidly to changing commands and resist high-frequency disturbances. However, the velocity loop alone cannot ensure the motor holds position over long periods of time and since position control is desired, the controller is augmented to include a position loop. The position loop includes a proportional controller and is configured in a cascaded structure with the velocity loop, yielding what is commonly known as a proportional-integral-velocity (PIV) controller [102]. The PIV control topology, shown in Figure 4.7, requires only three tuning parameters: proportional and integral gains for the velocity loop denoted K_{PV} and K_{IV} respectively, and a proportional gain for the position loop denoted K_{PP}. Any position error detected in the position loop is scaled by the proportional gain to generate a velocity command. This velocity command is passed into the PI velocity loop along with an estimate of the motor velocity to determine the required force, or

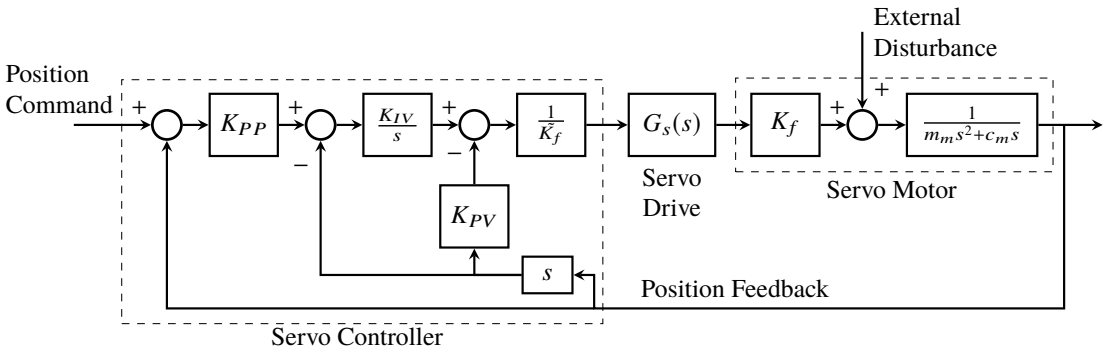

Figure 4.7: Schematic of servo control system for a linear motor

current, to correct the position error.

For modelling purposes, the current loop can represented by a linear transfer function G_s on the servo drive and approximated as unity (i.e., $G_s(s) = 1$). The motor force constant, denoted K_f, represents the force generated per unit of current. Since the force constant depends on the combined motor and load properties and cannot be determined exactly, the term $\tilde{K_f}$ is used to denote an estimate. A distinct advantage of linear motors is the ability to directly connect the load to the motor without the use of mechanical components that may introduce backlash or elasticity. This also facilitates reasonable estimates of the force constant and allows the motor and load to be modelled as a lumped inertial mass m_m with equivalent viscous damping c_m. A schematic of the servo drive, and linear motor model is included in Figure 4.7 Assuming $\tilde{K_f} = K_f$, the closed-loop transfer function between EMD force and command position, denoted $G_{F_e P_c}$ is given by:

$$G_{F_e P_c}(s) = -\frac{(K_{IV} K_{PP} m_m)s^2 + (K_{IV} K_{PP} c_m)s}{m_m s^3 + (K_{PV} + c_m)s^2 + K_{IV} s + K_{IV} K_{PP}} \tag{4.12}$$

Applying the PIV tuning gains and motor parameters summarized in Table 4.2 yields the following analytical EMD model:

$$G_{F_e P_c}(s) = -\frac{9.451 \times 10^5 s^2 + 2.813 \times 10^2 s}{33.6 s^3 + 3.230 \times 10^3 s^2 + 3.044 \times 10^5 s + 2.813 \times 10^7} \tag{4.13}$$

Table 4.2: Motor parameters and PIV tuning gains for EMD

Property		Value	
Total mass	m_m	33.6	kg
Equivalent damping	c_m	0.01	Ns/m
Proportional position gain	K_{PP}	92.4	1/s
Proportional velocity gain	K_{PV}	3,230	Ns/m
Integral velocity gain	K_{IV}	304,420	N/m

4.4.2 Experimental identification

An experimental model of the EMD can be identified through polynomial curve fitting to input-output data where the input and output are the command position and measured force respectively. Experimental identification is more direct than system modelling and accounts for closed-loop dynamics; however, is sensitive to any re-tuning or changes in the EMD auxiliary mass. The test setup involves mounting the EMD directly on a shear-type load cell and exciting the system using six sine-sweep position time-histories encompassing frequencies from 0.5 Hz to 5.0 Hz. The amplitude of each position time-history is scaled to achieve constant accelerations (ranging from 1.5 m/s^2 to 9.0 m/s^2) across the span of frequencies. FRFs between the command position and inertial force are computed for each trial and plotted in Figure 4.8. The relatively tight banding of experimental FRFs indicates consistent and approximately linear performance over the range of desired accelerations. Although analytical modelling suggests a third-order relationship, second-order models achieve higher fit percentages to the experimental data. Averaging over the six trials yields the following experimental model, denoted $H_{F_eP_c}$, for the EMD dynamics:

$$H_{F_eP_c}(s) = \frac{116.2s^2 - 55.07s + 58.36}{s^2 + 78.15s + 3459} \tag{4.14}$$

Although this best fit model is proper, it is not minimum-phase and thus does not yield a stable inverse model for the ICM approach. For inversion, the estimated transfer function is decomposed into a minimum-phase portion in series with an all-pass filter. This decomposition facilitates stable inversion of the minimum phase portion which can be used as an approximation of the system inverse. The minimum-phase portion of the EMD model is given by:

$$H^{min}_{F_eP_c}(s) = -\frac{116.2s^2 + 55.07s + 58.36}{s^2 + 78.15s + 3459} \tag{4.15}$$

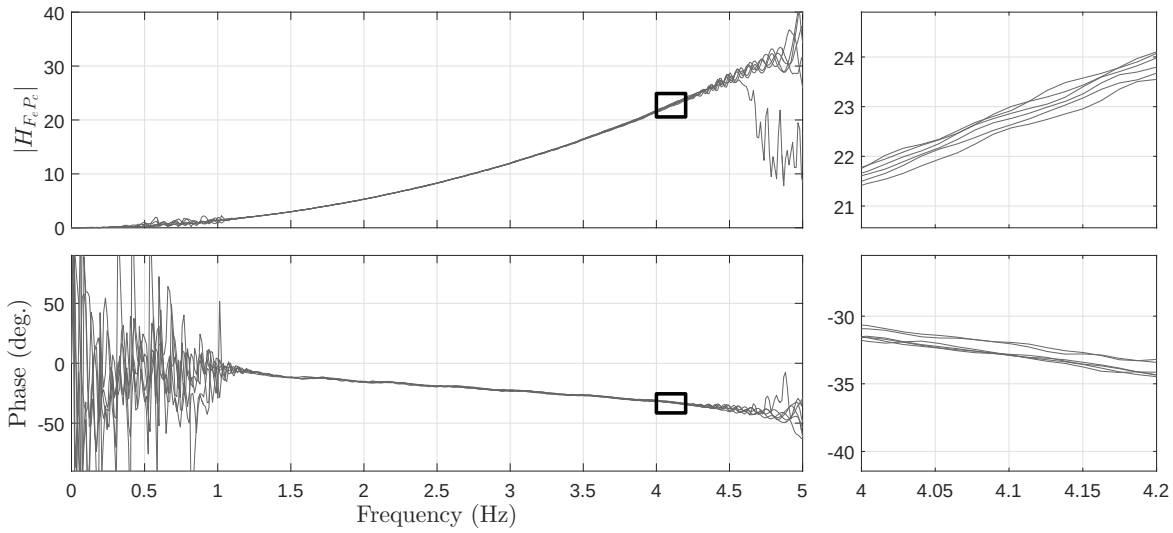

Figure 4.8: Bode plot of experimental FRFs for EMD modelling

Although the magnitude is preserved in the minimum-phase portion, phase information is lost in the all-pass filter. Nevertheless, the phase error decreases rapidly with increasing frequencies from approximately 24 ms at 1 Hz to less than 1 ms at 5 Hz. As a result, the minimum phase portion is an acceptable approximation of the EMD dynamics.

4.4.3 Comparing EMD models

The analytically derived and experimentally identified EMD models are compared with the experimental FRFs in Figure 4.9. The magnitudes of both models are consistent with the tight range of experimental FRFs. The slight difference between the models is attributed to estimation errors in the inertial and motor force constants. The phase properties of the experimental model are more consistent with the experimental FRFs. This small discrepancy of approximately 15 ms at 5 Hz is explained by the unity gain assumption for the servo drive which neglects control delay. Unlike the analytical derivation, any control delay is captured in the input-output data and thus included in the experimental model. As evidenced by the FRFs, the EMD device is capable of providing actuation between 1-5 Hz, which covers many lightweight structural control applications.

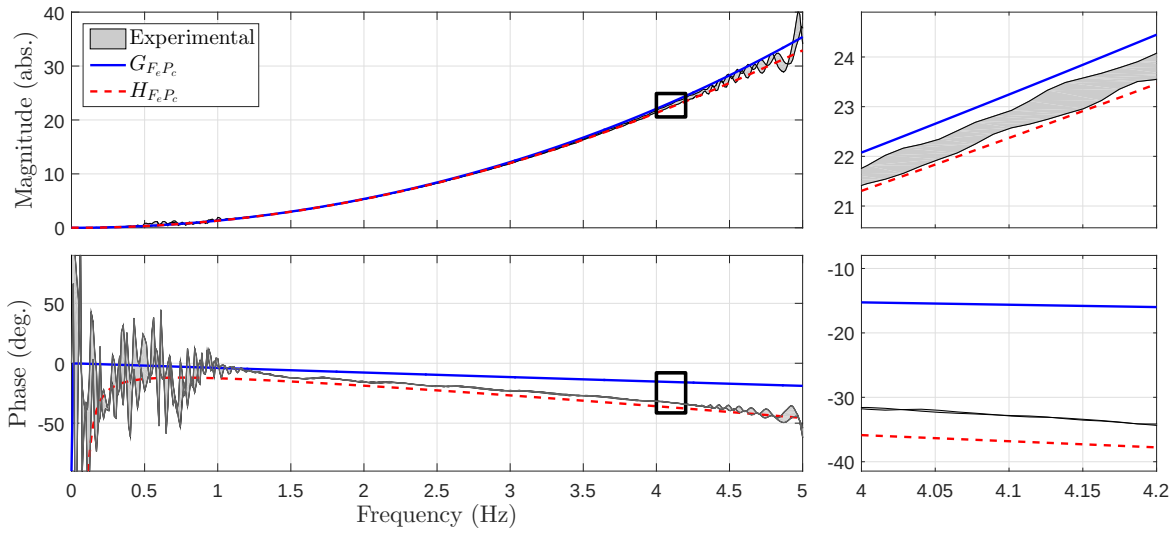

Figure 4.9: Comparison of experimental and analytical EMD transfer function models

4.5 Evaluation of DACS models

Experimental testing is conducted to assess the performance of the identified EMD and UGV models. The purpose of this testing is to identify the extent, in terms of both magnitude and frequency of the control force, for which the identified linear models are a valid representation of the prototype DACS. Table 4.3 describes the composition of the six prototype models considered in this study. The system models are comprised of the analytically derived and experimentally identified EMD models denoted $G_{F_eP_c}$ and $H^{min}_{F_eP_c}$ respectively as well as the parametric, and two experimentally identified UGV models (i.e., the minimum phase portion and the minimum phase portion with a lead-lag filter) denoted $G_{F_tF_e}$, $H^{min}_{F_tF_e}$, and $H_{F_tF_e}$ respectively.

The experimental test setup consists of the prototype DACS positioned atop four shear-type load cells with accelerometers mounted on the UGV body and auxiliary EMD mass to measure the UGV motion and compute inertial forces respectively. Figure 4.10 provides an overview of the experimental setup. Each model listed in Table 4.3 is inverted and discretized before being implemented on the cRIO. The inverse models are used to determine the EMD position command corresponding to a desired UGV tire force. The performance of each model is then assessed by comparing the desired force history with the measured UGV tire forces. To evaluate the models across the intended frequency range of operation, a constant amplitude sine-sweep from 0 Hz to

Table 4.3: Transfer function models for the prototype DACS

Name	Transfer Function Model
DACS-1	$H^{(1)}_{DACS} = H^{min}_{F_eP_c} G_{F_tF_e}$
DACS-2	$H^{(2)}_{DACS} = H^{min}_{F_eP_c} H^{min}_{F_tF_e}$
DACS-3	$H^{(3)}_{DACS} = H^{min}_{F_eP_c} H_{F_tF_e}$
DACS-4	$H^{(4)}_{DACS} = G_{F_eP_c} G_{F_tF_e}$
DACS-5	$H^{(5)}_{DACS} = G_{F_eP_c} H^{min}_{F_tF_e}$
DACS-6	$H^{(6)}_{DACS} = G_{F_eP_c} H_{F_tF_e}$

5 Hz is used. The test is repeated at six different force levels, ranging from 50 N to 300 N, to cover the full range of the device.

Phase-amplitude error indices (PAEI) comparing the desired and measured control forces are computed for each trial. PAEI utilize closed-form equations to decouple phase and amplitude errors and were developed specifically to measure error propagation in experimental testing [103]. The root mean square (RMS) values of the error indices are reported for each trial as well as for frequency subsets (i.e., 0 to 3 Hz and 0 to 4 Hz) of each trial to observe the error with respect to frequency range. Figure 4.11 compares the amplitude and phase errors across the six prototype models for each desired force level. Irrespective of the force level, the phase and amplitude error decreases when the frequency bandwidth is reduced. This confirms the expected non-linear amplification caused by the UGV dynamics at higher frequencies. Comparing the results from DACS-1 through DACS-3 with DACS-4 through DACS-6 respectively indicates a slight improvement in performance from the experimental EMD model compared to the analytically derived model. This improvement is attributed to the phase performance of the experimental EMD model as the difference in magnitude performance is considered negligible. Comparing the results from DACS-1 through DACS-3 provides a means to evaluate the performance of the UGV models. Although the parametric UGV model performs exceptionally well at low force levels, the overshoot in the measured force increases exponentially as the force level increases. This result is consistent with the magnitude curve in Figure 4.5 which shows the analytical model coinciding with the lower limit of the band of experimental FRFs. The improved performance after incorporating the lead-lag compensator (i.e., DACS-3) is evident in the phase error. DACS-3 yields consistently better phase results compared to the minimum-phase portion of the experimental model on its own

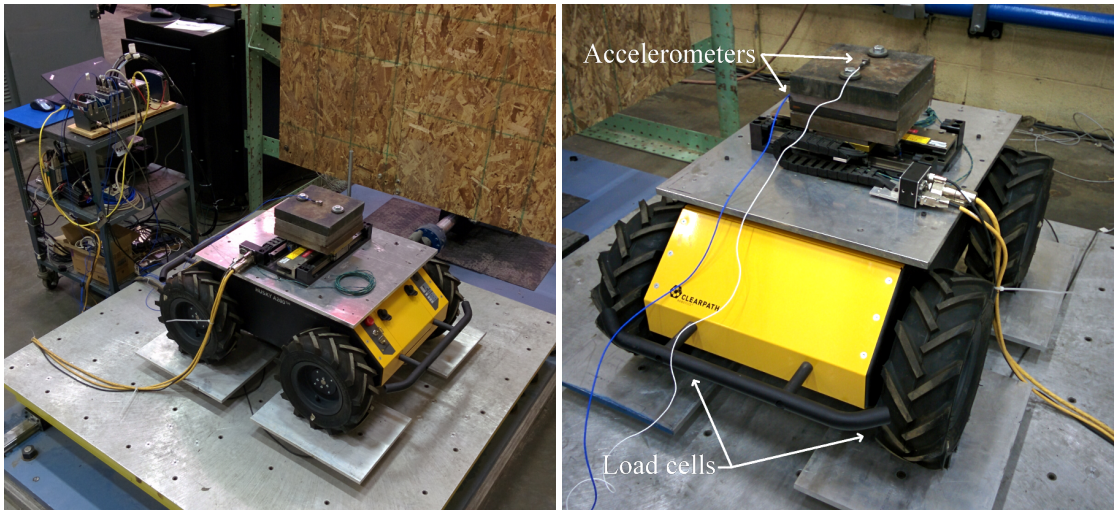

(a) Overall setup (b) Sensor locations

Figure 4.10: Experimental setup for evaluation of DACS models

(i.e., DACS-2). Furthermore, in terms of magnitude, DACS-3 outperforms DACS-2 over the full frequency range up to a force level of 200 N after which DACS-2 yields lower errors. However, the differences between the two models are reduced significantly when considering a narrower frequency bandwidth. Based on the experimental results, DACS-3, the model comprised of the experimental EMD model and experimental UGV model with lead-lag filter yields the highest overall performance. The use of this model suggests errors will be contained to approximately 5 % RMS provided control forces are less than 250 N with frequency content less than 4 Hz.

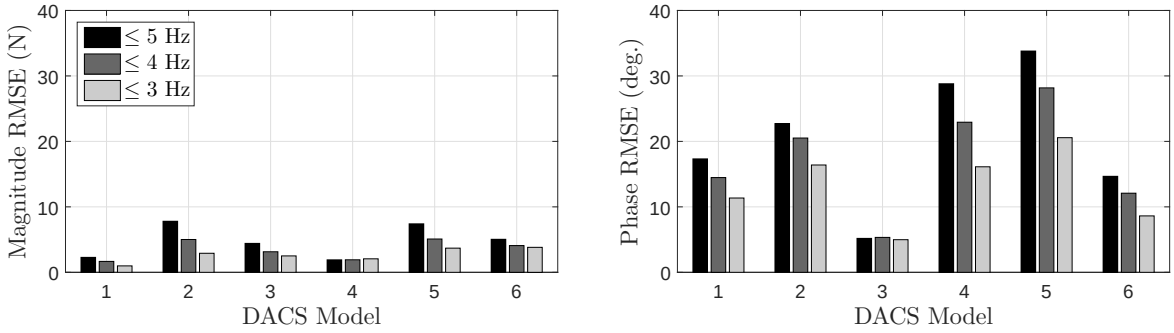

(a) RMSE of amplitude and phase for force level of 50 N

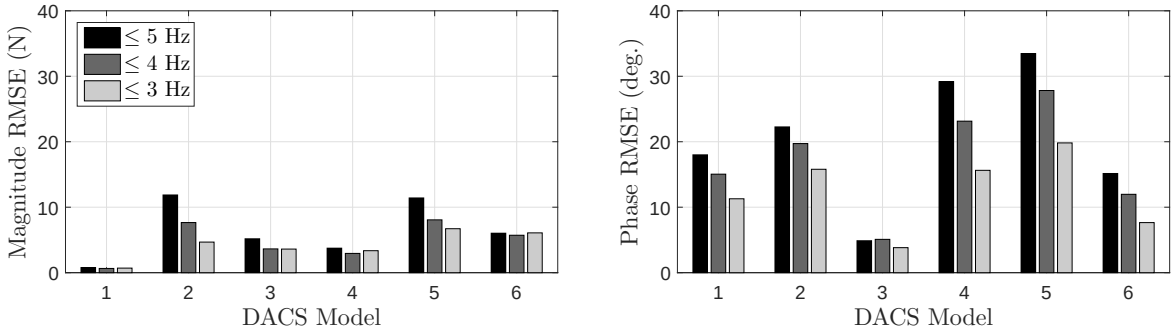

(b) RMSE of amplitude and phase for force level of 100 N

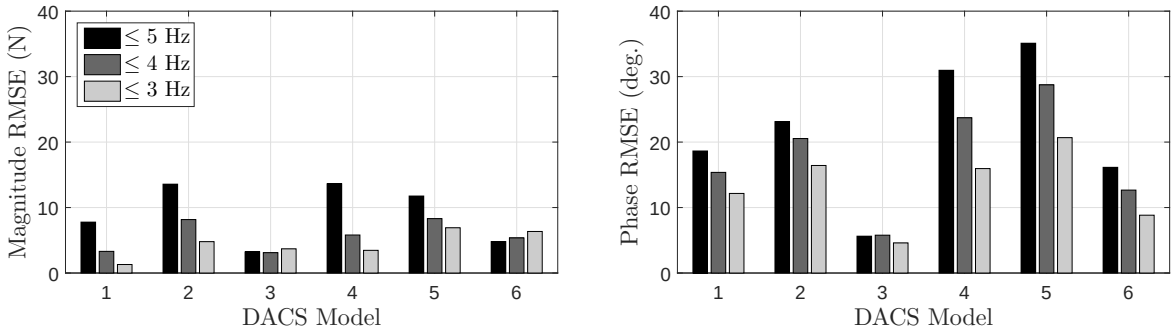

(c) RMSE of amplitude and phase for force level of 150 N

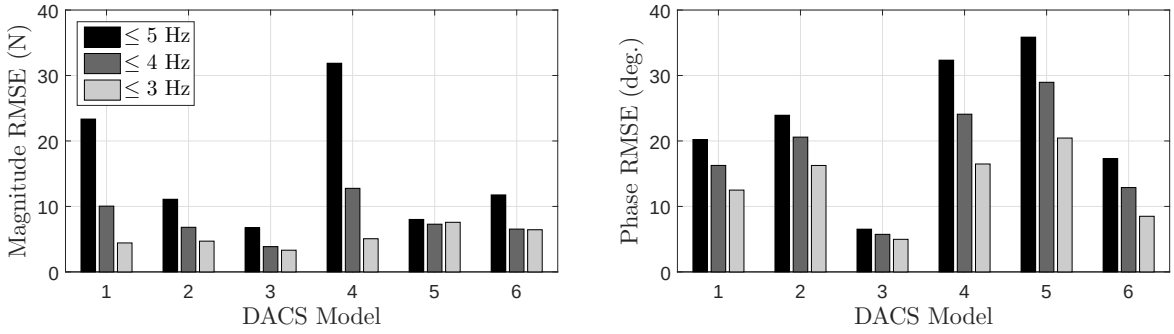

(d) RMSE of amplitude and phase for force level of 200 N

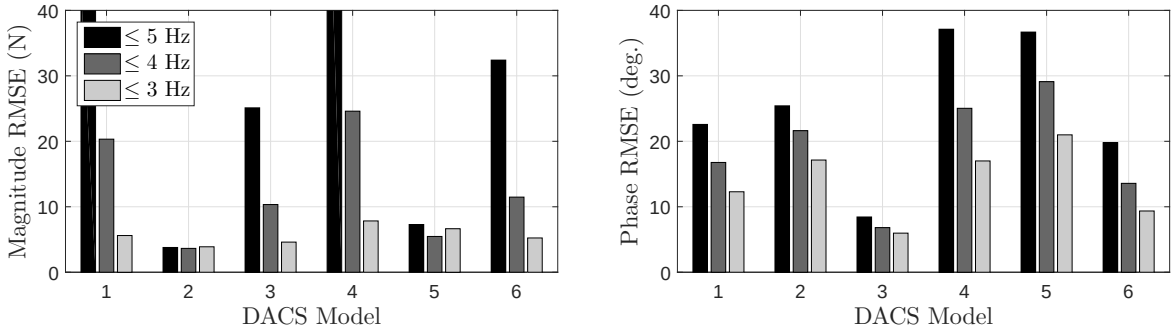

(e) RMSE of amplitude and phase for force level of 250 N

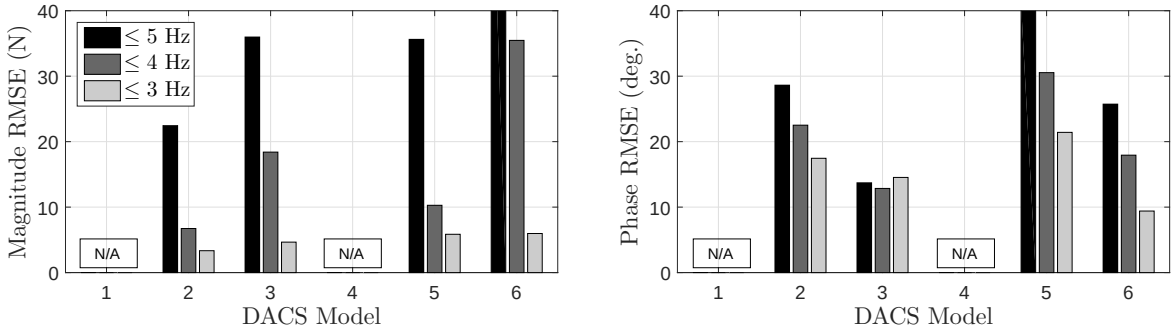

(f) RMSE of amplitude and phase for force level of 300 N

Figure 4.11: Comparison of PAEI for each DACS model at varying force levels

Chapter 5

Controller formulation

Practical applications of active structural control have been largely successful using traditional control algorithms based on optimal control theory (i.e., linear-quadratic or H_2 methods) or robust control techniques (i.e., H_∞ theory) [2, 6, 7]; however, the concept of DACSs introduces a number of unique challenges yet to be addressed by existing implementations. These challenges stem from the presence of additional interaction effects between the structure and control device, the increase in model uncertainty due to complex or non-linear dynamics, and the restrictions due to multiple operating constraints such as EMD stroke limitations and maximum UGV tire forces. The goal of this chapter is to address these challenges through the formulation of various control algorithms for the prototype device. An overview of the general control strategy is presented first, followed by an investigation into the effects of the dynamic interaction between the DACS and underlying structure. Subsequently, three different control algorithms, namely LQG, MPC, and H_∞, are formulated with consideration for the interaction effects, operating constraints, and model uncertainty. Each controller is designed to target a specific challenge of the prototype device, As such, the presented formulations can be adopted for other DACS designs that may only suffer from a subset of the challenges. Designing a single control formulation that addresses all concerns simultaneously is discussed as an item for future work.

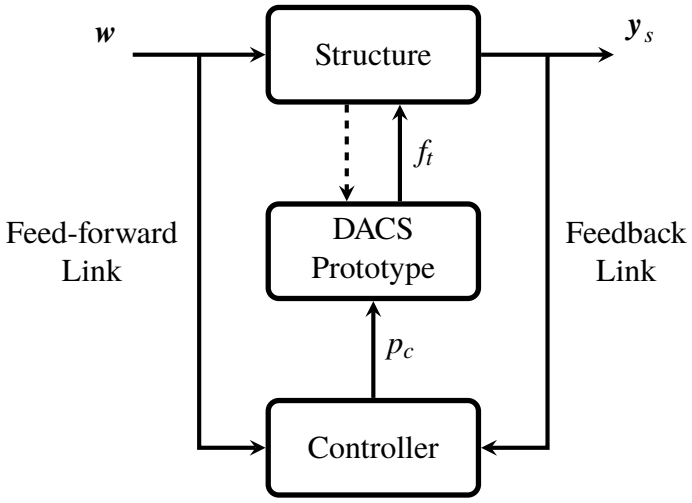

Figure 5.1: General active structural control problem with prototype DACS

5.1 General control strategy

The general active control problem for a structure controlled using the prototype device is described in Figure 5.1. The controller uses measurements of the external excitation $\boldsymbol{w}$ through a feed-forward link and/or measurements of the structural response $\boldsymbol{y}_s$ through a feedback link to compute the control input p_c for the device. With the exception of ground excitation, which could be measured using an accelerometer, structural disturbances such as wind or pedestrian loads are generally difficult to measure. Therefore, the controllers discussed herein will rely solely on the feedback link to compute the control input. For the prototype device, the overall controller determines position commands which are sent to the EMD to generate inertial forces. The inertial forces are then transferred through the UGV and applied to the structure through the tires. The two different approaches for control system modelling – namely ICM and ISM and described in Figure 4.2 – can be used to design the algorithm for the controller block in Figure 5.1. The primary difference between the two approaches is the plant model in which the controller design is based on. In the ICM approach, the plant only contains the structure model. Thus the control algorithm computes the desired control force and an inverse compensation block is needed to determine the EMD position command. Alternatively, following the ISM approach involves integrating the DACS model with the structure model to form the plant. In this case, the control algorithm solves for the optimal EMD position command directly using the augmented plant model. The

dotted line in Figure 5.1 represents the dynamic coupling between the structure and the DACS. The presence of this link, which symbolizes the effect of the structure's motion on the DACS, indicates that it is not possible to treat the DACS and structure as two independent dynamical systems connected in series. Instead, these effects, must be characterized and accounted for in the controller formulation to ensure the desired control force is applied to the structure. Prior to formulating control algorithms for the prototype device, a method to account for the interaction effects is proposed and experimentally validated.

5.2 Control-structure interaction

In typical applications of active structural control, dynamic coupling – widely known as CSI – exists between the actuator and the structure. The role of CSI has been investigated for a range of control devices including hydraulic actuators [73], electric screw drives [75], and force-controlled EMDs [76]. For the prototype DACS, the role of CSI is complicated due to the presence of UGV dynamics and configuration of the EMD to operate in position control. As such, the existing framework which shows the presence of a natural velocity feedback loop for hydraulic actuators and force-controlled EMDs is not directly applicable and a separate investigation is required. To illustrate the dynamic coupling between the prototype device and underlying structure, consider the block diagram description in Figure 5.2 where $G_{\boldsymbol{Y}_s \boldsymbol{F}_a}$ is the transfer function model of the structure describing the relationship between the applied forces $\boldsymbol{F}_a$ and the structural response $\boldsymbol{Y}_s$, $\boldsymbol{W}$ represents the vector of external disturbance, and P_c denotes the EMD position command. It should be noted that both the analytical and experimental models for the UGV and EMD components can be used in the diagram and the analytical models are selected simply for illustration purposes. The dynamic coupling is modelled as feedback from the structure's response to the control input and is assumed to have dynamics modelled by the transfer function H_I. Considering this coupling, the overall transfer function from the EMD command position to the structural response is given by:

$$G_{\boldsymbol{Y}_s P_c} = \frac{G_{\boldsymbol{Y}_s F_t} G_{F_t F_e} G_{F_e P_c}}{1 + G_{\boldsymbol{Y}_s F_t} G_{F_t F_e} G_{F_e P_c} H_I} \tag{5.1}$$

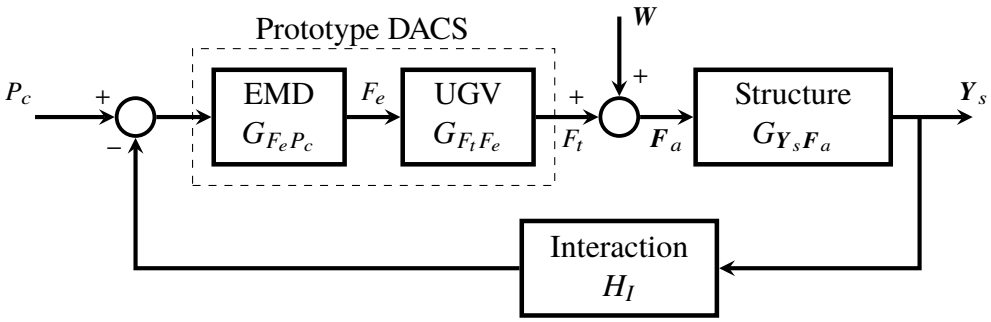

Figure 5.2: General block diagram description of CSI for DACS

Similarly, the transfer function from the EMD command position to the UGV tire force is given by:

$$G_{F_tP_c} = \frac{G_{F_tF_e}G_{F_eP_c}}{1 + G_{Y_sF_t}G_{F_tF_e}G_{F_eP_c}H_I} \tag{5.2}$$

From Equation 5.2 it becomes clear that the relationship between the EMD position command and the UGV tire force is not simply the combination of the EMD and UGV dynamics. Instead, this relationship is influenced by the dynamics of the structure and feedback interaction in addition to the modelled DACS dynamics. As a result, given a desired control force, the required EMD position command cannot be determined via the inverse UGV and EMD models. This also implies that the ICM approach as previously described is not capable of accounting for the interaction effects.

Two key aspects of the prototype device, specifically the ability to model each component individually and the use of position control for the EMD, influence the approach taken to characterize the interaction dynamics. Separating the two components, namely the EMD and UGV, allows the corresponding interaction effects to be studied independently. First consider the interaction dynamics between the structure and the UGV. By itself, the UGV is simply a passive system with an estimated dynamic model and thus the interaction between the UGV and structure can be derived analytically. If the parametric UGV model is used, this derivation is relatively straight-forward as the UGV can be integrated with the structure model analytically by adding an additional degree-of-freedom (DOF) with known mass, stiffness, and damping parameters. Alternatively, if the experimental transfer function is used, the interaction dynamics will require further experimental identification since an analytical expression to integrate the two models is difficult to derive. Next, consider the interaction effects impacting the EMD. In general, motion

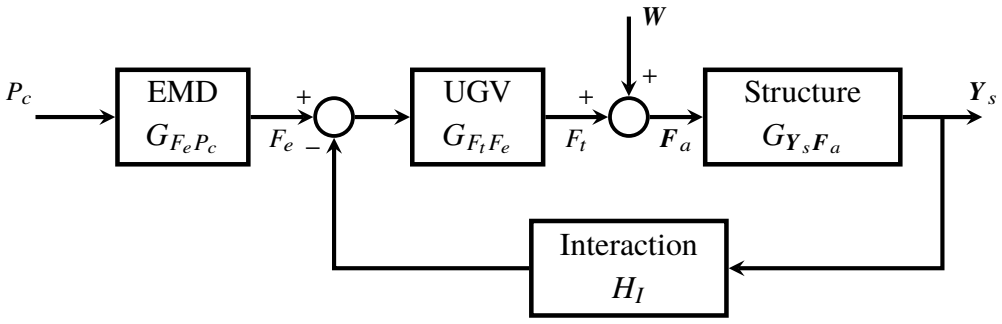

Figure 5.3: Block diagram description of CSI for prototype device

from both the structure and UGV contribute to the overall base motion of the EMD which in-turn impacts the force in the motor. However, given the EMD is configured to operate in position control, the control inputs and resulting inertial forces are measured relative to the base of EMD, not the ground reference frame. As a result, the impact of the dynamic coupling is directly related to the position tracking performance of the EMD when subjected to external disturbances. For example, if a high level of position-tracking is achieved under the expected level of disturbance, the dynamics of the structure and feedback interaction have negligible impact on the EMD model. Assuming the position tracking performance of the EMD is maintained under base excitation, the EMD can be isolated from the feedback interaction. This assumption is reflected in Figure 5.3 which models the feedback interaction between the structure's response and UGV dynamics. Prior to deriving the interaction dynamics between the UGV and underlying structure, this assumption is validated through an experimental study.

5.2.1 Position tracking performance

The ability to neglect the effects of feedback interaction on the EMD relies on the assumption that the disturbance rejection properties of the servo controller are sufficient to achieve a high level of position tracking under base motion. In other words, the servo drive is capable of maintaining the desired position of the mass relative to the EMD base despite external inertial forces generated by the structure's motion and resulting UGV response. The validity of this assumption depends to some extent on the tuning and control authority of the position feedback controller but to a larger extent on the capacity of the linear motor and magnitude of external disturbances. Consider the

extreme cases: slow base excitation (i.e., low frequency, small amplitude) and fast base excitation (i.e., high frequency, large amplitude). Slow base excitation will generate minimal inertial forces on the auxiliary mass and is unlikely to disrupt position tracking. On the other hand, fast base excitation could generate inertial forces too large and/or too rapid for the feedback algorithm to keep up. Thus, the EMD is expected to maintain a high level of position tracking up to a certain level of base excitation after which the tracking deteriorates and the system eventually becomes unstable. The assumption of negligible interaction effects on the EMD implies the position tracking begins to deteriorate under disturbances of greater magnitude and higher frequency than what can be anticipated for prototype system.

To assess the position tracking performance of the EMD under base excitation, the EMD is mounted directly on a shear-type load cell positioned atop a hydraulic shake table. The shake table provides harmonic base excitation across a range of frequencies and amplitudes. A total of 18 trials are conducted with the harmonic base excitation ranging in frequency from 1 to 5 Hz and in amplitude from 2.5 to 25 mm to yield a spectrum of peak base accelerations from 0.2 to 4.9 m/s^2. For each trial, the EMD is programmed to track a 60-second linearly-varying sine-sweep position time-history encompassing frequencies up to 5 Hz. To establish a baseline for comparison, the position tracking performance is first assessed under no base excitation. Figure 5.4a compares the position command against the measured position which is obtained using a built-in linear magnetic encoder. Under no base excitation the servo controller accurately follows the desired position trajectory with a measured control delay of 17 ms. When subjected to base excitation, small disruptions in the position tracking first appear when the peak base acceleration exceeds 1.75 m/s^2; however, these disruptions only occur when the EMD is moving at frequencies beyond 4 Hz. As the peak base acceleration increases beyond 1.75 m/s^2, the tracking continues to gradually deteriorate and become evident at lower EMD frequencies. Figure 5.4b shows the position tracking performance under 3 Hz harmonic base motion with an amplitude of 10 mm yielding a peak acceleration of 3.6 m/s^2. At this level of disturbance the position tracking begins to oscillate as the servo drive struggles to achieve the forces required to track the desired trajectory. The final trial, reaching a peak base acceleration of 4.9 m/s^2, could not be completed due to controller instability. Under this magnitude of disturbance, the EMD controller is unable to follow the position trajectory beyond 2 Hz. The root mean squared error (RMSE) between the commanded and measured positions is computed for each trial. The RMSE is computed after removing the baseline control delay of 17 ms from the measured signals. To illustrate the

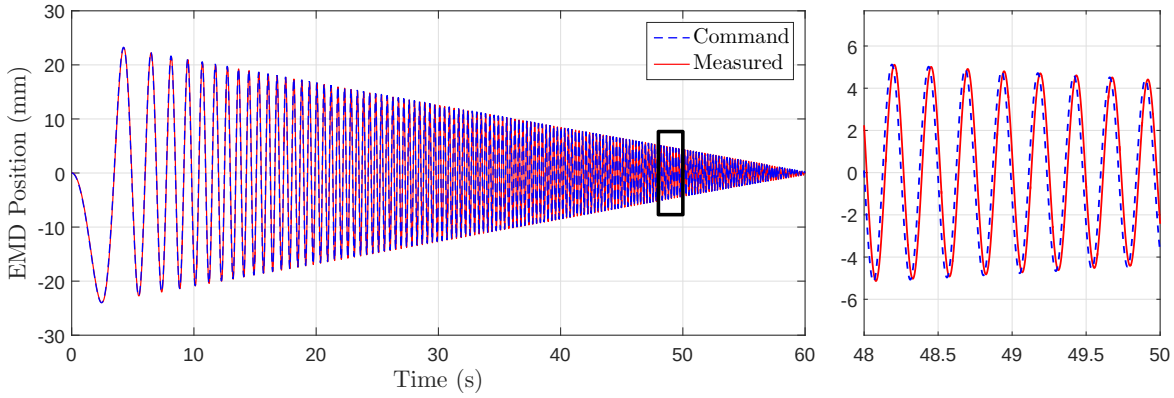

(a) No base-excitation

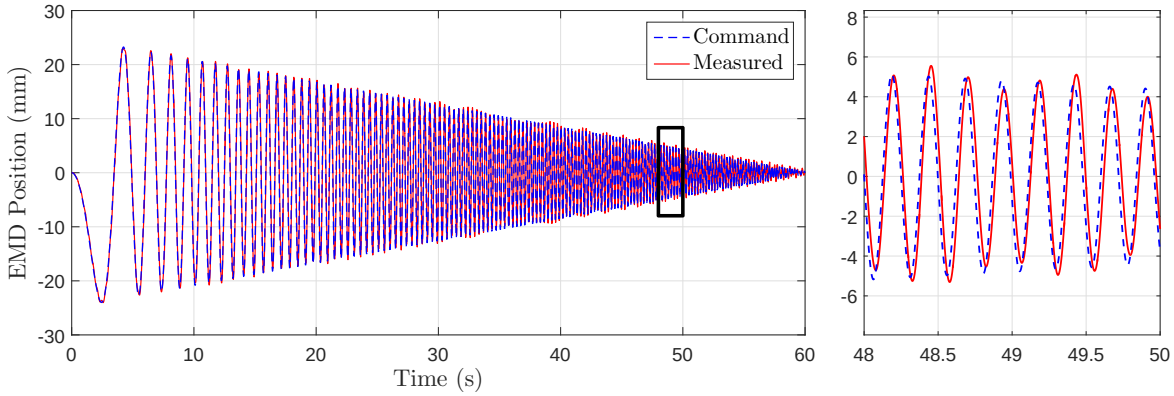

(b) Base excitation with peak acceleration of 3.6 m/s^2

Figure 5.4: Position tracking performance of EMD under varying levels of base excitation

error over different control frequencies, the RMSE is calculated for different windows of the sine-sweep data. Figure 5.5 compares the RMSE at different levels of base excitation for different ranges of EMD frequencies. For all control frequencies, the error increases when subjected to larger base excitation; however, the impact of the disturbance is more prominent at higher control frequencies.

Overall, the position tracking behaviour is consistent with expectations. The EMD accurately tracks positions under base excitation up to approximately 1.75 m/s^2 where performance first shows signs of disruptions at higher EMD frequencies. Performance continues to decrease until eventually becoming unstable. At the onset of the disruptions in position tracking, the EMD is

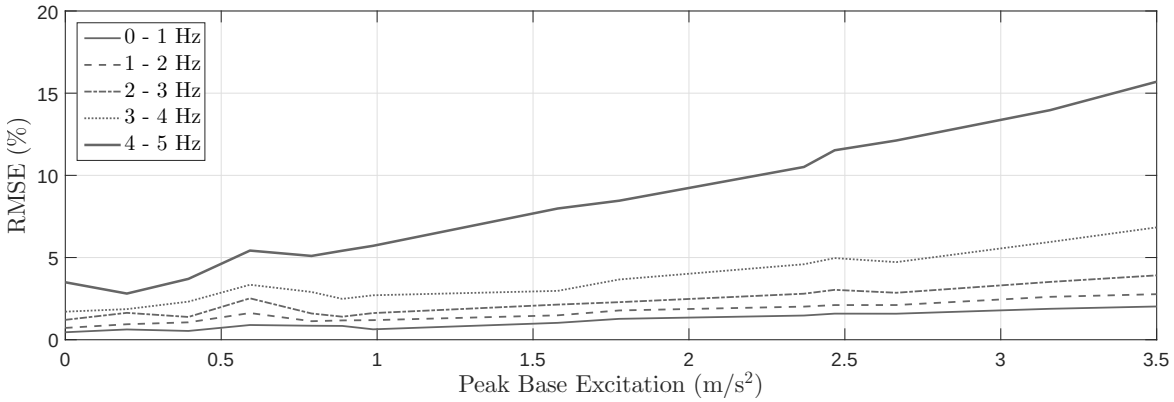

Figure 5.5: RMSE of position tracking for varying control frequencies

generating inertial forces of approximately 225 N at 4 Hz. This magnitude of force falls well outside the control bandwidth of the prototype system, as an EMD force of only 180 N at the same frequency is amplified beyond the peak UGV tire force of 400 N. Given this result, it is reasonable to assume that the servo controller is fast enough to track positions under disturbances from the structure's motion and corresponding UGV response and thus, the interaction effect on the EMD performance is negligible. It is worth emphasizing here that the disturbance rejection property is a key advantage of employing position control for the EMD. Since the position is always tracked relative to the base of the device, the generated inertial force that is applied to the UGV can be uncoupled from the UGV motion. Had the EMD been configured in force control, this separation would not be possible.

5.2.2 Characterizing interaction dynamics

The process for characterizing the feedback interaction dynamics depends on the method used to model the UGV. Given a parametric model of the UGV, the interaction effects can be derived analytically. Conversely, the use of an arbitrary curve-fitted model for the UGV will require further experimental testing and additional curve fitting to estimate the interaction dynamics. First assume the parametric model given in Equation 4.8 is used to represent the UGV dynamics. Given the feedback interaction configuration in Figure 5.3, an expression relating the structural

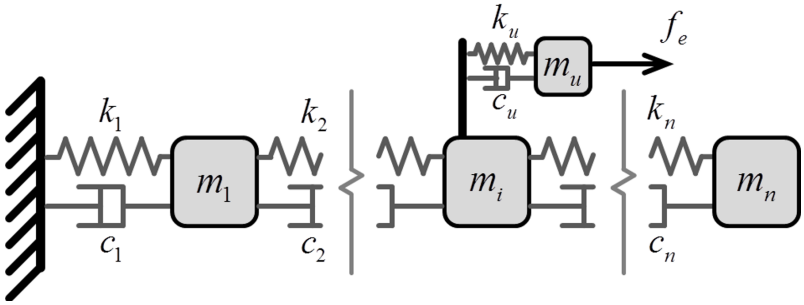

Figure 5.6: General MDOF system with DACS at i^{th} DOF

response $\boldsymbol{Y}_s$ to the EMD inertial force F_e and the external disturbances $\boldsymbol{W}$ can be expressed as:

$$\left(1 + G_{\boldsymbol{Y}_s\boldsymbol{F}_a} G_{F_t F_e} H_I \boldsymbol{E}\boldsymbol{E}^T\right) \boldsymbol{Y}_s(s) = \left(G_{\boldsymbol{Y}_s\boldsymbol{F}_a}\right) \boldsymbol{W}(s) + \left(G_{\boldsymbol{Y}_s\boldsymbol{F}_a} G_{F_t F_e} \boldsymbol{E}\right) F_e(s) \tag{5.3}$$

Assuming the structure model is a multi-degree-of-freedom (MDOF) requires the use of a location vector $\boldsymbol{E}$ to apply the UGV tire force at the appropriate DOF and ensure compatible dimensionality. The location vector indicates the location of the DACS and is expanded to a matrix for the case when multiple DACSs are used. After a series of simplifications, Equation 5.3 can be rewritten as:

$$\left(\frac{1}{G_{\boldsymbol{Y}_s\boldsymbol{F}_a} G_{F_t F_e}} + H_I \boldsymbol{E}\boldsymbol{E}^T\right) \boldsymbol{Y}_s(s) = \left(\frac{1}{G_{F_t F_e}}\right) \boldsymbol{W}(s) + \boldsymbol{E} F_e(s) \tag{5.4}$$

Since the parametric model of the UGV is being utilized, the block diagram in Figure 5.3 is equivalent to a MDOF dynamic system with SDOF systems connected at each location of a DACS. Consider the scenario where a single DACS is deployed on the i^{th} DOF (i.e., $\boldsymbol{E} = [0 \ldots 0\ 1\ 0 \ldots 0]$) as shown in Figure 5.6. External excitation is applied to the structural DOFs while the EMD inertial force is applied to the SDOF system representing the UGV. The dynamics of the combined system are defined by the following equations of motion:

$$\mathbf{M}\ddot{\boldsymbol{x}}_s(t) + \mathbf{C}\dot{\boldsymbol{x}}_s(t) + \mathbf{K}\boldsymbol{x}_s(t) = \boldsymbol{E}\left\{c_u\left(\dot{x}_u(t) - \boldsymbol{E}^T\dot{\boldsymbol{x}}_s(t)\right) + k_u\left(x_u(t) - \boldsymbol{E}^T\boldsymbol{x}_s(t)\right)\right\} + \boldsymbol{w}(t) \tag{5.5a}$$

$$m_u\ddot{x}_u(t) + c_u\left(\dot{x}_u(t) - \boldsymbol{E}^T\dot{\boldsymbol{x}}_s(t)\right) + k_u\left(x_u(t) - \boldsymbol{E}^T\boldsymbol{x}_s(t)\right) = f_e(t) \tag{5.5b}$$

where $\mathbf{M}$, $\mathbf{C}$, and $\mathbf{K}$ denote the structure's mass, damping, and stiffness matrices respectively and $\boldsymbol{x}_s$ represents the vector of structural displacements. The UGV mass, damping, and stiffness parameters are denoted by m_u, c_u, and k_u respectively while x_u represents the UGV displacement.

The location vector $\boldsymbol{E}$ is used here to extract the structural displacement at the i^{th} DOF and apply the UGV control force at the appropriate location. Expressing Equations 5.5a and 5.5b in the Laplace domain yields:

$$\left(\frac{\mathbf{M}s^2 + \mathbf{C}s + \mathbf{K}}{c_u s + k_u} + \boldsymbol{E}\boldsymbol{E}^T\right)\boldsymbol{X}_s(s) = \left(\frac{1}{c_u s + k_u}\right)\boldsymbol{W}(s) + \boldsymbol{E}X_u(s) \tag{5.6a}$$

$$\left(m_u s^2 + c_u s + k_u\right)\boldsymbol{E}X_u(s) - (c_u s + k_u)\,\boldsymbol{E}\boldsymbol{E}^T\boldsymbol{X}_s(s) = \boldsymbol{E}F_e(s) \tag{5.6b}$$

Combining Equations 5.6a and 5.6b with a series of manipulations can eliminate the UGV displacement term and yield the following expression for the the structural displacement response in terms of the external excitation and EMD inertial force:

$$\left\{\left(\mathbf{M}s^2 + \mathbf{C}s + \mathbf{K}\right)\left(\frac{m_u s^2 + c_u s + k_u}{c_u s + k_u}\right) + m_u s^2 \boldsymbol{E}\boldsymbol{E}^T\right\}\boldsymbol{X}_s(s) = \left(\frac{m_u s^2 + c_u s + k_u}{c_u s + k_u}\right)\boldsymbol{W}(s) + \boldsymbol{E}F_e(s) \tag{5.7}$$

Notice this expression has the same form as Equation 5.4 which was derived from the block diagram description with unknown interaction dynamics. Given the following transfer function models for the structure and the UGV:

$$G_{\boldsymbol{X}_s\boldsymbol{F}_a} = \frac{1}{\mathbf{M}s^2 + \mathbf{C}s + \mathbf{K}} \tag{5.8}$$

$$G_{F_t F_e} = \frac{c_u s + k_u}{m_u s^2 + c_u s + k_u} \tag{5.9}$$

the appropriate substitutions can be made in Equation 5.7 to yield:

$$\left(\frac{1}{G_{\boldsymbol{X}_s\boldsymbol{F}_a} G_{F_t F_e}} + m_u s^2 \boldsymbol{E}\boldsymbol{E}^T\right)\boldsymbol{X}_s(s) = \left(\frac{1}{G_{F_t F_e}}\right)\boldsymbol{W}(s) + \boldsymbol{E}F_e(s) \tag{5.10}$$

Finally, equating Equation 5.10 with Equation 5.4 gives:

$$\left(m_u s^2 \boldsymbol{E}\boldsymbol{E}^T\right)\boldsymbol{X}_s(s) = \left(H_I \boldsymbol{E}\boldsymbol{E}^T\right)\boldsymbol{Y}_s(s) \tag{5.11}$$

Therefore, given the structure's displacement response (i.e., $\boldsymbol{Y}_s = \boldsymbol{X}_s$) the interaction dynamics are defined by:

$$H_I = m_u s^2 \tag{5.12}$$

Furthermore, given the structure's acceleration response, the second derivative term is removed and the feedback interaction dynamics are simply modelled using the UGV mass. Notice the

presence of the location vector applied to the structural response which indicates that only the response at the location of the DACS is needed for feedback.

The elegance of this solution is achieved based on the assumption that the UGV behaves as a SDOF system and thus can be integrated analytically with the structure model. Alternatively, if the arbitrary curve-fit UGV model is used, such analytical expressions are not as straight-forward to derive. In this case, full-scale experimental testing is required to fit a transfer function model to the overall block diagram (i.e., between the EMD inertial force and the structural response). The overall transfer function, denoted $H_{\boldsymbol{Y}_s F_e}$, can then be used to solve for the interaction dynamics given the structure model and UGV model. More specifically, if the curve-fit UGV model given in Equation 4.11 is utilized, Equation 5.4 can be rearranged to solve for the interaction dynamics as follows:

$$\boldsymbol{E}\boldsymbol{E}^T H_I = \frac{\boldsymbol{E}F_e(s)}{\boldsymbol{Y}_s(s)} - \frac{1}{G_{\boldsymbol{Y}_s \boldsymbol{F}_a} H_{F_t F_e}} \tag{5.13}$$

where $\frac{\boldsymbol{E}F_e(s)}{\boldsymbol{Y}_s(s)} = H_{\boldsymbol{X}_s F_e}$ is the experimentally identified transfer function model and the external excitation is neglected (i.e., $\boldsymbol{W} = 0$).

Both approaches for identifying the interaction dynamics require a certain level of approximation. For the case of the parametric UGV model, the approximation is governed by the accuracy of the UGV model itself. As shown in Figure 4.5, the parametric model does not capture the phase performance as well as the experimentally identified model and tracks the lower bound of the magnitude range. By comparison, the use of the experimental or curve-fit UGV model creates the potential for estimation errors through full-scale experimental testing, formulating a transfer function model for the structure, and curve-fitting the overall transfer function. These errors are added to the uncertainty present in the experimental UGV model itself. The simplicity and conciseness of the parametric modelling solution has a number of advantages over an arbitrary transfer function model. For example, the simple UGV mass feedback dynamics can be directly incorporated in the controller model without increasing the model-order however a curve-fit transfer function will require appending additional states to the system model and increase the overall complexity. Furthermore, it should be noted that the use of the parametric UGV model to analytically derive the feedback dynamics does not preclude the use of the curve-fit model in controller design. As such, the analytical estimation of the interaction dynamics is used for controller design.

The idea behind the ICM approach to controller modelling is to utilize inverse EMD and

UGV models to compensate for the dynamics of the DACS. However, as shown, the dynamic coupling between the structure and the UGV prevent the separation of the structure and UGV as independent systems connected in series. Therefore, the ICM approach is modified to incorporate the parametric UGV model with the structure model in the plant. The resulting control algorithm will compute the desired inertial force applied to the UGV and the inverse EMD model will still be used to determine the required position command. Since the ISM approach to controller modelling already integrates the structure and the DACS models in the plant, no modelling change is required.

5.3 Linear-quadratic optimal control

In civil engineering applications, there exists a trade-off between control performance and robust stability. In general, higher control authority tends to improve control performance, but uncertainties in the system model could severely degrade performance and even cause instabilities if the control authority is too high [104]. Linear quadratic controllers utilize quadratic cost functions to balance control performance with control effort and provide an effective solution for addressing this trade-off [105]. The LQR design method yields optimal linear state feedback gains to control systems under perfect information (i.e., full state information is known). To address the case with partial state information, which is commonly the case in structural control, the separation principle (i.e., the principle of separation of estimation and control) is applied to first estimate the states using an optimal estimator and subsequently treat the estimates as true states in a controller that is optimal for the system under perfect information. The separation principle significantly simplifies the controller design by guaranteeing that the two systems, namely the optimal estimator and optimal controller, can be designed independently and combined. The combination of a Kalman filter and LQR yields the LQG controller which is widely used for control of stochastic linear systems disturbed by additive Gaussian noise with incomplete state information.

5.3.1 LQG formulation

Consider the continuous-time, time-invariant, linear dynamic system

$$\dot{z}(t) = \mathbf{A}z(t) + \mathbf{B}\boldsymbol{u}(t) + \boldsymbol{\omega}(t) \tag{5.14a}$$

$$\boldsymbol{y}(t) = \mathbf{C}z(t) + \mathbf{D}\boldsymbol{u}(t) + \boldsymbol{\nu}(t) \tag{5.14b}$$

where z represents the vector of state variables, $\boldsymbol{u}$ is the vector of control inputs, and $\boldsymbol{y}$ is the vector of measured outputs. Additive white Gaussian process noise and measurement noise are represented by $\boldsymbol{\omega}$ and $\boldsymbol{\nu}$ respectively. Given this system, the objective is to find the control input $\boldsymbol{u}(t)$ as a linear function of past outputs and/or control inputs such that the following quadratic cost function is minimized:

$$J = \int_0^\infty \left(z^T(t)\mathbf{W}_z z(t) + \boldsymbol{u}^T(t)\mathbf{W}_{\boldsymbol{u}}\boldsymbol{u}(t) \right) dt \tag{5.15}$$

where $\mathbf{W}_z \geq 0$ and $\mathbf{W}_{\boldsymbol{u}} > 0$ are weighting matrices penalizing non-zero states and the level of control input respectively. The cost function is minimized by linear state-feedback of the following form:

$$\boldsymbol{u}(t) = \boldsymbol{K}_c z \tag{5.16}$$

where the controller gain matrix $\boldsymbol{K}_c$ is given by:

$$\boldsymbol{K}_c = -\frac{1}{2}\mathbf{W}_{\boldsymbol{u}}{}^{-1}\mathbf{B}^T\mathbf{H}_K \tag{5.17}$$

and $\mathbf{H}_K$ satisfies the following algebraic Riccati equation:

$$\mathbf{A}^T\mathbf{H}_K + \mathbf{H}_K\mathbf{A} - \mathbf{H}_K\mathbf{B}\mathbf{W}_{\boldsymbol{u}}{}^{-1}\mathbf{B}^T\mathbf{H}_K + \mathbf{W}_z = 0 \tag{5.18}$$

In LQG control, the measured outputs $\boldsymbol{y}$ may not provide full state information. In this case, a Kalman filter is used to generate an estimate the state vector, denoted $\hat{z}$, given the measured outputs. Details pertaining to the Kalman filter formulation are omitted here but can be found in Appendix B.

5.3.2 Implementing LQG for DACSs

An LQG controller can be implemented for DACSs under both the ICM and ISM approaches. In the ISM approach, the LQG controller is formulated for an integrated plant model containing both

the structure and the DACS and as such computes the optimal EMD position command directly. Alternatively, the ICM approach formulates a controller based on an combined structure and UGV model while the EMD model is isolated. In this case, the controller computes the optimal EMD inertial force and the inverse EMD model is required to determine the corresponding position command. The general implementation procedure for an LQG controller is unchanged by the control system modelling approaches. The only differences between the two approaches is the order of the plant model and size of the weighting matrices. As such, the different formulations for the plant model are presented individually before proceeding with the LQG algorithm.

Plant model for ICM approach: Consider the equations of motion for a general n-DOF system with UGV dynamics added at the i^{th} DOF as shown in Figure 5.6:

$$\mathbf{M}\ddot{\boldsymbol{x}}_s(t) + \mathbf{C}\dot{\boldsymbol{x}}_s(t) + \mathbf{K}\boldsymbol{x}_s(t) = \boldsymbol{E}\left(c_u\dot{x}_{u_r}(t) + k_u x_{u_r}(t)\right) + \boldsymbol{w}(t) \tag{5.19a}$$

$$m_u\left(\ddot{x}_{u_r}(t) + \boldsymbol{E}^T\ddot{\boldsymbol{x}}_s(t)\right) + c_u\dot{x}_{u_r}(t) + k_u x_{u_r}(t) = f_e(t) \tag{5.19b}$$

The structure mass, damping and stiffness matrices are represented by $\mathbf{M}$, $\mathbf{C}$, and $\mathbf{K}$ respectively, $\boldsymbol{x}_s$ is the vector of structural displacements, $\boldsymbol{E}$ is a location vector indicating the location of the prototype system, and the vector $\boldsymbol{w}$ models external disturbances. The UGV is modelled with mass, damping, and stiffness parameters of m_u, c_u, and k_u respectively while x_{u_r} represents the UGV displacement relative to the i^{th} structural DOF and the inertial force generated by the EMD is denoted f_e. Writing Equations 5.19a and 5.19b in state-space form requires an expanded state vector that includes the UGV relative displacement and velocity in addition to the displacement and velocity of the structure. Thus the state vector is given by:

$$\boldsymbol{z} = \begin{bmatrix}\boldsymbol{x}_s & x_{u_r} & \dot{\boldsymbol{x}}_s & \dot{x}_{u_r}\end{bmatrix}^T \tag{5.20}$$

The resulting state and output equations, assuming acceleration measurements of the structure, are given by:

$$\dot{\boldsymbol{z}}(t) = \mathbf{A}\boldsymbol{z}(t) + \mathbf{B}f_e(t) + \boldsymbol{\omega}(t) \tag{5.21a}$$

$$\boldsymbol{y}_s(t) = \mathbf{C}\boldsymbol{z}(t) + \mathbf{D}f_e(t) + \boldsymbol{\nu}(t) \tag{5.21b}$$

where $\boldsymbol{\omega}$ and $\boldsymbol{\nu}$ represent the process noise including external disturbances and measurement noises respectively, and the corresponding state, input, output, and feed-through matrices are

given by:

$$\mathbf{A} = \begin{bmatrix} \mathbf{0}_{n,n} & \mathbf{0}_{n,1} & \mathbf{I}_{n,n} & \mathbf{0}_{n,1} \\ \mathbf{0}_{1,n} & 0 & \mathbf{0}_{1,n} & 1 \\ -\mathbf{M}^{-1}\mathbf{K} & \mathbf{M}^{-1}\boldsymbol{E}k_u & -\mathbf{M}^{-1}\mathbf{C} & \mathbf{M}^{-1}\boldsymbol{E}c_u \\ \boldsymbol{E}^T\mathbf{M}^{-1}\mathbf{K} & -\left(\frac{k_u}{m_u} + \boldsymbol{E}^T\mathbf{M}^{-1}\boldsymbol{E}k_u\right) & \boldsymbol{E}^T\mathbf{M}^{-1}\mathbf{C} & -\left(\frac{c_u}{m_u} + \boldsymbol{E}^T\mathbf{M}^{-1}\boldsymbol{E}c_u\right) \end{bmatrix}, \quad \mathbf{B} = \begin{bmatrix} \mathbf{0}_{n,1} \\ 0 \\ \mathbf{0}_{n,1} \\ \left(\frac{1}{m_u}\right) \end{bmatrix},$$

$$\mathbf{C} = \begin{bmatrix} -\mathbf{M}^{-1}\mathbf{K} & \mathbf{M}^{-1}\boldsymbol{E}k_u & -\mathbf{M}^{-1}\mathbf{C} & \mathbf{M}^{-1}\boldsymbol{E}c_u \end{bmatrix} \quad , \quad \mathbf{D} = \begin{bmatrix} \mathbf{0}_{n,1} \end{bmatrix}$$

Plant model for ISM approach: By contrast, in the ISM approach the transfer function models for both the UGV and EMD are interconnected with the structure model and feedback interaction dynamics are addressed according to the block diagram in Figure 5.3. The overall transfer function model from the EMD position command to the structural response is given by:

$$G_{\boldsymbol{Y}_s P_c} = \frac{G_{F_t F_e} G_{F_e P_c}}{1 + G_{F_t F_e} G_{\boldsymbol{Y}_s \boldsymbol{F}_a} H_I} \tag{5.22}$$

Expressing this transfer function model in state-space form yields the same state and output equations as the ICM approach (see Equations 5.21a and 5.21b); however the state vector in this case contains structure, UGV, and EMD states and the state, input, output, and feed-through matrices are defined in the transformation from the transfer function model to state-space.

Regardless of the modelling approach, the cost function is written in terms of the state vector and EMD inertial force which serves as the control input to the system:

$$J = \int_0^\infty \left(\boldsymbol{z}^T(t)\mathbf{W}_z \boldsymbol{z}(t) + {f_e}^T(t)\mathbf{W}_{\boldsymbol{u}} f_e(t) \right) dt \tag{5.23}$$

As such, minimizing the cost function yields the optimal EMD inertial force given by:

$$\bar{f}_e(t) = \boldsymbol{K}_c \hat{\boldsymbol{z}} \tag{5.24}$$

where $\boldsymbol{K}_c$ is computed using Equation 5.17 and $\hat{\boldsymbol{z}}$ is the estimated state vector.

Determination of the controller gain $\boldsymbol{K}_c$ depends on prescribed weighting matrices $\mathbf{W}_z$ and $\mathbf{W}_{\boldsymbol{u}}$. These weighting matrices are tuned to achieve the desired trade-off between performance and controller effort. In both modelling approaches, the state vector contains the structural states as well as states for the UGV (and EMD in the ISM approach). Thus, the matrix $\mathbf{W}_z$ is designed as

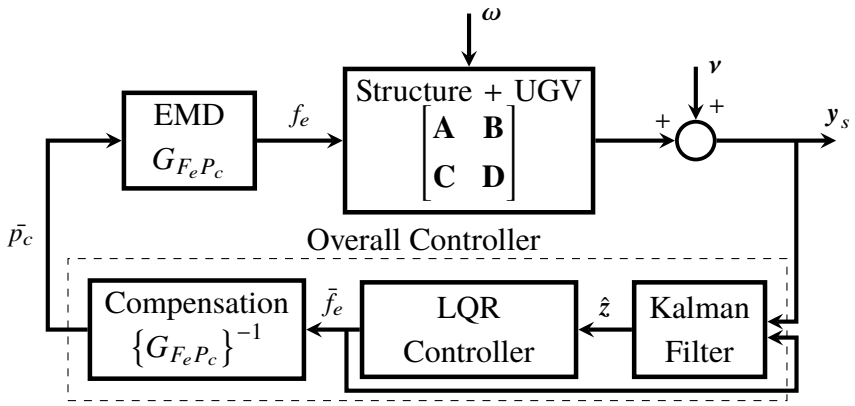

Figure 5.7: LQG controller implementation based on the ICM approach

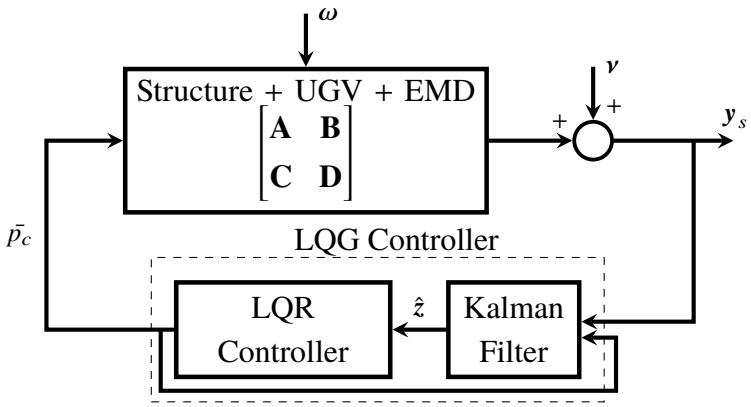

Figure 5.8: LQG controller implementation based on the ISM approach

a diagonal matrix with entries designed to only penalize non-zero structural states. Furthermore, for a single device, the matrix $\mathbf{W}_{\boldsymbol{u}}$ becomes a scalar and is tuned to penalize the level of control. In the ICM approach, after determining the desired inertial force, the inverse EMD model is used to compensate for the EMD dynamics and thereby compute the corresponding position command. By comparison, the ISM approach yields the EMD position commands directly and thus removes the need for a compensation block. Figures 5.7 and 5.8 provides the overall block diagram descriptions of the LQG controller formulated under the ICM and ISM approaches respectively.

5.3.3 Limitations of LQG controller

The main limitations associated with the LQG formulation for the prototype DACS are: the need for *a priori* tuning of the weighting matrices, the inability to explicitly account for physical operating constraints, and difficulties in addressing model uncertainty. To achieve the desired control objectives, the weighting matrices are generally tuned through a process of trial-and-error. This method of tuning requires knowledge of the expected disturbances in addition to the structural model and must be completed before the control device is deployed. Furthermore, without a systematic approach to account for operating constraints such as the EMD stroke limit and peak UGV tire force, the weighting matrices must be designed to ensure the position command and resulting control force remain the physical limitations of the prototype device. This leads to a conservative controller design that inevitably under-utilizes the capacity of the device during day-to-day operations. In some applications a saturation function is used to clip the command signal at a prescribed limit; however for the prototype system, saturating the position command may result in abrupt changes in acceleration that generate unwanted inertial forces. Furthermore, saturation can only be applied to command signals and thus does not address the UGV tire force limitations. Lastly, the LQG formulation does not provide robustness to the uncertainty in the UGV or EMD models and does not address the potential for errors in the structure model.

5.4 Model predictive control

In general, MPC represents a collection of controllers that rely explicitly on the use of a model to predict the future behaviour of the system [43]. In MPC, an optimal sequence of control actions is solved for over a finite horizon by minimizing a cost function subject to prescribed constraints. When formulated using a quadratic cost function for a linear plant model without constraints, the MPC formulation reduces to an LQG control problem [106]. Therefore, many of the benefits associated with LQG control, specifically the ability to tune the trade-off between control performance and control effort, are also present in MPC formulations. Furthermore, MPC offers two key advantages over linear quadratic control; namely a method to systematically address physical operating constraints and the ability to model time-varying constraints and weighting matrices in the cost function. Unlike LQG control where the optimal state feedback gains are determined *a priori* and held constant, MPC algorithms solve a constrained optimization problem

at every time iteration to determine new feedback gains for the subsequent time step. A direct consequence of this approach is the ability to incorporate constraints on the control input or system states and vary the weighting matrices according to a prescribed algorithm. These properties are particularly attractive for the prototype DACS which has multiple operating constraints and could be tuned in real-time to maximize device utilization.

5.4.1 MPC formulation

MPC schemes determine a sequence of optimal control inputs by solving a constrained, finite-horizon optimization problem. In most cases, a receding horizon is used where only the first control action from the sequence is applied to the system and the optimization is repeated in the subsequent time step after incorporating current measurement information. Central to the performance of any MPC implementation are the prediction model and state estimator, which are used to forecast the future behaviour of the system. Figure 5.9 provides a schematic of the general MPC formulation. At the current time step k, the state estimator predicts the current system states for the prediction model which are then used to propagate the system forward (i.e., estimate future system states) over the prediction horizon of length h_p. Given the future state estimates, the optimization problem becomes one of identifying the sequence of optimal control inputs over a prescribed control horizon of length h_m such that a specified cost function is minimized. As shown in Figure 5.9, the control and prediction horizons need not be of equal length. In fact, a common technique known as move blocking can reduce the size of the optimization problem by holding the control input constant for the $h_p - h_m$ steps beyond the control horizon.

The constrained optimization problem has two main components: a cost function to be minimized and a set of operating constraints bounding the optimization. The cost function can be constructed to penalize the error between predicted and targeted outputs, the error between a particular state and its desired set-point, the magnitude or rate of change of the control input, or any combination thereof. For structural control applications, a quadratic cost function penalizing non-zero system states and the level of control input is commonly used such that weighting matrices can be tuned to achieve a desired control objective. As such, the cost function is given by:

$$J(k) = \sum_{j=0}^{h_p-1} z(k+j)^T \mathbf{W}_z z(k+j) + \sum_{j=0}^{h_m-1} u(k+j)^T \mathbf{W}_u u(k+j) + z(k+h_p)^T \mathbf{W}_\infty z(k+h_p) \quad (5.25)$$

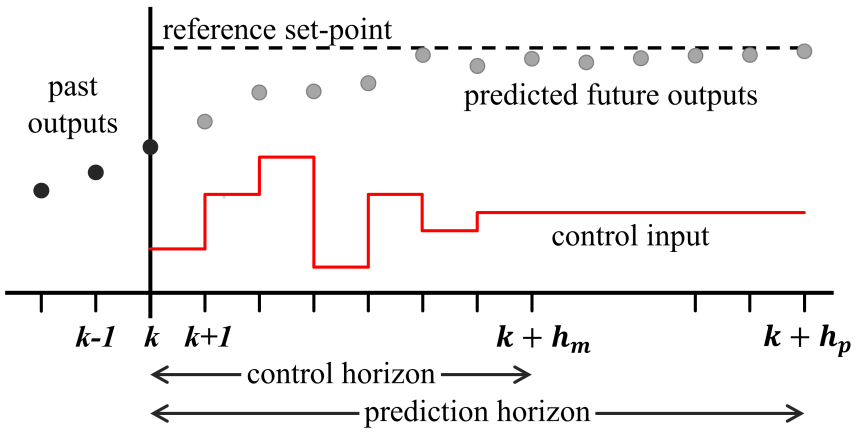

Figure 5.9: Schematic of general MPC scheme

where $\mathbf{W}_z$ and $\mathbf{W}_u$ are weighting matrices penalizing the non-zero system states and the control input respectively and $\mathbf{W}_\infty$ is the terminal state weighting matrix. The variables h_p and h_m represent the lengths of the prediction and control horizons respectively.

Given the cost function, constraints acting on the controlled inputs, system states, or system outputs can be modelled mathematically and included in the optimization problem to ensure the behaviour of the system operates within a desired range. These constraints can be modelled as either hard or soft constraints depending on the implication of violation. Hard constraints are inviolate and generally only applied to controlled variables where command saturation can be used. Applying hard constraints on system states or outputs may lead to infeasible solutions if the threshold is exceeded at some point over the prediction horizon. Soft constraints offer more flexibility by prescribing a threshold and penalty function that only applies when the threshold is exceeded. In this way, soft constraints permit violation under the condition that the amount the threshold is exceeded is heavily penalized in the objective function to bring the system back to the desired range. Soft constraints can also be modelled with a maximum violation which in effect superimposes a hard limit on the amount the threshold can be exceeded.

The quadratic cost function, together with any modelled constraints, form a constrained quadratic programming optimization problem that must be solved at each time step to determine the optimal state feedback gains. There are a number of methods and solvers available to solve such problem; however consideration must be given to the computation time required for each

solution in order to implement MPC schemes in real-time control applications.

5.4.2 Implementing MPC for prototype device

There are three key challenges related to the implementation of an MPC scheme for the prototype DACS: modelling physical operating constraints, incorporating adaptability through time-varying weighting matrices, and computational efficiency for real-time execution. Each of these challenges are addressed next.

Modelling constraints: The physical operating constraints for the prototype device include the EMD stroke length, which is limited to ±75 mm, and the peak force in the UGV tires, which is limited to ±400 N. Both constraints are of high importance as violating the EMD stroke limitation will cause the auxiliary mass to collide with the end-of-stroke limits and damage the EMD while exceeding the UGV tire force limitation will cause the tires to slip and destabilize the control system. Implementing the MPC scheme using the ISM approach provides direct computation of the desired EMD position command. Thus, the stroke limitation can be modelled directly using a hard constraint on the control input. Given a control horizon of length h_m, the EMD stroke constraint is modelled as:

$$-75 \text{ mm} \leq p_c(k+j) \leq 75 \text{ mm} \quad , \quad j = 0, 1, 2, \ldots, h_m - 1 \tag{5.26}$$

By virtue of the hard constraint, any desired position commands that exceed ±75 mm will be saturated to prevent end-of-stroke collisions. An important consideration for this constraint is that abrupt changes in acceleration caused by position saturation will introduce unwanted impulsive forces into the system which may affect the control performance. An alternative solution involves replacing the hard constraint with a soft constraint such that the position commands are penalized as they approach the limit thereby greatly reducing the likelihood of saturation. For example, the soft constraint can be designed with a threshold of ±65 mm and maximum violation of ±10 mm such that any position commands beyond 65 mm will be penalized in the cost function. The use of a quadratic penalty function will ensure the penalty is increased for larger violations while the maximum violation of 10 mm effectively imposes a hard constraint at ±75 mm.

Modelling the UGV force constraint is less direct since the interface force in the tires is not a controlled variable, system state, nor measured output. Thus, in order to model a constraint on the UGV tire force, the force must first be appended as an additional system output and estimated

from the system states. Furthermore, the ±400 N capacity must be modelled as a soft-constraint to avoid infeasible solutions during the optimization process. Soft constraints are defined by a threshold, maximum allowable violation, and penalty function. For the UGV tire force, the threshold is set to a safe value such that the sum of the threshold and maximum violation does not exceed the physical ±400 N limit. Consider a threshold of 300 N with a maximum violation of 100 N. Provided the tire force is below ±300 N, the soft constraint has no impact on the cost function; however, if the estimated tire force exceeds the threshold, a quadratic penalty is applied to the magnitude of exceedance. Note that with a maximum violation of 100 N, the maximum permissible tire force is capped at 400 N as required. The soft constraint for the UGV tire force is given by:

$$0 \leq \check{f}_t \leq 100 \text{ N} \quad , \quad \check{f}_t(k) = \begin{cases} |f_t| - 300 \text{ N} & \textit{if } |f_t| \geq 300 \text{ N} \\ 0 & \textit{otherwise} \end{cases} \tag{5.27}$$

where $\check{f}_t$ denotes the absolute magnitude of the UGV tire force beyond the specified 300 N threshold. Combining these constraints with the quadratic cost function in Equation 5.25 yields the following MPC formulation:

$$\begin{aligned} J(k) = & \underbrace{\sum_{j=0}^{h_p-1} z(k+j)^T + \mathbf{W}_z z(k+j) + \sum_{j=0}^{h_m-1} p_c(k+j)^T \mathbf{W}_{\boldsymbol{u}} p_c(k+j) \ldots}_{\textit{stage cost}} \\ & + \underbrace{z(k+h_p)^T \mathbf{W}_\infty z(k+h_p)}_{\textit{terminal cost}} + \underbrace{\sum_{j=0}^{h_p-1} \check{f}_t(k+j)^T \mathbf{W}_f \check{f}_t(k+j)}_{\textit{cost for violating soft constraint}} \\ \textit{such that} \quad & -75 \text{ mm} \leq p_c(k+j) \leq 75 \text{ mm} \quad \textit{for} \quad j = 0, 1, 2, \ldots, h_m - 1 \\ & 0 \leq \check{f}_t(k+j) \leq 100 \text{ N} \quad \textit{for} \quad j = 0, 1, 2, \ldots, h_p - 1 \end{aligned} \tag{5.28}$$

where $\mathbf{W}_f$ penalizes violation of the UGV tire force soft constraint.

Time-varying cost function: A distinct advantage of MPC over LQG control is the ability to incorporate time-varying weighting functions and constraint equations. This adaptability – a direct result of solving the optimization problem at each iteration – is well suited for the prototype DACS where online tuning can maximize device utilization by adjusting to the current conditions for the particular structure. To demonstrate this capability, a utilization-based algorithm is used to

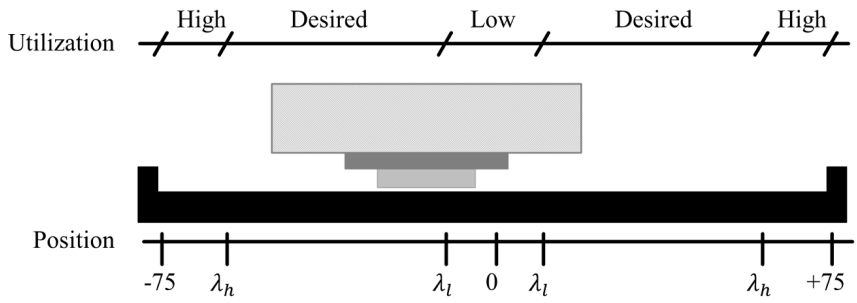

Figure 5.10: Utilization thresholds for EMD stroke

adjust the penalty on the control input. In general, if low utilization is detected, the weighting on the control input will be reduced to improve performance; meanwhile, detecting high utilization will trigger an increase in the penalty weighting to ensure the operating constraints are not violated. The sequence of optimal EMD position commands is used to compute two separate metrics that make inference on the device utilization. The first metric quantifies the extent to which the full stroke capacity of the device is utilized, while the second metric monitors extended periods of low stroke to suggest low utilization. It should be noted that this is a simple method to quantify utilization and other data such as the estimated force or an energy variable could also be used to enhance the metrics. Each metric has a prescribed threshold that together divide the EMD stroke into three ranges: high utilization when exceeding the upper threshold λ_h, low utilization when below the lower threshold λ_l, and desired utilization when operating between the thresholds. Figure 5.10 overlays the thresholds on a schematic of the EMD stroke. The regions are designed to prevent under-utilization with consideration for the risk of exceeding the allowable EMD stroke. The first metric θ_h is used to monitor high utilization and is calculated at each time step by summing over the control horizon an exponentially weighted score for each position command greater than the upper threshold. Specifically, this metric is computed as:

$$\theta_h(k) = \sum_{j=1}^{h_m} \epsilon_h(j) \quad , \quad \epsilon_h(j) = \begin{cases} \exp\left[\alpha_h \left(|p_c(j)| - \lambda_h\right)\right] & \text{if } |p_c(j)| - \lambda_h \geq 0 \\ 0 & \text{otherwise} \end{cases} \tag{5.29}$$

where h_m represents the number of steps in the control horizon and α_h is a tunable rate parameter. If the device is considered to be in the high utilization zone (i.e., $\theta_h > 0$), the magnitude of $\mathbf{W_u}$ is increased as a function of the metric θ_h. The second metric, denoted θ_l, runs in tandem with the high utilization metric to detect periods of low utilization. This metric is configured differently

to account for the fact that oscillating position commands passing through the low utilization zone do not necessarily indicate low utilization. In this case, the metric is computed based on the maximum absolute EMD position command over the control horizon. If the maximum absolute position command falls within the low utilization range, the difference between the maximum command and the lower threshold is exponentially weighted to yield the metric:

$$\theta_l = \begin{cases} \exp\left[\alpha_l \left(\lambda_l - \max\left\{|p_c(j)|\right\}\right)\right] & \textit{if } \lambda_l - \max\left\{|p_c(j)|\right\} \geq 0 \textit{ for } j = 0, 1, \ldots, h_m \\ 0 & \textit{otherwise} \end{cases} \tag{5.30}$$

where α_l is a tunable rate parameter. If the device is considered under-utilized (i.e., $\theta_l > 0$), the magnitude of $\mathbf{W_u}$ is reduced as a function of the metric θ_l. Furthermore, to avoid over-tuning by changing the penalty too frequently, the algorithm includes provisions to require persistent high or low utilization before triggering an update in the weighting matrix. For the prototype system, the low utilization metric must be greater than zero for ten consecutive iterations before triggering a decrease in the control input penalty.

Computational efficiency: A well-known drawback of MPC is the heavy computational demands associated with solving the constrained optimization problem at every time step. This requirement has limited the application of MPC to relatively slow processes or small systems [40]. To be a feasible control solution for deployable systems, the algorithm must be capable of executing in real-time. Furthermore, the controller must also be self-contained and executable on an on-board controller such as the cRIO used in the prototype. To achieve this, the MPC scheme is formulated using an open source toolkit for automatic control and dynamic optimization (ACADO) [107]. The ACADO toolkit is a software environment with a collection of algorithms for various control and optimization applications. The toolkit, provides general frameworks for a wide range of direct optimal control algorithms and features a number of efficiently implemented Runge-Kutta and backward differential formula integrators for fast simulation of differential and algebraic equations. MPC is one of four problem classes supported by the toolkit. This class, which can also be used for online state estimation, has been designed to repeatedly solve parameterized optimization problems such as the one described in Equation 5.28. Figure 5.11 provides an flow-chart highlighting the end-to-end process from formulation to implementation of the MPC algorithm with the ACADO toolkit.

A convenient feature of the ACADO toolkit is a MATLAB interface which allows problems formulated in MATLAB to communicate with the ACADO code base. Furthermore, the toolkit

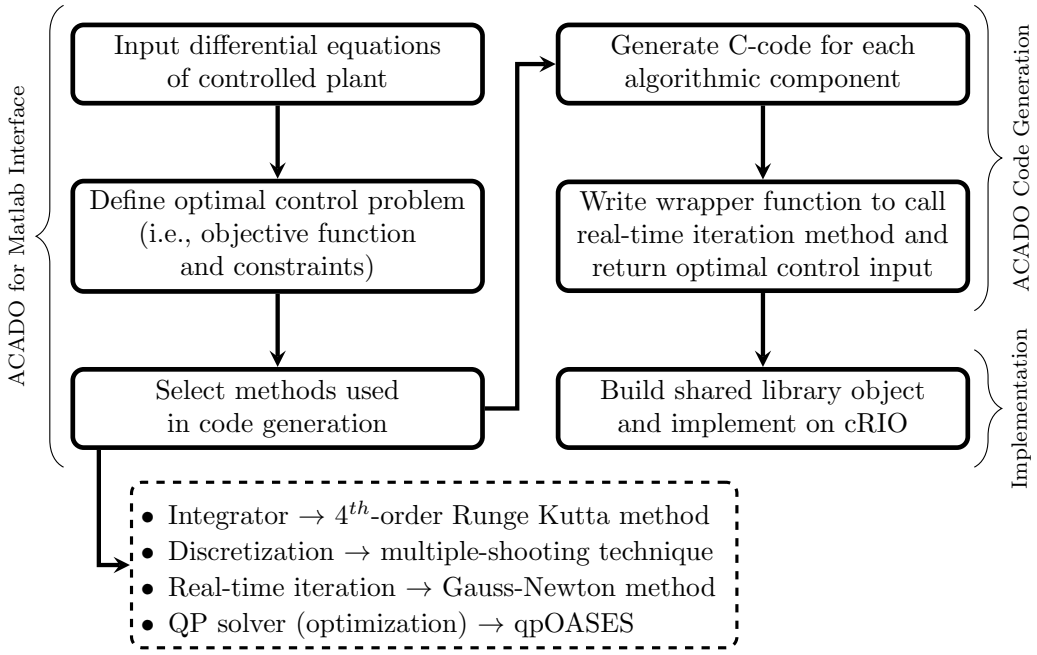

Figure 5.11: Overview of the process for implementing MPC using the ACADO toolkit

also includes a built-in code generation tool which can be used to export stand-alone, highly efficient, optimized code suitable for deploying on the cRIO. The exported code achieves its performance by implementing the Gauss-Newton Hessian approximation within its real-time iteration scheme and applying shooting techniques for the discretization of the continuous time differential equation of the plant [108]. These techniques yield a large, yet sparse quadratic problem, that is first condensed and then solved using qpOASES, a dense linear algebra quadratic programming solver employing the active set method [109]. The code generation tool generates a MATLAB executable as well as a main C++ file supported by a library of C-code to solve the optimization problem. The toolkit has the capability to parameterize variables such as constraints and objective function weights and thus supports the use of the utilization-based algorithm that redefines the weighting matrix for the control input based on the described metrics. It should be noted that only weighting matrices or constraint variables can be modelled as time-varying parameter inputs while the system model, prediction horizon, and solution method remain fixed after generating the code.

5.4.3 Limitations of MPC controller

The heavy computational demand is the main factor restricting the use of MPC. Although there are a variety of methods to reduce computations, such as shortening the prediction and control horizons, increasing the time step, or applying model reduction techniques, each method is generally associated with a trade-off in performance. Moreover, despite a combination of these efforts, large models may still experience computational delays beyond the largest possible time step for practical implementations. The prototype DACS not only augments the plant model, but also introduces hard and soft constraints that increase the complexity of the problem. Using the ACADO code generation tool described above, the prototype can be integrated with small structure models on the order 3 to 5 DOF and implemented in real-time on the cRIO. Larger structure models or the use of any additional constraints may require special consideration to run in real-time. A second limitation of the above MPC formulation is difficulty in addressing potential uncertainty in both the structure or controller models. Since the controller is designed based on the nominal DACS model and structure model, the presence of model errors may reduce performance or even lead to instabilities if the variance between the true and believed models is significant.

5.5 H_∞ robust control

The application of robust control theory is motivated by the ability to directly address plant uncertainties in the controller formulation. The robustness of a control system refers to the stability of the closed-loop system under both structured and unstructured perturbations [110]. For the prototype system, the linear UGV and EMD models contain some degree of uncertainty due to non-linear effects, modelling assumptions, and/or experimental curve fitting. For the UGV model, the uncertainty is frequency dependent due to the fact an inherently non-linear system is approximated using a linear model. Unlike the LQG and MPC formulations which design a controller based solely on the nominal system models, robust controller design requires the control requirements to be simultaneously satisfied over the entire class of systems. H_∞ control theory provides a convenient framework for robust controller design. The premise of H_∞ control is to design a controller such that the infinity norm of the transfer function from exogenous inputs (i.e., external forces) to regulated outputs (i.e., collection of states and control inputs) is

minimized. The H_∞ norm of a closed loop system can be viewed as the upper limit of the ratio from the RMS of the output to the RMS of the input and thus gives a measure of the worst case response over the entire class of system models and input disturbances. The ability to directly model uncertainty is significant in DACS applications. In addition to the inherent uncertainty contained in the DACS models, the model of the structure in which it is being deployed to control is generally not known precisely and derived based on estimated parameters. As such, achieving a controller that is also robust to uncertain structure models is beneficial.

5.5.1 H_∞ formulation

The formulation for an H_∞ controller is best described using a generalized plant model. Consider the following state-space equations for a generalized plant P_g:

$$P_g : \begin{cases} \dot{\boldsymbol{x}}_g &= \mathbf{A}\boldsymbol{x}_g &+ \mathbf{B}_1\boldsymbol{\omega}_g &+ \mathbf{B}_2\boldsymbol{u}_g \\ \boldsymbol{z}_g &= \mathbf{C}_1\boldsymbol{x}_g &+ \mathbf{D}_{11}\boldsymbol{\omega}_g &+ \mathbf{D}_{12}\boldsymbol{u}_g \\ \boldsymbol{y}_g &= \mathbf{C}_2\boldsymbol{x}_g &+ \mathbf{D}_{21}\boldsymbol{\omega}_g &+ \mathbf{D}_{22}\boldsymbol{u}_g \end{cases} \tag{5.31}$$

where $\boldsymbol{\omega}_g$ and $\boldsymbol{u}_g$ denote the exogenous and control input vectors respectively and P_g can be more compactly written as:

$$P_g(s) = \left[\begin{array}{c|cc} \mathbf{A} & \mathbf{B}_1 & \mathbf{B}_2 \\ \hline \mathbf{C}_1 & \mathbf{D}_{11} & \mathbf{D}_{12} \\ \mathbf{C}_2 & \mathbf{D}_{21} & \mathbf{D}_{22} \end{array}\right] \tag{5.32}$$

Two output equations are used in this model to distinguish between the measured outputs, denoted $\boldsymbol{y}_g$, which are treated as inputs to the controller and the regulated outputs, denoted $\boldsymbol{z}_g$. Figure 5.12 contains the block diagram description of the generalized plant P_g controlled by a feedback controller K_g. The transfer function between the exogenous inputs and regulated outputs, referred to as the closed-loop performance channel, is given by:

$$\boldsymbol{z}_g = F_\ell(P_g, K_g)\boldsymbol{\omega}_g \tag{5.33}$$

where F_ℓ denotes the lower linear fractional transformation and is defined as:

$$F_l : G_{z_g\omega_g}(P_g, K_g) = P_{g,11} + P_{g,12}K_g(\mathbf{I} + P_{g,22}K_g)^{-1}P_{g,21} \tag{5.34}$$

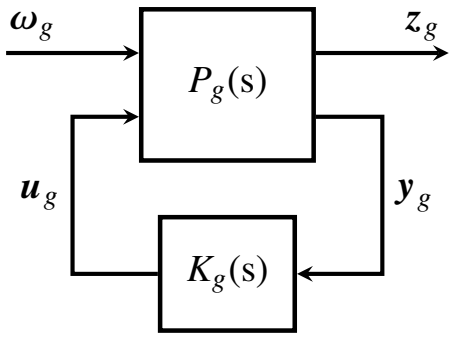

Figure 5.12: Generalized plant model for H_∞ controller formulation

Details pertaining to linear fractional transformations are provided in Appendix C. The control objective is thus to design a feedback controller K_g such that F_l is minimized. In H_∞ control, the controller is found by minimizing the infinity norm of the performance channel. Mathematically, this can be expressed as:

$$\text{minimize} \left\| G_{z_g \omega_g}(P_g, K_g) \right\|_\infty \tag{5.35}$$

subject to the condition that the controller K_g stabilizes the plant P_g internally. Basic H_∞ algorithms solve a suboptimal version of the controller design problem [111]. The suboptimal version involves designing a controller such that

$$\left\| G_{z_g \omega_g}(P_g, K_g) \right\|_\infty < \gamma_g \tag{5.36}$$

for a given value of $\gamma_g > 0$. The motivation for designing suboptimal controllers stems from the fact the optimal closed loop transfer matrix $G_{z_g \omega_g}$ can be shown to have a constant largest singular value over the complete frequency range. Thus the optimal controller is not strictly proper and the optimal frequency response to the cost output does not roll off at high frequencies [53, 111]. Furthermore, in cases where there is more than one control variable or more than one sensor variable, the optimal H_∞ controller is generally not unique. Suboptimal design methods use a binary search to determine the level of optimality (i.e., measured by the parameter γ_g). Once the value of γ_g has converged within a specified tolerance, the H_∞ controller is designed using Youla parameterization or Riccati-based approaches [111].

The generalized plant P_g in Figure 5.12 may contain frequency domain descriptions of filters and weighting functions to achieve the desired control performance. Mixed-sensitivity H_∞ controllers provide a closed loop response according to design specifications such as model

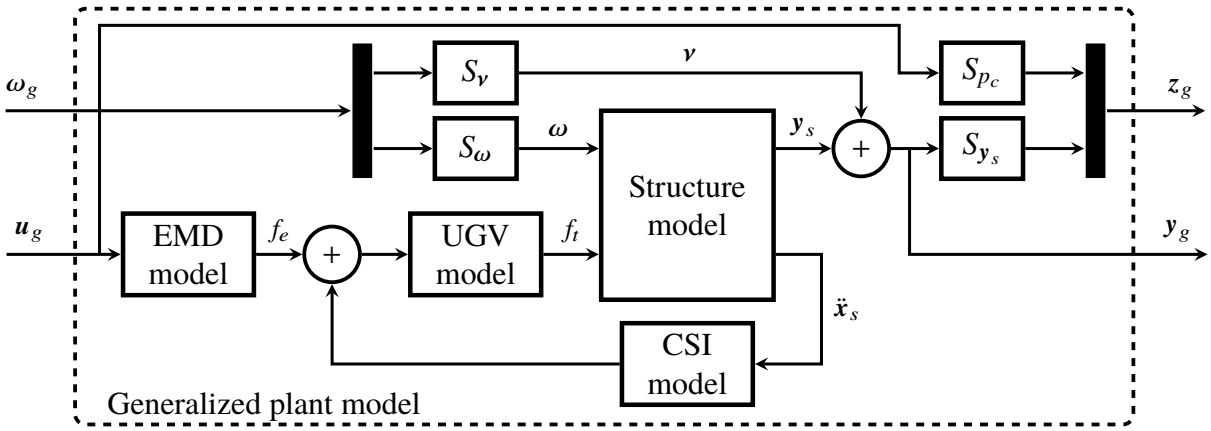

Figure 5.13: Generalized plant model with prototype device for H_∞ controller design

uncertainty, frequency-dependent disturbance attenuation, and control bandwidth. For example, weights can be added to the elements of z_g to fix the frequency range over which an element is minimized.

5.5.2 Implementing robust control for prototype device

Implementing an H_∞ controller for the prototype DACS requires modelling the entire closed loop system as a generalized plant and therefore the ISM approach must be followed. Figure 5.13 contains the block diagram description of the generalized plant model for the prototype device controlling an arbitrary structure. The feedback interaction dynamics are contained in the CSI block while the prototype DACS is represented by the EMD and UGV blocks. For simplicity, the output from the structure model is assumed to be the state vector containing nodal displacements and velocities. In practical applications where nodal accelerations are measured, a Kalman filter can be included to estimate the state vector which is then treated as the true state vector for implementation purposes. The exogenous input ω_g contains the vector of external disturbances ω and vector of measurement noise ν. This input signal is partitioned accordingly and passed through separate sensitivity weighting filters, denoted S_ω and S_ν respectively, to shape and scale the signals. The regulated output, denoted z_g contains the weighted structural states and weighted control input. The states are weighted by the sensitivity function S_{y_s} while the control input is

weighted by the sensitivity function S_{p_c} to achieve the desired control performance. The two key implementation challenges include accurately modelling the uncertainty associated with the EMD and UGV system models and designing the sensitivity functions to achieve the desired control performance.

Modelling DACS uncertainty: The uncertainty associated with the UGV and EMD models was discussed in Chapter 4 and is illustrated in Figure 4.5 and Figure 4.9 respectively. As shown, the estimated system models lie within their respective ranges of experimental FRFs and were designed to minimize the impact of modelling errors. In the context of uncertain dynamical systems, these best-fit approximations are referred to as nominal models while the range of experimental FRFs represent the expected level of uncertainty. In order to take such uncertainty into account, uncertain system models – containing a nominal model and a set of models that is guaranteed to contain the system uncertainty – must be derived. There are two common modelling approaches for incorporating uncertainty: additive uncertainty modelling and multiplicative uncertainty modelling. For a given nominal model $H_{j,i}$, the multiplicative uncertainty approach models the uncertain system $\tilde{H}_{j,i}$ as:

$$\tilde{H}_{j,i} = H_{j,i}(1 + S_{j,i}\Delta) \tag{5.37}$$

where $S_{j,i}$ is a frequency-dependent weighting function and Δ is an uncertain, stable, linear time invariant (LTI) system model. In this case, the weighting function describes the percentage of variation between the nominal model and worst-case models and thus is particularly useful when the gain is uncertain. On the other hand, additive uncertainty describes the absolute magnitude of variation between the nominal model and worst-case model. Additive uncertainty is commonly used when a bounded neighbourhood on the nominal model is known. Mathematically, additive uncertainty models are of the form:

$$\tilde{H}_{j,i} = H_{j,i} + S_{j,i}\Delta \tag{5.38}$$

Although both methods are valid alternatives for modelling the uncertainty associated with the DACS components, multiplicative uncertainty modelling is better suited for capturing the frequency-dependent gain uncertainty and will be discussed next. It should be noted that although multiple UGV and EMD system models were found by applying both experimental and analytical methods, only the experimentally identified models are considered for H_∞ controller design. This is merely done to simplify the explanation as the use of analytically derived models would follow an analogous procedure.

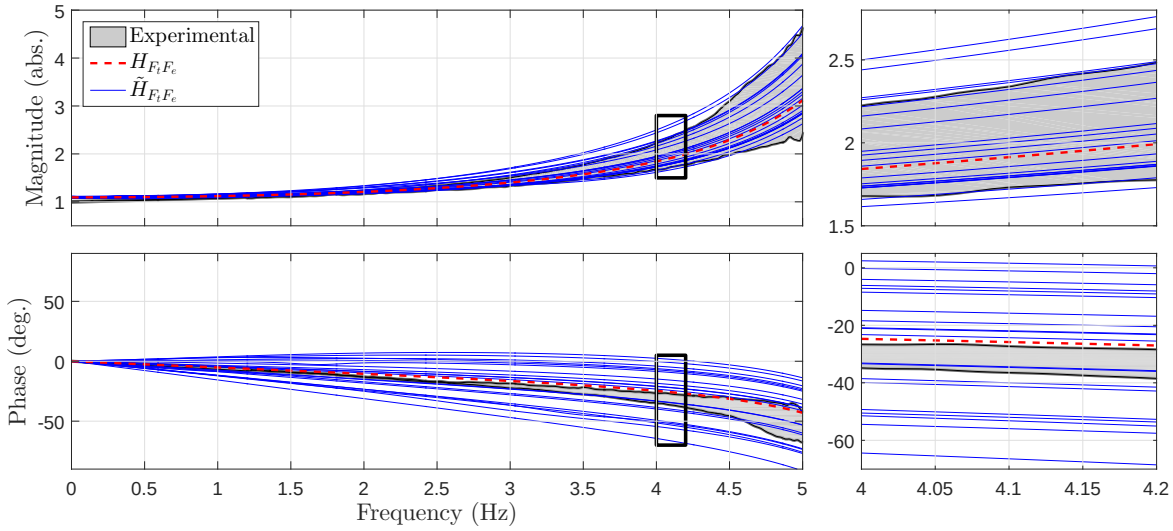

Figure 5.14: Bode plot of uncertain UGV model with experimental FRFs

Consider the nominal UGV model relative to the range of experimental FRFs. At low frequencies, below 2 Hz, the variation in the FRFs is relatively small (i.e., approximately ± 0.5 %) suggesting a low amount of uncertainty. However, beyond 2 Hz, the non-linear effects of the pneumatic UGV tires lead to considerable variation in the magnitude and phase of the estimated models constituting higher levels of uncertainty. For example, the range of experimental FRFs extend approximately ± 6 % and ± 35 % from the nominal model at 3 Hz and 5 Hz respectively. The weighting function for multiplicative uncertainty is designed based on the percentage of variation from the nominal model across the frequency range of interest and is expressed as:

$$S_{F_t F_e} = \frac{2s + 1.386}{s + 69.3} \tag{5.39}$$

Using this weighting function in Equation 5.37 yields the uncertain UGV model. Figure 5.14 plots 20 realizations from the uncertain UGV model, as well as the nominal model and range of experimental FRFs illustrated by a shaded region. As shown in Figure 5.14, a number of realizations from the uncertain UGV model fall beyond the range of the experimental transfer functions. This is achieved using a conservative weighting function to account for any measurement errors and/or time delays associated with the experimental testing. More importantly, since the range of experimental transfer function models are guaranteed to fall within the class of systems defined by the uncertain UGV model, the effects of non-linearity will be addressed within the H_∞ controller

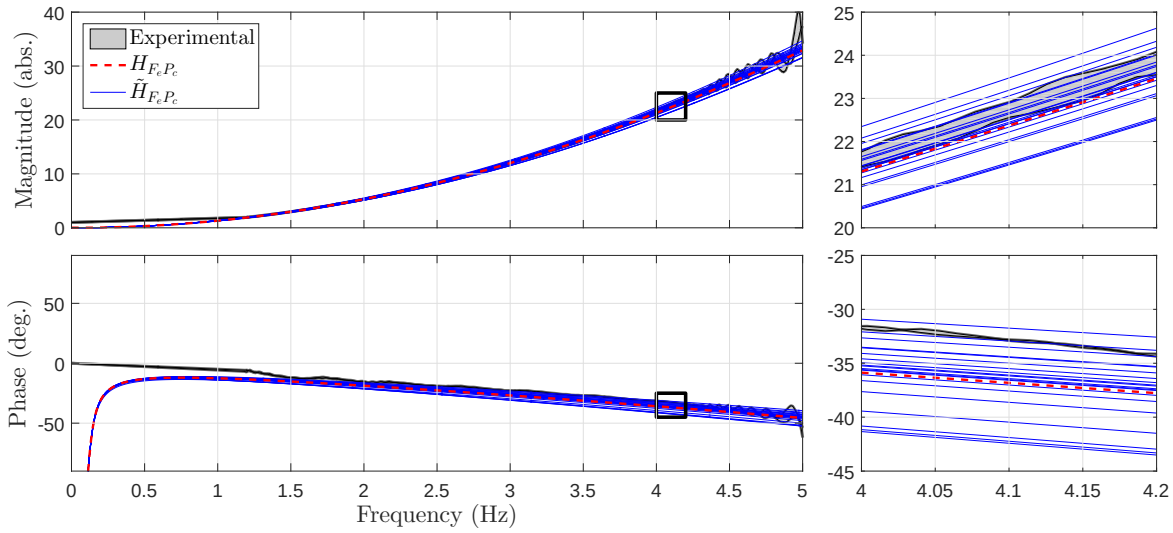

Figure 5.15: Bode plot of uncertain EMD model with experimental FRFs

formulation.

Quantifying the uncertainty associated with the nominal EMD model follows the same process. The percentage of variation from between the nominal model and experimental FRFs is identified across the range of frequencies and used to model the uncertainty weighting function. The weighting model for EMD uncertainty is given by:

$$S_{F_eP_c} = \frac{1.5s + 15.67}{s + 391.6} \tag{5.40}$$

Applying multiplicative uncertainty according to Equation 5.37 yields the uncertain EMD model. Figure 5.15 compares 20 realizations of the uncertain EMD model with the nominal model and range of experimental transfer function models. As intended, the uncertain EMD model includes all experimentally identified transfer function models and thus addresses the uncertainty associated with the nominal EMD model.

Tuning weighted sensitivity functions: In H_∞ control, the various sensitivity functions need to be tuned in order to achieve the desired control performance. The sensitivity functions perform frequency shaping and magnitude scaling on their respective signals to formulate the desired optimization problem. For structural control applications, the sensitivity function for the structural output (i.e., structural states) is generally designed as either a band-pass filter

or low-pass filter to target a narrow frequency bandwidth or multiple low-frequency modes respectively. In either case, frequency content outside the filter cut-offs is suppressed by the filter allowing the optimization to focus on a specific mode or modes. The DACS prototype, has an operating control bandwidth of 0 - 5 Hz. To optimize based on this range, a high-pass filter with a frequency cut-off of 5 Hz is used as the sensitivity function for the control input. In effect, this function penalizes high frequency content by reducing the relative weight on control frequencies within the operating bandwidth. In addition to frequency shaping, the relative gains associated with the output sensitivity and control sensitivity can be tuned to balance the trade-off between performance and control effort. On the other hand, the input sensitivity function and noise sensitivity function are used to shape and scale the external excitation and additive noise respectively. The design of these functions is based on the expected or worst-case excitation and types of sensors used for measurement. For example, narrow-band excitation can be considered by using a band-pass filter for the input sensitivity. Similarly, the expected level of sensor noise can be designed by appropriately scaling the magnitude of a constant gain transfer function.

5.5.3 Limitations of H_∞ robust controller

The main limitation of the H_∞ formulation is the inability to directly model the DACS operating constraints. As a result, the weighting sensitivities must be carefully designed to ensure the physical limitations are not exceeded under extreme conditions. Furthermore, since the formulation is based in the frequency domain, time domain specifications such as the EMD stroke limitations or maximum UGV tire forces are challenging to achieve. This limitation has been addressed through various means in the literature [112–114]. Although these methods show promising results, they are outside the scope of this thesis and the concept of constrained H_∞ is considered a potential direction for future work. The H_∞ formulation described above yields unstructured controllers which are generally of high order. This may lead to implementation issues and/or a large control effort requirement. One approach to overcome this is to employ model-reduction techniques. Alternatively a structured approach can be used in which the controller is parameterized and the H_∞ norm is minimized by optimizing the parameters.

Chapter 6

Achieving mobility

Regardless of the controller formulation, all structural control devices have an upper limit on control performance imposed by their position on the structure. The position of a control device is an important consideration in structural control since the controllability of a given mode of vibration depends on the relative magnitude of the mode shape at the location of the control force. To achieve the greatest control effect for a particular mode, the control device is positioned at or near the peak of the corresponding mode shape. The trade-off here is a considerable reduction in the control effect on other modes with may in fact reduce to no control effect if the location coincides with the node of a mode shape. For simple geometries where the response is dominated by a single mode of vibration, identifying the optimal position for the control device is straight-forward. However, determining the optimal control location for larger and mode complex structures is much less direct. This problem is particularly challenging for lightweight flexible structures such as aluminum pedestrian bridges where individuals or large groups of pedestrians could excite entirely different modes [92]. A common approach used in practice is to employ multiple control devices where each device is intended to suppress a different mode of vibration. Although this method is a valid long-term solution for permanent structures, the use of several fixed devices is largely redundant and impractical for applications with an immediate and temporary need for vibration mitigation. In such cases, this problem could be resolved by repositioning one or two devices to the appropriate locations as needed. This motivates the concept of mobility which is one of the key aspects of the DACS concept.

A mobile control system is characterized by the ability to autonomously position itself at

a desired location on a structure. This capability allows a single device to effectively control different modes of vibration by repositioning to appropriate locations. Moreover, this adaptability adds further capability to the overall controller which can be expanded to determine the optimal location for the control devices in addition to the control forces. For the prototype device, mobility is facilitated by the UGV and on-board vision sensors. Therefore, achieving autonomous positioning requires two of the most central tasks in autonomous robotics: localization and mapping. Localization describes the process of estimating the UGVs position as it navigates through a known environment while mapping involves the construction of a map of the environment based on estimated locations of features [86]. When navigating an unknown environment, the autonomous system must build a map of the environment while concurrently using the same map to localize itself [88]. This is a fundamental problem in mobile robotics and addressed using SLAM, and acronym for simultaneous localization and mapping [87]. This chapter summarizes the advantages of incorporating mobility in the DACS concept, discusses the corresponding impact on the overall control algorithm, and presents the implemented SLAM solution for autonomous navigation on unknown structures.

6.1 Advantages of mobility

Mobility is a key component in the DACS concept and eliminates the need to deploy several fixed devices by simply repositioning one or two mobile devices as required. The main advantages of mobility in the context of the vibration control are summarized as follows:

1. ***Ability to control different modes of vibration:*** Mobility allows repositioning of the prototype to effectively control different modes of vibration. This is particularly advantageous for lightweight flexible structures where the applied loading dictates the dominant mode.

2. ***Potential to control multiple modes simultaneously:*** By navigating to a position between mode-shape peaks the control device can influence the response of multiple modes simultaneously. In fact, mobility generates an additional control variable – namely the control device's position on the structure – which can be optimized to improve the overall control performance.

3. ***Facilitates deployability and simplifies implementation:*** A mobile control system with autonomous navigation can be deployed from a convenient location on the structure. This eliminates the need for manual installation at the final device location and could potentially speed up implementation and/or reduce disruption to service.

In addition to the aforementioned benefits from a vibration control perspective, a mobile control system can also be leveraged for system identification purposes. Having a control system readily available for immediate implementation is the main motivation for the DACS concept; however, in order to achieve this, an accurate structure model must be known *a priori*. In many cases, if a model of the structure does exist, it only approximates the physical system. Although the use of an approximated model may cause a reduction in control effectiveness, the efforts required to refine the model (i.e., through large-order finite element modelling or experimental system identification) can be both time consuming and expensive. An advantage of having a mobile control device deployed on the structure is the potential for rapid system identification by providing forced excitation at different locations. The collected input-output data could be used to update prior models or initiate new models. This added benefit reduces the dependence on an *a priori* model and raises the potential to use DACSs on unknown structures. Nevertheless, the use of the prototype device for system identification purposes is beyond the scope of this thesis and is addressed as an item for future study.

6.2 Augmenting the control algorithm

The primary function of existing structural control algorithms is to determine the optimal input to the control device. The models used in designing these algorithms reflect the position of the control device on the underlying structure which is a key constraint in the optimization. The concept of DACSs has introduced the idea of mobile control systems in which the position of the device can change in real time. As such, instead of treating the device location as a fixed parameter (i.e., constraint) in the plant model, the location can be modeled as an additional input variable in the optimization. In other words, the structural control algorithm can be augmented to determine the optimal location of the control force in addition to the control input, given the optimized location.

The ability to change the location of the control force on a given structure provides adaptability to respond to changes in the structure's properties or external loading patterns and thus offers potential to achieve improved control performance. The immediate trade-off with these benefits is a considerable increase in controller complexity. Part of this complexity stems from practical issues such as the time required to reposition the device and uncertain future behaviour. For example, the cost of repositioning must be weighed against the control benefit in the new location to justify the move. This is particularly relevant if the vibration control component is inactive while repositioning in which case frequent repositioning will greatly limit vibration control efforts. Although mobile control systems and thus optimizing the control location in real time is being presented for the first time, the problem of determining the optimal control location for a given structure has been studied by a number of researchers [115–117]. In these studies, the focus is on solving for the single best location for controlling the structure under all possible scenarios. The general limitation with these solutions is that they don't account for mobility which provides a means to change the position in response to the current scenario. Nevertheless, the existing literature on this topic provides a starting point for addressing the augmented control problem for DACS.

Developing a complete, fully augmented control algorithm for the prototype DACS is beyond the scope of this thesis and reserved as a direction for future work. However, for demonstration purposes and to study the impact of mobility on vibration control performance, a relatively simple augmented control framework is employed. In general, the control framework contains three components: sensing, position control, and vibration control. The sensing component involves continuous monitoring of the applied loading and/or dynamic response to inform the positioning and vibration control components. The positioning control component is divided into two main tasks; first, determine the optimal control position and second, navigate to that location. In this thesis, simple algorithms that predict the dominant mode of vibration are used to determine the optimal position from a set of predefined locations. Since the position is optimized amongst a constrained set of locations, multiple controllers are designed *a priori* based on the possible positions. As such, the vibration control component, involves pulling the appropriate feedback gains or control algorithm and determining the optimal control input. In should be noted that while navigating to the desired position, the vibration control component is paused. Specific details on the implemented augmented control frameworks are provided later in the descriptions of the experimental studies investigating the impact of mobility.

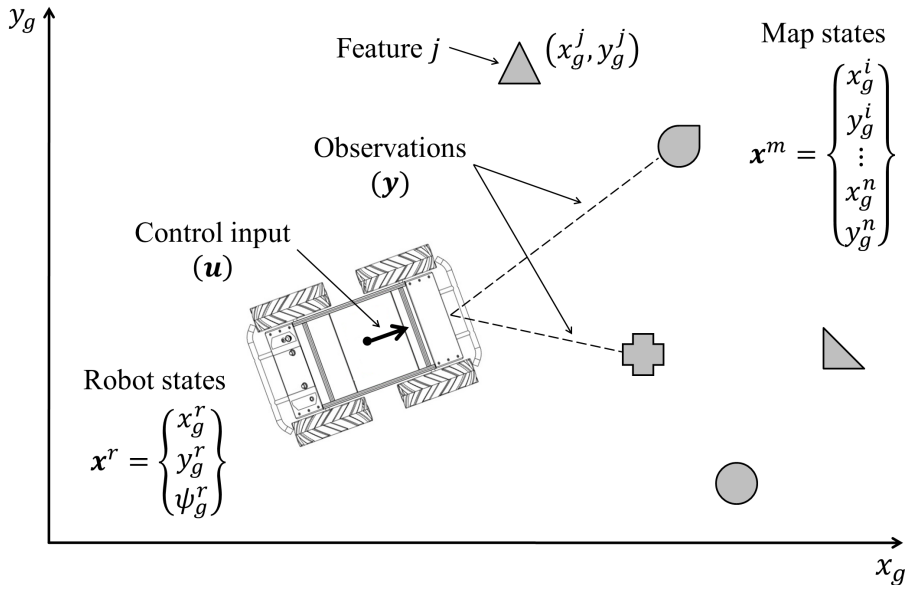

Figure 6.1: Sketch of the general SLAM problem

6.3 Simultaneous localization and mapping (SLAM)

In general, the SLAM problem is one of determining the position of the robot while concurrently building a map of the environment given control inputs and observations. This problem is sketched pictorially in Figure 6.1. The SLAM problem has been formulated and solved in many different forms [90]. In some cases, the solution method is selected based on the robotic system and available sensors however in most applications the type of environment in which the robot operates dictates the SLAM solution. One of the most widely used solution methods, given its suitability to a variety of environments, utilizes an extended Kalman filter (EKF) and is referred to as EKF-SLAM [89]. In EKF-SLAM, the standard two-step prediction-correction update procedure associated with the EKF is used to estimate the mobile robot's pose and coordinates of all known features in the environment. Prior to introducing the EKF-SLAM formulation, the probabilistic framework upon which the solution method rests, is discussed.

6.3.1 Probabilistic framework for SLAM

The probabilistic representation is one of several unique mathematical frameworks that have been used to model the SLAM problem. Although other representations have resulted in alternative solutions to the SLAM problem, there is no evidence that these alternatives outperform the probabilistic approach in practical scenarios [118]. As such, the probabilistic approach has become the most widely used and is considered standard [88]. The underlying assumption of the probabilistic framework is that the system state can be represented by a probability density function (PDF) at every time iteration k. The system state is composed of the vector of robot pose states (i.e., global coordinates and heading) denoted $\boldsymbol{x}^r$ and the vector of states for each feature in the map (i.e., global coordinates) denoted $\boldsymbol{x}^m$. Given all observations and control inputs up to time k, this probability distribution represents the joint posterior PDF of the system state and is defined as $p\left(\boldsymbol{x}_k|\boldsymbol{y}_{0:k}, \boldsymbol{u}_{0:k}, \boldsymbol{x}_0\right)$ where $\boldsymbol{x}$, $\boldsymbol{y}$ and $\boldsymbol{u}$ denote the system state vector, vector of observations, and vector of control inputs respectively [118]. When posed in this manner, the solution to the SLAM problem becomes one of solving for this posterior distribution (i.e., belief for the system state) at each time step.

The Bayes filter is the most general of many algorithms for calculating the posterior distribution in a probabilistic framework [86]. The Bayes filter operates recursively such that the believed state is first predicted based on information contained in past control inputs and observations and subsequently corrected using current observations. Mathematically, this sequential prediction-correction estimation scheme is defined by the following prediction and measurement update equations [88]:

Prediction update:

$$p\left(\boldsymbol{x}_k|\boldsymbol{y}_{0:k-1}, \boldsymbol{u}_{0:k}, \boldsymbol{x}_0\right) = \int p\left(\boldsymbol{x}_k^r|\boldsymbol{x}_{k-1}^r, \boldsymbol{u}_k\right) \times p\left(\boldsymbol{x}_{k-1}|\boldsymbol{y}_{0:k-1}, \boldsymbol{u}_{0:k-1}, \boldsymbol{x}_0\right) d\boldsymbol{x}_{k-1}^r \tag{6.1a}$$

Measurement update:

$$p\left(\boldsymbol{x}_k|\boldsymbol{y}_{0:k}, \boldsymbol{u}_{0:k}, \boldsymbol{x}_0\right) = \frac{p\left(\boldsymbol{y}_k|\boldsymbol{x}_k\right) p\left(\boldsymbol{x}_k|\boldsymbol{y}_{0:k-1}, \boldsymbol{u}_{0:k}, \boldsymbol{x}_0\right)}{p\left(\boldsymbol{y}_k|\boldsymbol{y}_{0:k-1}, \boldsymbol{u}_{0:k}\right)} \tag{6.1b}$$

where the terms $p\left(\boldsymbol{x}_k^r|\boldsymbol{x}_{k-1}^r, \boldsymbol{u}_k\right)$ and $p\left(\boldsymbol{y}_k|\boldsymbol{x}_k\right)$ are referred to as the motion model and observation model respectively. The motion model describes the probability distribution on state transitions while the observation model describes the probability of making an observation given a believed

state. A key simplifying assumption is that the robot follows a Markov process where the current robot pose depends only on the preceding pose and applied control action (i.e., the state transition of the robot is independent of the feature observations) [88].

The full SLAM solution is only required when neither the robot states nor map states are known. If a map of the environment is known, the problem reduces to one of localizing the robot within the map. As such, the known map states denoted $\bar{\boldsymbol{x}}^m$ are used within the estimation of the robot states and the goal becomes solving for the probability distribution $p\left(\boldsymbol{x}_k^r | \boldsymbol{y}_{0:k}, \boldsymbol{u}_{0:k}, \bar{\boldsymbol{x}}^m\right)$. On the contrary, if the robot state can be assumed to be known given reliable and accurate pose measurements from multiple sensors such as GPS units and IMU sensors, the problem reduces to one of constructing a map based on the observation data. Here the problem is reformulated such that the goal is to find the probability distribution $p\left(\boldsymbol{x}_k^m | \boldsymbol{y}_{0:k}, \boldsymbol{u}_{0:k}, \bar{\boldsymbol{x}}_k^r\right)$ where $\bar{\boldsymbol{x}}^r$ represents the known robot pose states [88].

6.3.2 EKF-SLAM formulation

The EKF is one particular implementation of the generic Bayes filter algorithm that can be used to solve the probabilistic SLAM problem. In EKF-SLAM, the posterior PDF (i.e., believed system state) is assumed to be a multivariate, Gaussian, normal distribution and thus can be characterized by a mean $\hat{\boldsymbol{x}}_{k|k}$ and covariance $\mathbf{P}_{k|k}$. The probability distributions for the motion model and the observation model in Equations 6.1a and 6.1b respectively can be rewritten using nonlinear state space equations with added Gaussian noise as:

$$p\left(\boldsymbol{x}_k^r | \boldsymbol{x}_{k-1}^r, \boldsymbol{u}_k\right) \Leftrightarrow \boldsymbol{x}_k = g(\boldsymbol{x}_{k-1}, \boldsymbol{u}_k) + \boldsymbol{\omega}_k \tag{6.2a}$$

$$p\left(\boldsymbol{y}_k | \boldsymbol{x}_k\right) \Leftrightarrow \boldsymbol{y}_k = h\left(\boldsymbol{x}_k\right) + \boldsymbol{\nu}_k \tag{6.2b}$$

where $\boldsymbol{\omega}$ and $\boldsymbol{\nu}$ represent the process noise and measurement noise vectors with covariances denoted by $\mathbf{R}_k$ and $\mathbf{Q}_k$ respectively [88]. However, the use of the nonlinear functions $g(\cdot)$ and $h(\cdot)$ violate the Gaussian properties of the posterior probability distribution and thus linear approximations are required. Using a first-order Taylor expansion, the non-linear motion model and observation models are approximated as:

$$g(\boldsymbol{x}_{k-1}, \boldsymbol{u}_k) \approx g(\hat{\boldsymbol{x}}_{k-1|k-1}, \boldsymbol{u}_k) + \mathbf{G}_k(\boldsymbol{x}_{k-1} - \hat{\boldsymbol{x}}_{k-1|k-1}) \tag{6.3a}$$

$$h(\boldsymbol{x}_k) \approx h(\hat{\boldsymbol{x}}_{k|k-1}) + \mathbf{H}_k(\boldsymbol{x}_k - \hat{\boldsymbol{x}}_{k|k-1}) \tag{6.3b}$$

where $\hat{\boldsymbol{x}}_{k-1|k-1}$ and $\hat{\boldsymbol{x}}_{k|k-1}$ denote the mean of the belief distribution at $k-1$ and mean of the prior belief distribution at k respectively. The term $\mathbf{G}_k = g'\left(\hat{\boldsymbol{x}}_{k-1|k-1}, \boldsymbol{u}_k\right)$ is the Jacobian of $g(\cdot)$ evaluated at the estimate $\hat{\boldsymbol{x}}_{k-1|k-1}$ while $\mathbf{H}_k = h'\left(\hat{\boldsymbol{x}}_{k|k-1}\right)$ is the Jacobian of $h(\cdot)$ evaluated at the estimate $\hat{\boldsymbol{x}}_{k|k-1}$ [86]. Linearizing the motion model and observation model implies the EKF-SLAM algorithm only approximates the Gaussian belief distribution. Nevertheless, since a Gaussian distribution can be characterized by a mean and covariance, the goal of the EKF is to efficiently estimate the mean and covariance opposed to computing the exact posterior.

The EKF-SLAM solution incorporates the two-step prediction-correction scheme. In the prediction update, the belief distribution for the robot pose states is updated given known control input. Since the belief is assumed to be Gaussian, this is accomplished by updating the mean and covariance of the distribution. In general, the features in the environment are assumed to be static. As a result, the vector of map states is not included in the prediction update and only the robot states and corresponding entries in the covariance matrix are updated. The prediction update equations are given by:

$$\hat{\boldsymbol{x}}^r_{k|k-1} = g\left(\hat{\boldsymbol{x}}^r_{k-1|k-1}, \boldsymbol{u}_k\right) \tag{6.4a}$$

$$\mathbf{P}^{rr}_{k|k-1} = \mathbf{G}_k \mathbf{P}^{rr}_{k-1|k-1} \mathbf{G}_k^T + \mathbf{R}_k \tag{6.4b}$$

In the correction update, measurements to features are used to improve estimates of both the robot states and map states. The degree to which the measurements are incorporated in the new state estimate is determined by the Kalman gain $\mathbf{K}_s$. The observation model is used to compute the difference between the actual and expected measurements. This error, calculated as $\boldsymbol{y}_k - h\left(\hat{\boldsymbol{x}}_{k|k-1}\right)$ is multiplied by the Kalman gain to correct the state estimates. The equations for the correction update are given by:

$$\hat{\boldsymbol{x}}_{k|k} = \hat{\boldsymbol{x}}_{k|k-1} + \mathbf{K}_{s,k}\left(\boldsymbol{y}_k - h\left(\hat{\boldsymbol{x}}_{k|k-1}\right)\right) \tag{6.4c}$$

$$\mathbf{P}_{k|k} = \left(\mathbf{I} - \mathbf{K}_{s,k}\mathbf{H}_k\right)\mathbf{P}_{k|k-1} \tag{6.4d}$$

where the Kalman gain is given by:

$$\mathbf{K}_{s,k} = \mathbf{P}_{k|k-1}\mathbf{H}_k^T\left(\mathbf{H}_k\mathbf{P}_{k|k-1}\mathbf{H}_k^T + \mathbf{Q}_k\right)^{-1} \tag{6.4e}$$

6.3.3 EKF-based localization

Once a sufficient map has been established using EKF-SLAM, the autonomous navigation problem reduces to localization. As shown in the probabilistic framework, the localization problem involves using a known map to estimate the robot pose states. Mathematically, this requires solving for the posterior probability distribution: $p\left(\boldsymbol{x}_k^r | \boldsymbol{y}_{0:k}, \boldsymbol{u}_{0:k}, \bar{\boldsymbol{x}}^m\right)$. To leverage the efforts towards implementing EKF-SLAM, an EKF-based localization algorithm is utilized on the prototype device. The prediction-correction updates provided for EKF-SLAM can be adopted for EKF-localization by reducing the state vector to the robot pose states and replacing the believed map states with the known feature locations. Incorporating these changes allows the same two-step prediction-correction scheme to be used to first predict the robot pose state and subsequently correct the estimate based on observations.

6.4 Implementing EKF-SLAM on the prototype device

One of the main advantages of a DACS is the ability to be deployed on a range of structures. Therefore, the implemented SLAM algorithm should be suitable for a variety of mapping environments and shouldn't rely on any structure-specific conditions. The EKF-SLAM solution defines a map based on a collection of uniquely identifiable features and thus is suitable for a range of unknown environments. Nevertheless, a number of challenges arise when implementing EKF-SLAM on civil infrastructure. These challenges stem from difficulties associated with identifying unique features as well as restricted exploration due to confined spaces. In order to implement the EKF-SLAM and EKF-based localization schemes, a motion model and a measurement model must be developed for the prototype device. The derivations for the motion and measurement models are presented next followed by a discussion on the methods used to overcome the key implementation challenges.

6.4.1 Motion model

The motion model is central to the prediction update and responsible for propagating the robot pose states given a control action. The motion model for the prototype DACS is derived from the kinematic model for a skid-steered UGV. Kinematic modelling of skid-steer vehicles has

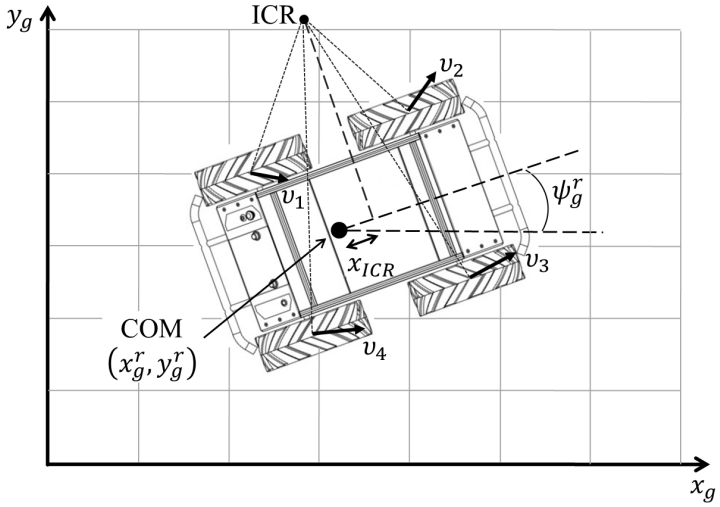

Figure 6.2: Coordinate systems for UGV motion model

been studied to varying degrees in the literature and has yielded a range of modelling approaches [119–121]. Nevertheless, the most commonly used kinematic model for the UGV is given by:

$$\begin{bmatrix} \dot{x}_g^r \\ \dot{y}_g^r \\ \dot{\psi}_g^r \end{bmatrix} = \begin{bmatrix} \cos\psi_g^r & x_{ICR}\sin\psi_g^r \\ \sin\psi_g^r & -x_{ICR}\cos\psi_g^r \\ 0 & 1 \end{bmatrix} \begin{bmatrix} v_x \\ \omega_g \end{bmatrix} \tag{6.5}$$

where x_g^r, y_g^r, and ψ_g^r denote the global coordinates and heading for the robot's pose. The linear and angular input velocity commands are represented by v_x and ω_g respectively and x_{ICR} is the projection of the instantaneous center of rotation (ICR) on the local x-axis. Figure 6.2 illustrates the local and global frames of reference and projection of the ICR. The ICR is the point about which the vehicle rotates at any given instant and thus, the projection of this point on the local x-axis describes the relationship between the angular velocity and the y-component of the local frame velocity. As such, the y-component of the local frame velocity, denoted v_y, is computed using:

$$v_y = -\omega_g x_{ICR} \tag{6.6}$$

For skid-steered vehicles such as the UGV used in the prototype, the location of the ICR and magnitude of the corresponding projection on the local x-axis depends on the ratio of forward to angular velocities. By assuming the ratio between the forward and angular velocities is constant,

the projection of this point on the local x-axis (i.e., x_{ICR}) is also assumed to be constant which considerably simplifies the motion model. For cases where the UGV travels predominantly in a straight line with minimal steering (i.e., pedestrian bridge applications), this assumption was shown to have negligible impact on the estimated robot pose. Based on the kinematic model in Equation 6.5, the non-linear motion model in discrete-time with a time step of dt is given by:

$$g(\hat{\boldsymbol{x}}^r_{k-1|k-1}, \boldsymbol{u}_k) = \begin{bmatrix} x^r_{g,k-1} + (v_{x,k}\cos\psi^r_{g,k-1} + \omega_{g,k}x_{ICR}\sin\psi^r_{g,k-1})dt \\ y^r_{g,k-1} + (v_{x,k}\sin\psi^r_{g,k-1} - \omega_{g,k}x_{ICR}\cos\psi^r_{g,k-1})dt \\ \psi^r_{g,k-1} + \omega_{g,k}dt \end{bmatrix} \tag{6.7}$$

Taking the partial derivative of Equation 6.7 with respect to the robot pose yields the corresponding Jacobian matrix:

$$\mathbf{G}_k = \begin{bmatrix} 1 & 0 & \left(-v_{x,k}\sin\psi^r_{g,k-1} + \omega_{g,k}x_{ICR}\cos\psi^r_{g,k-1}\right)dt \\ 0 & 1 & \left(v_{x,k}\cos\psi^r_{g,k-1} + \omega_{g,k}x_{ICR}\sin\psi^r_{g,k-1}\right)dt \\ 0 & 0 & 1 \end{bmatrix} \tag{6.8}$$

6.4.2 Measurement model

Dead reckoning methods, which rely solely on local measurements such as wheel encoders and IMUs suffer from drift due to the accumulation of erroneous signals. As such, in EKF-SLAM, absolute measurements to identified features are incorporated to correct this drift. The measurement model is used to calculate the expected measurement for a given feature based on the believed robot pose. This expected measurement is then compared with the actual measurement to correct the beliefs. The main challenge associated with incorporating observations involves synchronization of the measurements with the UGV states. In some cases, measurements from vision sensors experience time delay associated with processing the image and therefore may be used to correct the current state of the UGV which had been updated since the instant the images were recorded. For the prototype DACS, encoder data from the UGV and measurements to known features in the map from the Kinect sensors are used in the correction update. Although encoder information for skid-steered UGVs is fraught with errors caused by wheel slippage, given the vehicle travel is predominantly in a straight line the encoder measurements in the longitudinal (local x-coordinate) direction are only marginally biased by the slippage. The same does not apply

to the lateral (local y-coordinate) or UGV heading as thus only the longitudinal encoder position data is used in the update. Furthermore, to prevent the accumulation of error over large travel distances, the incremental encoder measurements are used opposed to the absolute data which is tracked by the UGV. In this way, instances of wheel slippage only affect the current update and are removed from memory for future updates. The measurement model for the incremental change in the local x-coordinate is given by:

$$h_{enc}\left(\hat{\boldsymbol{x}}^r_{k-1|k-1}, \hat{\boldsymbol{x}}^r_{k|k-1}\right) = \frac{x^r_{g,k} - x^r_{g,k-1}}{\cos\psi^r_{g,k-1}} \tag{6.9}$$

The forward and rear-facing Kinect sensors are used to detect known features in the environment and provide range and bearing measurements relative to the sensor's local reference frame. Experimental testing with the Kinect sensor revealed that relatively small features (approximately 0.2 m by 0.2 m in dimension) can be accurately detected up to 4 m away from the sensor; however, it was shown that measurement error began increasing beyond 3 m. Similarly, features can be detected across the full field of view of the sensor although image distortion near the edges of the field of view cause increases in measurement error. In an effort to reduce measurement error, raw measurements greater than 3 m or less than 0.5 m are rejected from the update. Figure 6.3 depicts a sketch of the measurement model for the Kinect sensors. Mathematically, the model contains range and bearing measurements to a unique point feature with believed coordinates $\left(x^i_g, y^i_g\right)$ and is expressed as:

$$h^i_{knct}(\hat{\boldsymbol{x}}_{k|k-1}) = \begin{bmatrix} \sqrt{\left(\delta^i_{x,k}\right)^2 + \left(\delta^i_{y,k}\right)^2} \\ \arctan\left(\frac{\delta^i_{y,k}}{\delta^i_{x,k}}\right) - \psi^r_{g,k} \end{bmatrix} = \begin{bmatrix} \gamma^i_{r,k} \\ \gamma^i_{b,k} \end{bmatrix} \tag{6.10}$$

where the global distance components are computed using:

$$\delta^i_x = x^i_{g,k} - x^r_{g,k} \tag{6.11a}$$

$$\delta^i_y = y^i_{g,k} - y^r_{g,k} \tag{6.11b}$$

Since each measurement depends on a single feature, measurement updates can be performed independently (i.e., one feature at a time.) Linearizing the above measurement model with respect to the UGV states and i^{th} feature states leads to the corresponding Jacobian matrix:

$$\mathbf{H}^i_{knct,k} = \begin{bmatrix} \frac{-\delta^i_{x}k}{\gamma^i_{r,k}} & \frac{-\delta^i_{y}k}{\gamma^i_{r,k}} & 0 & 0 & \dots & 0 & \frac{\delta^i_{x}k}{\gamma^i_{r,k}} & \frac{\delta^i_{y}k}{\gamma^i_{r,k}} & 0 & \dots & 0 \\ \frac{\delta^i_{y}k}{\left(\gamma^i_{r,k}\right)^2} & \frac{-\delta^i_{x}k}{\left(\gamma^i_{r,k}\right)^2} & -1 & 0 & \dots & 0 & \frac{-\delta^i_{y}k}{\left(\gamma^i_{r,k}\right)^2} & \frac{\delta^i_{x}k}{\left(\gamma^i_{r,k}\right)^2} & 0 & \dots & 0 \end{bmatrix} \tag{6.12}$$

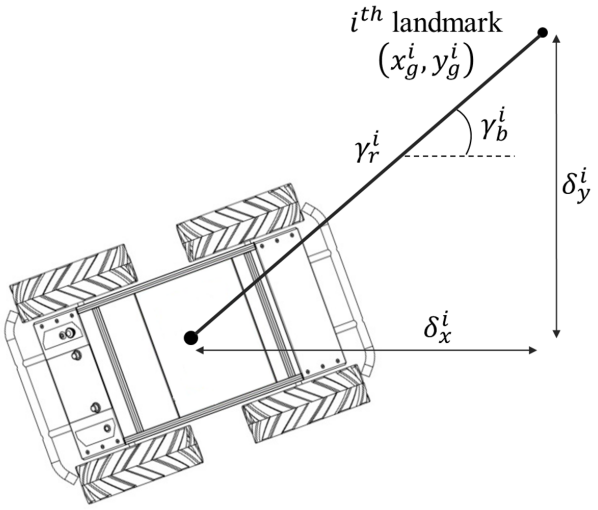

Figure 6.3: Schematic of measurement model for Kinect sensor

6.4.3 Implementation challenges

Although the field of autonomous robotics has experienced considerable growth over recent years, the specific application of SLAM to civil engineering structures for the purpose of vibration control is novel and is associated with unique challenges that must be addressed for successful implementation. For example, many lightweight pedestrian bridges are modular in nature and contain several repeated elements. Although this has a number of advantages from a structural design perspective, from a mapping and localization point-of-view the repeated structural elements produce identical features within the environment. Furthermore, exploration of bridge structures is generally confined to a straight line which limits the ability to observe features from different viewpoints and may lead to convergence issues in the map. Thus, the overarching goal is to develop a SLAM solution suitable for mapping a range of structures with sparse or repeated features in confined spaces. The three key challenges pertaining to the implementation of an EKF-SLAM solution for existing structures and specifically pedestrian bridges are: ensuring accurate feature extraction and data association, maximizing exploration in constrained environments, and achieving loop closure. In addressing these challenges, the SLAM solution method should be suitable for use on a range of structures. As such, the EKF-SLAM algorithm shouldn't rely on structure-specific properties or characteristics to achieve accurate results.

Feature extraction and data association: Feature extraction is the process of identifying distinguishable features in the environment that can be used to develop the overall map. The type of features that are extracted and corresponding map that is produced depends on both the type of sensors being used and the nature of the surrounding environment. Data association involves finding correspondences between the features that already exist in the global map and those that are currently visible to the UGV. When features are not simple points it is possible for them to appear different from different view-points, which is a fundamental problem in data association. The sparsity of physical elements and repetitive nature within modular structures compounds the existing challenges in feature extraction and data association. If the SLAM solution relies solely on the structure itself for mapping and ignores the surrounding environment which may not remain constant, features may only be derived from structural elements or permanent attachments. Using a feature extraction method designed to map individual structural elements, will be highly susceptible to false correspondences in data association. On the other hand, if all of the elements on one side of the bridge are grouped as a single line feature, the algorithm will lack measurement data to correct the longitudinal position of the UGV. To overcome these limitations and develop a feature extraction scheme that is suitable for a range of structures, individual tags containing unique augmented reality (AR) codes are placed on the structure. This standardizes the features, facilitates efficient data association, and significantly reduces the likelihood of false correspondences. The Kinect sensors mounted on the DACS can detect the AR codes using the RGB image and provide relative location information by incorporating depth information from the infrared transmitter. Figure 6.4 illustrates one possible setup where the AR codes are positioned on both sides of the bridge at each panel point. In EKF-SLAM, the number of states to be estimated is proportional to the number of features in the estimated map plus the robot pose states. As such, a trade-off exists between the number of tags added to the bridge and computational complexity. For example, if not enough tags are used there may not be sufficient measurement information for convergence; however, if too many tags are used, the processing time of each measurement may lead to time delays in the algorithm.

Exploration scheme: In any SLAM implementation, an exploration scheme is required to navigate the robot through the unknown environment and ensure the entire area is explored. For pedestrian bridge applications, a straight-forward exploration scheme that tracks the center-line of the bridge is considered to be the most effective. In this case, the UGV is commanded with a constant forward velocity and a proportional-derivative (PD)-controller is used to command

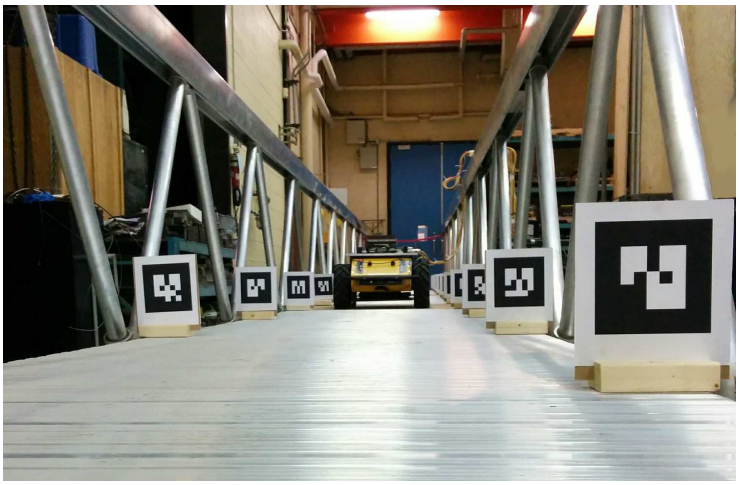

Figure 6.4: Use of AR tags to standardize features

angular velocity to correct the heading of the vehicle such that it tracks the desired trajectory. Given AR tags on both sides of the bridge, the desired trajectory is defined by the midpoint between two tags directly across from each other. As such, the desired trajectory is extended as additional features are detected. This process continues until the UGV reaches the opposite end of the bridge and no new features are identified. An advantage of this exploration method is that the placement of AR tags dictates the desired trajectory and therefore can be applied to a wide range of structures as well as confine the exploration to a portion of the structure.

Loop-closure: Loop closure is central to the convergence of the SLAM problem and is achieved when a feature is re-observed after significant travel. In EKF-SLAM, state uncertainty continues to grow until loop closure is achieved [86, 88]. Upon achieving loop closure, the estimates of all states improve based on the correlation information that is stored in the covariance matrix. Achieving full loop-closure on a pedestrian bridge with a forward facing sensor requires travel to the far end of the bridge and a return trip back to the starting point. Not only does this process require a large amount of time, it also results in a significant travel distance before achieving loop closure during which large amounts of uncertainty may accumulate. The loop-closure problem motivates the use the second, rear-facing Kinect sensor. When traveling forward, features are first extracted and initialized based on measurements from the forward-facing Kinect sensor. After continuing in the same direction, the same feature is re-observed, this time from the rear-facing sensor. As a result, a partial loop-closure is achieved for the features that have

been seen up to that point. Continuing in this fashion results in a series of incremental partial loop-closures that progressively improve the state estimates. It should be noted that the features or in this case AR tags must be visible from both directions. As such, double-sided AR tags are used for the prototype system.

6.5 Experimental validation

This section covers the experimental study that is carried out to verify the functionality of the EKF-SLAM solution for mapping existing structures. The physical structure considered in this study is a modular aluminum pedestrian bridge with a span of 16.76 m, width of 1.22 m and constructed in 1.52 m modules. Double-sided features (i.e., AR codes) are placed on both sides of the bridge deck and evenly spaced at 1.52 m along the length to coincide with the panel points.

6.5.1 Implementation

The described EKF-SLAM solution is implemented in MATLAB using the Robotics Systems Toolbox. A TCP link is used to establish communication between the EKF-SLAM algorithm and the on-board ROS-enabled laptop. All measurement information from the UGV and sensors is sent to the algorithm while the computed velocity input commands are returned to the ROS platform for execution. Synchronization of the measurements is achieved by predicting the future position and timing the collection of measurements to align with that particular instance. To start, the DACS is placed at one end of the bridge and programmed to travel with a constant forward velocity until the last feature is detected. The simple steering controller injected angular velocity to correct the UGV heading such that the robot tracks the center-line of the map as it is being created. The response from the steering controller is intentionally slow to minimize wheel slippage and associated errors in the prediction model. The noise models for the prediction and measurement updates are quantified experimentally prior to implementation by comparing the estimated pose and sensor measurements with known values.

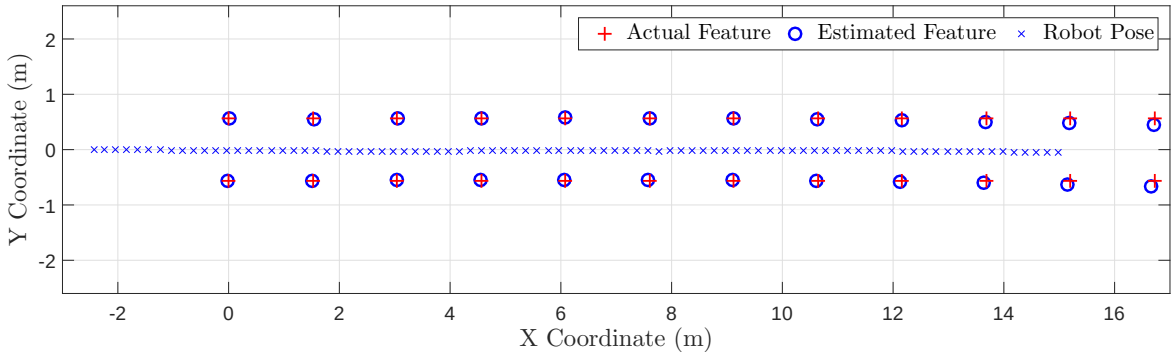

Figure 6.5: Map of pedestrian bridge using EKF-SLAM

Table 6.1: Summary of RMSE for estimated feature locations using EKF-SLAM

Direction	RMSE (m)	
	Overall map	First 20 features
Global X-coordinate	0.024	0.0063
Global Y-coordinate	0.043	0.0081

6.5.2 Mapping results

Figure 6.5 compares the constructed map of the bridge with the actual AR tag locations and includes samples from the estimated DACS trajectory. Overall, the estimated feature states correspond well to the actual tag locations. However, as shown in Figure 6.5, the accuracy of the map tends to degrade towards the end of the bridge. This error is due to the fact the exploration concluded at the 15 m mark and the incremental loop closure scheme has not corrected the final feature estimates. Table 6.1 summarizes the RMSE between the actual map and the estimated feature states in terms of the global X and Y coordinates. The RMSE for the entire map is compared with the RMSE for the first 20 features (i.e., excluding the last two rows of features). The resulting covariance matrix reveals the considerably lower variance in the global X-coordinate of a given feature estimate compared to the global Y-coordinate. This difference can be attributed to measurement error in the sensor and the fact the exploration followed a nearly straight line down the center of the bridge. A consequence of this trajectory and positioning of the AR tags is that most measurements are taken at relatively small angles. As such, small errors in the heading estimate will have a much larger impact on the local y-component compared to the local

x-component. Although there is increased uncertainty associated with the global Y-coordinates of the features, the resulting map is considered sufficient for use in localization.

Chapter 7

Performance evaluation of the prototype DACS

This chapter presents the experimental program used to investigate the overall performance and control effectiveness of the prototype DACS. An overview of the general experimental setup and testing methodology is provided first followed by three separate studies designed to evaluate the formulated LQG, MPC, and H_∞ controllers. Finally, the advantages of mobility when suppressing the vibrations of lightweight structures are assessed on a full-scale pedestrian bridge.

7.1 General experimental setup

Although numerical simulation is a powerful tool to assess a wide range of device characteristics in an efficient manner, physical testing is necessary to accurately capture the true dynamics of the system and properly assess the effects of modelling simplifications. Furthermore, physical testing must be done in full-scale to produce true interaction effects between the structure and device and assess the actual device capacity and mobility. Nevertheless, full-scale experimental testing is cost-prohibitive and fraught with challenges including exciting the structure in a controlled manner, test reproducibility, and space requirements. Therefore, the experimental program for this research leverages real-time hybrid simulation (RTHS) on a hydraulic shake table to achieve full-scale interaction effects without physically testing a full-scale structure.

7.1.1 Methodology

Hybrid simulation is an experimental testing method where the reality of physical testing is combined with the power of numerical simulation techniques. This method of testing allows the test system to be divided into two substructures such that the well understood components are separated from those for which a reliable analytical model is not available. The well understood components are modelled numerically in what is referred to as the analytical substructure while the remaining components make up the experimental substructure which is tested physically in a lab [122]. The experimental substructure often contains load-rate-dependent characteristics, in which case the experiments must be conducted in real-time in order to capture the realistic performance of the system [123–125]. Implementing RTHS requires robust and efficient computational resources as well as a platform for fast and well-synchronized data communication [125]. Nevertheless, by simulating in real-time, the dynamic response of complex systems such as structures controlled by passive, active, or semi-active control devices can be studied without having to physically excite a full-scale structure under laboratory conditions [126, 127]. RTHS is an ideal testing method for the prototype DACS as it enables efficient and accurate assessment of the control performance on full-scale structures under different controller formulations. This method also allows the performance of the device to be evaluated across a range of structures by simply modifying the analytical substructure accordingly.

7.1.2 Mechanical setup

The mechanical aspect of the test setup for RTHS consists of a Shore Western shake table and four shear-type load cells as shown in Figure 7.1. The 1.5 m^2 shake table is driven by a hydraulic fatigue-rated actuator with a stroke length of ±150 mm. A hydraulic service manifold (HSM) rated at 450 L/min regulates the oil pressure at 20 MPa and can generate a maximum force of 67 kN. A built-in linear variable differential transformer (LVDT) and integrated dynamic load cell provide displacement and force feedback respectively from the actuator. An accelerometer mounted on the table is also used to obtain direct acceleration measurements. The four shear-type load cells all have maximum lateral load capacities of 17 kN and are positioned below each UGV tire to measure the interface forces between the UGV and shake table. The load cell measurements are passed through a low-pass digital filter to reduce system noise and prevent high-frequency content from the hydraulic system from entering the numerical simulation. The shake table is

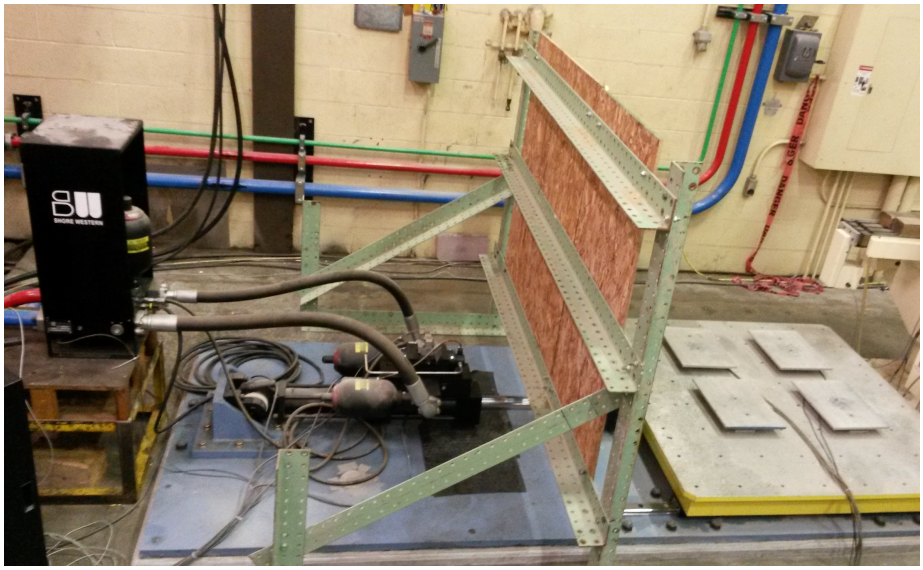

Figure 7.1: Mechanical setup for RTHS

equipped with a Shore Western integrated controller that is capable of applying predefined as well as externally generated (i.e., via analog input) displacement commands. For RTHS, the desired position command is calibrated to a voltage signal and passed to the integrated controller operating in displacement control.

7.1.3 RTHS platform

The key hardware component for the RTHS experimental platform is a NI cRIO-9035 consisting of an embedded real-time controller and an FPGA. The controller features a 1.33 GHz dual-core processor running NI Linux Real-Time, which combines the performance of a real-time operating system with the openness of Linux. An FPGA is an integrated circuit chip consisting of programmable logic blocks, configurable interconnections, and input/output nodes. The programmed logic in an FPGA is compiled into physical hardware facilitating true parallel execution with high reliability [128].

Figure 7.2 presents a schematic of the RTHS architecture which is made up of two nested operational loops. The outer loop, referred to as the real-time loop, is responsible for the real-time simulation of the analytical substructure, determination of the DACS control input, and

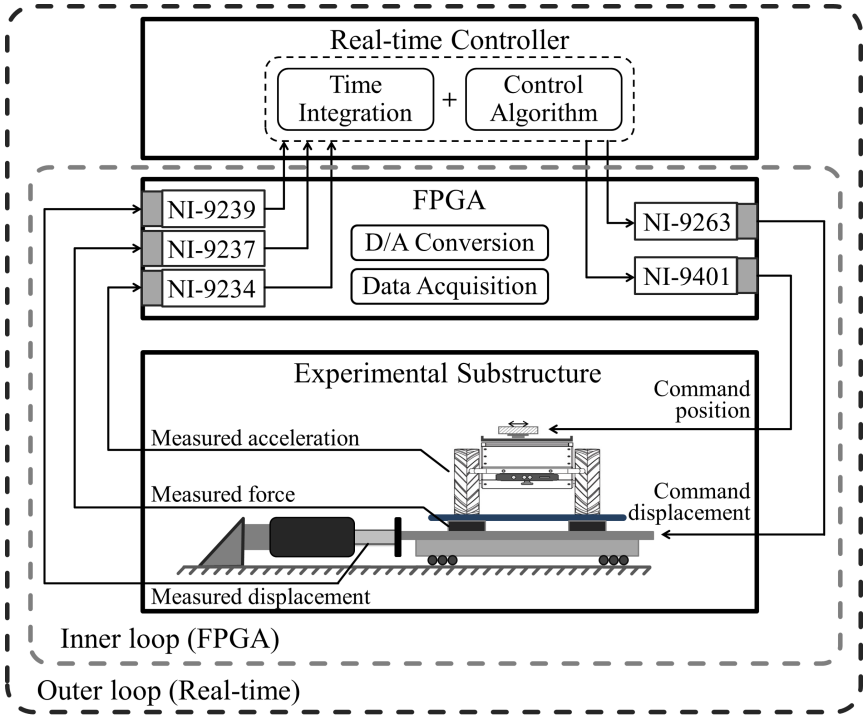

Figure 7.2: Schematic of RTHS platform

any input/output file manipulations being carried out on the real-time controller. The inner loop, running on the FPGA, executes all tasks related to data acquisition from the sensors (i.e., measured restoring force, measured shake table displacement and acceleration, and measured EMD position) and application of any control signals to the experimental substructure (i.e., shake table displacement and EMD position). The NI C-series modules, listed in Table 3.1, facilitate the acquisition and transfer of signals between the FPGA and experimental substructure. As shown in Figure 7.2, the inner loop and outer loop exchange data through direct memory access (DMA). Since the inner loop runs as compiled FPGA code, the execution rate is typically faster than the outer loop running on the real-time controller. Therefore, the DMA link between the two loops executes at the rate of the outer loop. A loop rate of 1 kHz is used in the real-time loop for all simulations unless noted otherwise.

Within a given iteration, simulation of the analytical substructure yields the displacement of the experimental substructure which is issued to the Shore-Western controller and realized on the

shake table. During the same step, the active control algorithm estimates the current states of the system and computes the control input for the DACS. The control input (i.e., position command) is passed to the inner loop where it is converted to a digital quadrature encoder signal and applied to the Gemini servo drive to control the EMD. The restoring force measured at the interface between the UGV tires and shake table is acquired by the load cells and passed to the outer loop to be incorporated in the next iteration of the simulation.

The LabVIEW Real-Time module and LabVIEW FPGA module extend the NI LabVIEW graphical programming environment and are used to program the real-time controller and FPGA respectively. The user interface consists of a host virtual instrument (VI), an FPGA VI, and several sub-VIs coordinated through a LabVIEW program. The term VI is used to refer to an independent LabVIEW program or subroutine. The host VI is designed as a state machine that features initialization and start-up routines and provides a structure for fixed-period iterations. As such, the outer loop tasks are programmed on the host VI which runs on the real-time controller. Given the configurable input/output and parallel execution of the FPGA, the inner loop is programmed in the FPGA VI. This facilitates signal routing between the cRIO and experimental substructure (i.e., shake table, EMD, and sensors)[1]

7.1.4 Real-time hybrid simulator

The most central task within the outer loop is the simulation of the analytical substructure. This involves solving the second-order dynamic equation of motion for the test system. The inputs to the system include the external forces on the analytical substructure and restoring forces measured from the experimental substructure while the outputs of interest are the displacement of the experimental substructure and simulated acceleration measurements for state estimation. Unlike conventional hybrid simulation where the time to complete each step is arbitrary, RTHS is performed in real-time and thus the solution method should not only be robust and accurate but also computationally efficient to maintain synchronization with the control system [129]. A wide range of both implicit and explicit numerical integration methods have been developed for RTHS. Although many implicit methods such as the Hilber-Hughes-Taylor-alpha (HHT-α) method [130] have the benefit of being unconditionally stable, the iterative calculations within each step require significant computational effort which may lead to time delays. On the contrary,

[1]The VIs used for most RTHS studies were developed collaboratively by the author and Mr. Ali Ashasi-Sorkhabi.

explicit methods, such as the central difference method [122], explicit Newmark method [131], or state space formulations [132, 133] are much more efficient computationally; however, typically have a restriction on the step size for numerical stability. In this thesis, the discrete state-space formulation presented in Liu et al. [132] is implemented for simulating the system. This formulation has been validated experimentally using similar hardware and can leverage the previously developed state-space models used for controller design.

Consider the following equation of motion for a general MDOF system:

$$\mathbf{M}\ddot{\boldsymbol{x}}_s(t) + \mathbf{C}\dot{\boldsymbol{x}}_s(t) + \boldsymbol{R}_a(t) + \boldsymbol{E}R_e(t) = \boldsymbol{w}(t) \tag{7.1}$$

where $\mathbf{M}$ and $\mathbf{C}$ are the mass and damping matrices of the analytical substructure respectively, $\boldsymbol{x}_s$ is the vector or nodal displacements and $\boldsymbol{w}$ is the vector of external forces. The terms $\boldsymbol{R}_a$ and R_e denote the restoring force vector computed in the analytical substructure and restoring force measured in the experimental substructure respectively. Note the use of a location vector $\boldsymbol{E}$ to apply the experimental restoring force at the corresponding DOF. In cases where the analytical substructure is assumed to be linear elastic, the analytical restoring force vector is equal to $\mathbf{K}\boldsymbol{x}_s$ where $\mathbf{K}$ is the stiffness matrix of the analytical substructure. On the other hand, the restoring force from the experimental substructure is measured directly by the load cells and treated as an external input to the analytical substructure.

Rewriting the equation of motion in state-space form yields:

$$\dot{\boldsymbol{z}}(t) = \mathbf{A}\boldsymbol{z}(t) + \mathbf{B}\boldsymbol{w}(t) - \mathbf{B}\boldsymbol{E}R_e(t) \tag{7.2a}$$

$$\boldsymbol{y}_s(t) = \mathbf{C}\boldsymbol{z}(t) + \mathbf{D}\boldsymbol{w}(t) - \mathbf{D}\boldsymbol{E}R_e(t) \tag{7.2b}$$

where the state vector $\boldsymbol{z} = [\boldsymbol{x}_s \ \dot{\boldsymbol{x}}_s]^T$ contains the displacements and velocities of the analytical substructure. In RTHS, the outputs of interest are the structural displacements, particularly the displacement at the interface with the experimental substructure. Furthermore, to objectively evaluate the state-estimators used in controller design, the simulated structural accelerations are needed. Therefore, the state, input, and output matrices are given by:

$$\mathbf{A} = \begin{bmatrix} \mathbf{0} & \mathbf{I} \\ -\mathbf{M}^{-1}\mathbf{K} & -\mathbf{M}^{-1}\mathbf{C} \end{bmatrix}, \ \mathbf{B} = \begin{bmatrix} \mathbf{0} \\ \mathbf{M}^{-1} \end{bmatrix}, \ \mathbf{C} = \begin{bmatrix} \mathbf{I} & \mathbf{0} \\ -\mathbf{M}^{-1}\mathbf{K} & -\mathbf{M}^{-1}\mathbf{C} \end{bmatrix}, \ \mathbf{D} = \begin{bmatrix} \mathbf{0} \\ \mathbf{M}^{-1} \end{bmatrix}$$

where $\mathbf{I}$ denotes the identity matrix. For implementation purposes, the continuous-time state-space formulation is discretized using the zero-order-hold discretization method. Denoting the

discrete time step as T and setting $t_0 = kT$, $t = (k+1)T$ yields the following discrete state-space formulation (DSSF) [132]:

$$\boldsymbol{z}\left[(k+1)T\right] = \mathbf{A}_d \boldsymbol{z}\left[kT\right] + \mathbf{B}_d \boldsymbol{w}\left[kT\right] - \mathbf{B}_d \boldsymbol{E} R_e\left[kT\right] \tag{7.3a}$$

$$\boldsymbol{y}_s\left[(k+1)T\right] = \mathbf{C}_d \boldsymbol{z}\left[kT\right] + \mathbf{D}_d \boldsymbol{w}\left[kT\right] - \mathbf{D}_d \boldsymbol{E} R_e\left[kT\right] \tag{7.3b}$$

where $\mathbf{A}_d$, $\mathbf{B}_d$, $\mathbf{C}_d$, and $\mathbf{D}_d$ are the discrete system matrices computed using a discretization time-step of T. A discrete time step of 1 ms is used to coincide with the 1 kHz loop rate of the real-time loop.

7.1.5 Substructuring techniques

Substructuring is the process of decomposing the overall system into two subsystems such that the well understood components are separated from those for which a reliable analytical model is not available. This facilitates accurate assessment of the control performance of the prototype device on full-scale structures by physically testing the prototype on a dynamic shake table (i.e., experimental substructure) and modelling the underlying structure numerically in a computer (i.e., analytical substructure). To account for the interaction effects between the structure and DACS, the dynamic shake table must realize the displacement of the simulated structure at the location of the prototype in real time. In this way, the measured interface force can be applied back to the numerical model at the same location to close the loop. Having the prototype separated from the numerical model facilitates efficient investigations into various controller formulations and control performance on different structures.

Previous studies employing RTHS to evaluate structural control systems simulate numerical substructures in the physical domain and thus are limited to spatially fixed loads [126, 134]. In other words, both the external loads applied to the structure and the experimental restoring forces are confined to locations corresponding to modelled DOFs. While suitable for evaluating rigidly connected control devices, the existing substructuring frameworks are unable to asses the mobility aspect introduced through the concept of DACSs which allows to device position itself at any location on the structure. To overcome this limitation, as well as address the case of spatially varying external loads (i.e., moving pedestrians loads), Ashasi-Sorkhabi et al. [135] developed a numerical substructuring approach based on modal decomposition principles. The premise of this formulation is that by decomposing the structure into separate vibrational modes, the influence of

spatially varying forces can be computed using the corresponding mode shapes. In this approach, RTHS is carried out for each mode separately and superposition techniques are used to recreate the physical response. Although based in the modal domain, the same DSSF approach presented above (see Equations 7.3a and 7.3b) is used by expressing each mode as a individual state space model. Thus, the only difference is the discrete system matrices $\mathbf{A}_{d,i}$, $\mathbf{B}_{d,i}$, $\mathbf{C}_{d,i}$, and $\mathbf{D}_{d,i}$ are defined in the modal domain for each mode i considered in the simulation. Further details on this numerical substructure modelling approach in the modal domain are provided in Appendix B.

It should be noted that in typical RTHS applications, the experimental substructure consists of a passive system [134, 136, 137]. Thus, the generated interface forces are a direct result of the physical displacement and cannot be controlled externally. However, in the case of an active control system such as the prototype device, the desired interface force is determined according to a predefined control algorithm. As such, comparing the desired interface force to the actual measured force is indicative of the modelling accuracy (i.e., DACS models and interaction effects) and overall control system performance.

7.2 LQG control performance

The performance of the LQG control formulation for the prototype DACS is experimentally evaluated through RTHS. The purpose of this study is two-fold: the first goal is to validate the LQG control formulation for the prototype DACS using the ICM approach while the second goal is to comparatively assess the overall control performance relative to alternative devices. To fulfill the latter, an equivalent TMD device is designed to establish a baseline for comparison. In this case, the term equivalent implies that the TMD is designed with a mass equal to the moving mass of the prototype DACS. The control performance of each device is assessed on an SDOF system. A description of the SDOF system and TMD design is provided next followed by the testing procedure and discussion of results.

7.2.1 System description

Consider an SDOF system with mass, damping, and stiffness of 2000 kg, 300 Ns/m and 120 kN/m respectively, yielding a natural frequency of 1.2 Hz and a damping ratio of 1.0 %. The linear

system is assumed to be time-independent and excited by harmonic excitation coinciding with the natural frequency to cause resonance. The properties of the SDOF system are selected such that the system is representative of the first lateral mode of an arbitrary lightweight footbridge. For comparison, two different modular aluminum footbridges spanning 12.2 m and 22.9 m were reported to have masses of 982 kg and 1735 kg respectively. Experimental testing of these footbridges identified fundamental lateral frequencies of 2.3 Hz and 1.0 Hz respectively and damping ratios of 1.0 % and 0.8 % respectively [92].

The LQG formulation presented earlier is adopted to implement an LQG controller. The weighting matrices $\mathbf{W}_z$ and $\mathbf{W}_u$ are tuned *a priori* based on trial and error simulations to ensure the desired control forces are within the capacity of the EMD. The ICM approach is used such that the LQG controller outputs the desired EMD inertial force and the corresponding position command is determined using the inverse EMD model. It is worth noting that the LQG controller design can be improved by taking into account the narrow-band excitation. This is accomplished by incorporating a band-pass filter into the structure model in the same way in which Kanai–Tajimi filters are used to account for the frequency content of seismic excitation [38]. However, in practical applications the frequency content of the excitation is generally unknown *a priori*, which supports the Gaussian white noise assumption used in the LQG controller formulation. The equivalent TMD device used for performance comparison is designed with a 2 % mass ratio such that the TMD mass is approximately equal to the auxiliary mass of the EMD. Following the standard design procedure for passive damping devices in Connor [1], the resulting TMD mass, damping, and stiffness properties are 40 kg, 53 Ns/m and 2.27 kN/m respectively.

7.2.2 Test procedure

The performance of the prototype device is evaluated using the previously described RTHS methodology. This involves isolating the prototype DACS as the experimental substructure and positioning it atop four shear-type load cells on the Shore Western shake table. The SDOF system is modelled numerically as the analytical substructure in LabVIEW and deployed on the cRIO. Figure 7.3 shows the RTHS substructuring and experimental setup. Since the ICM approach is used, the analytical UGV model is incorporated with the SDOF system to form the controlled plant. The LQG controller in this approach outputs the desired EMD inertial force and the inverse EMD model is utilized to compute the desired EMD position command. The augmented plant

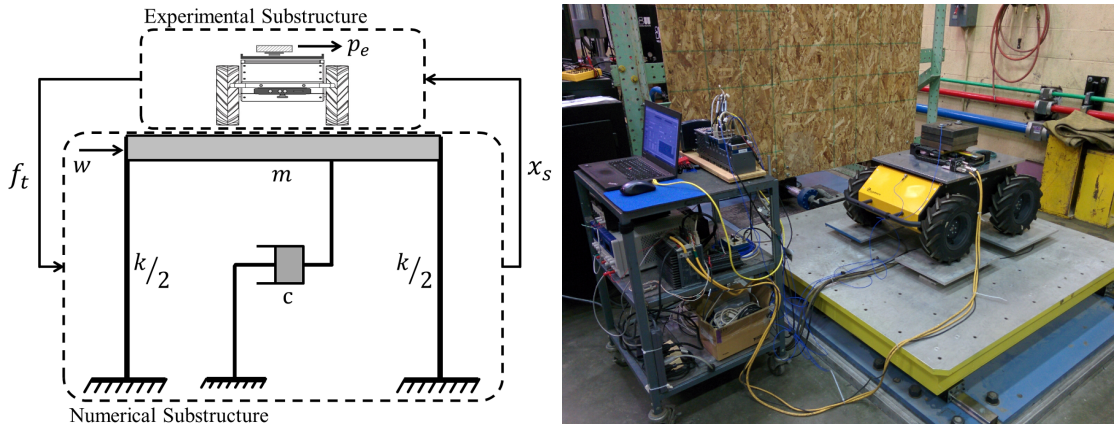

(a) Substructuring approach

(b) Experimental substructure

Figure 7.3: RTHS substructuring and experimental setup for evaluation of LQG controller

is also used to build a Kalman filter for state estimation. In the RTHS setup, the Kalman filter uses simulated acceleration measurements to estimate the states of the augmented plant needed for state feedback control. The control effectiveness of the prototype DACS is compared against the uncontrolled case and performance of the equivalent TMD device. Both the uncontrolled response and response under passive control are determined through numerical simulation in MATLAB using the same harmonic excitation.

7.2.3 Results

Figure 7.4 compares the uncontrolled displacement response with the controlled responses using the passive TMD and prototype DACS. As shown, the prototype DACS outperformes the equivalent TMD system, reducing the TMD steady-state response by approximately 45 %. To achieve the same level of performance as the prototype DACS for the given structure, the TMD mass would need to be increased to a 10 % mass ratio or 200 kg. Passive devices of this size are not practical for lightweight structures. The control effectiveness of the prototype DACS largely depends on the LQG controller design which balances the trade-off between control performance and robust stability. In this study, the controller design is relatively conservative and only generates control forces of approximately ± 100 N as shown in Figure 7.5. Reducing the weighting matrix $\mathbf{W}_u$ will increase the control effort and further reduce the response. This result confirms

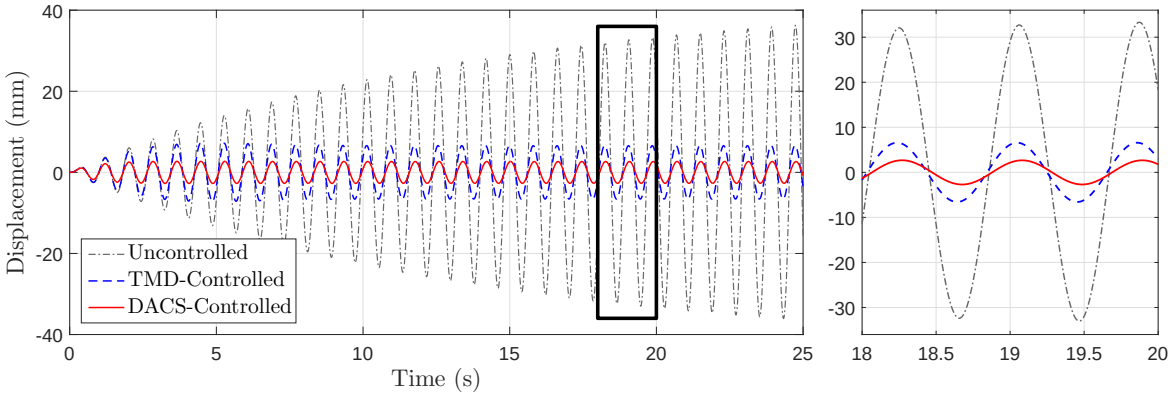

Figure 7.4: Uncontrolled and controlled displacement responses of the SDOF system

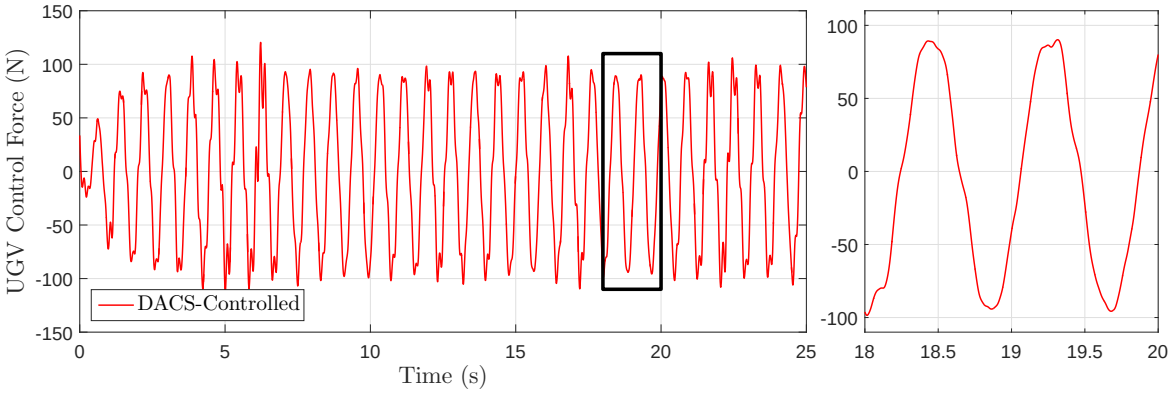

Figure 7.5: Measured control force from prototype DACS with LQG control

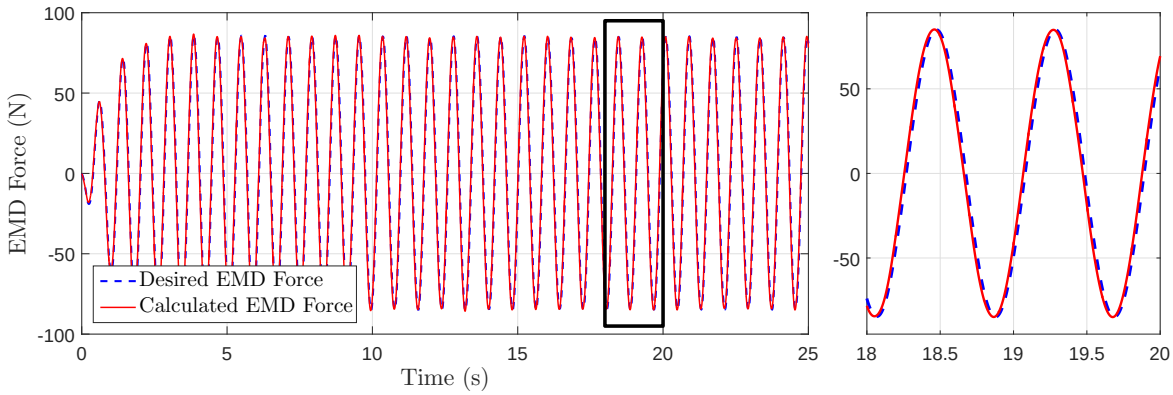

Figure 7.6: Desired and measured EMD control force with LQG control

that the prototype device deployed for a short-term application has ample capacity to outperform a passive TMD of similar mass. Furthermore, the prototype device can effectively suppress low-frequency vibrations on structures with masses of approximately 2000 kg. For larger structures, the prototype can be modified or multiple units can be deployed in order to achieve similar levels of performance.

To illustrate the accuracy of the system modelling and controller formulation, Figure 7.6 compares the desired EMD control force with the actual EMD inertial force computed from the measured relative acceleration. The strong correlation verifies the accuracy of the EMD model for computing the position commands and further validates the disturbance rejection properties of the position feedback controller. In turn, the CSI modelling approach based on the disturbance rejection assumption is confirmed. However, the accuracy of the UGV model and associated effects of model uncertainty may still influence the overall performance.

7.3 MPC performance

Both numerical simulations and experimental studies are conducted to investigate the performance of the MPC formulation for the prototype device. The main objectives of the numerical simulations are to compare the overall performance of the MPC scheme with LQG control methods and demonstrate the ability of the adaptive cost function (i.e., online tuning) to maximize utilization of the device. Although numerical simulations have the advantage of efficiently com-

paring a number of different controller designs, there is no guarantee these control algorithms can be implemented in real-time. Thus, an experimental study is designed to demonstrate the ability of the formulated MPC algorithm to execute in real-time. To this end, RTHS is used to examine the control performance of the prototype device on a full-scale aluminum pedestrian bridge. If the MPC algorithm can execute in real-time on the cRIO while simultaneously simulating the numerical substructure, it can be guaranteed to run in real-time under practical applications, where the additional burden of numerical sub-structure computations are not present. The systems used in the numerical and experimental studies are described next followed by the testing procedure and discussion of results.

7.3.1 System description

Numerical study:

For the numerical simulations, an SDOF system is used as the structure to be controlled (i.e., representative of a single mode of vibration). The SDOF system is designed with mass, damping, and stiffness properties of 2000 kg, 345 Nm/s, and 150 kN/m respectively, yielding a natural frequency of 1.4 Hz and a 1 % damping ratio. A model predictive controller is designed for the combined SDOF structure and prototype control system according to the ISM approach, with the interaction effects modelled using acceleration feedback. The MPC objective function is designed to penalize non-zero displacement and velocity of the structure as well as the magnitude of the control input. The EMD stroke and peak tire force constraints described in Equations 5.26 and 5.27 are applied as bounds to the optimization problem.

Many factors influence MPC effectiveness including the penalty weighting matrices, the prediction horizon, and the number of prediction points. The weighting matrices penalizing the states are set to $\mathbf{W}_z = \mathbf{W}_\infty = 1.0 \times 10^6 \times \mathbf{I}_2$ for all cases, while the weighting matrix penalizing control effort $\mathbf{W}_u$ varies depending on the desired level of control authority or is tuned online using the proposed utilization algorithm. The prediction horizon and the number of prediction points are tuned to balance the trade-off between performance and computational demand. Longer prediction horizons with more prediction points yield improved control performance at the cost of increased computational time. Constrained by the condition that the controller must run in real-time, a prediction horizon of $h_p = 0.8$ s with 40 prediction points is used. It should be noted that this length of prediction horizon is possible due to the relatively small model size and may not be

realizable with larger systems. To study the effects of incorporating operating constraints directly in the control formulation, the MPC controller is compared against a traditional LQG controller. The objective function for the LQG controller takes the same form as the MPC objective function with the only difference being the minimization in LQG is performed over an infinite horizon and as such the terminal weighting matrix isn't used. To conduct a valid comparison free from tuning bias, both controllers are designed with the same weighting matrices $\mathbf{W}_z$ and $\mathbf{W}_u$.

Experimental study:

The experimental test structure is a full-scale modular aluminum pedestrian bridge spanning 16.76 m. The lightweight bridge has a width of 1.22 m and is constructed in 1.52 m modules. Figure 3.2b shows the physical bridge which was previously used to demonstrate map building through EKF-SLAM. A numerical model of the pedestrian bridge makes up the analytical substructure. The bridge is modelled as a simply-supported, linear Bernoulli beam with a length of 16.76 m, mass of 1800 kg, and elastic modulus and moment of inertia of 69 GPa and 50 $\times 10^6$ mm^4 respectively. Damping ratios of 1 % and 2 % are approximated for the first two modes. The continuous beam model is discretized into four beam elements resulting in 10 translational and rotational DOF at the 5 nodes. To reduce the model order for more efficient controller formulation, the system equivalent reduction expansion procedure (SEREP) is employed to condense the model to three translational DOFs [138]. SEREP preserves the natural frequencies of the full model through the condensation which are computed as 1.0 Hz, 4.0 Hz, and 9.2 Hz for the first three modes respectively. The mass, damping, and stiffness matrices for the numerical bridge model denoted $\mathbf{M}$, $\mathbf{C}$, and $\mathbf{K}$ are given by:

$$\mathbf{M} = \begin{bmatrix} 437.7 & 12.0 & -5.2 \\ 12.0 & 432.6 & 12.0 \\ -5.2 & 12.0 & 437.7 \end{bmatrix} \text{[kg]}, \quad \mathbf{C} = \begin{bmatrix} 755.5 & -711.8 & 307.8 \\ -711.8 & 1063.3 & -711.8 \\ 307.8 & -711.8 & 755.5 \end{bmatrix} \text{[Nm/s]}, \quad \mathbf{K} = \begin{bmatrix} 4.91 & -4.82 & 2.07 \\ -4.82 & 7.00 & -4.82 \\ 2.09 & -4.82 & 4.91 \end{bmatrix} \times 10^5 \text{ [N/m]} \tag{7.4}$$

With the structure modelled numerically, the prototype control system is isolated as the experimental substructure. The prototype is tested physically on the dynamic shake table such that the simulated bridge displacements are realized beneath the UGV tires. Since the shake

table reproduces the structural response at the location of the control system in real-time, the true interaction effects are physically realized. The prototype DACS is assumed to be positioned at mid-span coinciding with the second DOF. In this case, the MPC objective function is designed to minimize the displacement and velocity at each DOF while balancing the trade-off with control effort. For experimental validation, the objective function weighting matrices are set to constant values of $\mathbf{W}_z = \mathbf{W}_\infty = 1.0 \times 10^6 \times \mathbf{I}_6$ and $\mathbf{W}_u = 1.0$. The EMD stroke and UGV tire force constraints are included in the formulation to bound the minimization which uses 40 prediction points over a 0.8 second horizon. It should be noted however that in experimental testing, the EMD stroke constraint is reduced to ±65 mm for safety purposes.

7.3.2 Test procedure

Numerical study:

All numerical simulations are implemented in the MATLAB R2015b computing environment and simulated using a time step of 1 ms. The SDOF system is excited using a constant amplitude chirp signal that forces the system to pass through resonance. The 60-second chirp signal has an amplitude of 275 N with frequencies increasing linearly from 1 Hz to 1.4 Hz over 30 seconds and decreasing to 1 Hz at the end of the signal. Five different controllers are implemented to assess the performance of the MPC and LQG algorithms under varying levels of control authority. Table 7.1 summarizes the controller properties and penalty weights of the controllers. The low authority controllers have been tuned such that the physical operating constraints are not violated with LQG control under the specified harmonic excitation. The high authority controllers employ a reduced control penalty in order to maximize performance. However, the increased control effort will lead to constraint violations if not properly accounted for.

Experimental study:

In addition to numerical simulations, a number of RTHS experiments are conducted to verify the control performance of the prototype device under the proposed MPC algorithm and demonstrate physical implementation of MPC for full-scale structural control applications. The MDOF bridge model is subjected to band-limited Gaussian excitation at each DOF and controlled by the DACS prototype positioned at mid-span. The numerical bridge is simulated under three different control scenarios: uncontrolled, theoretical, and experimental. The uncontrolled scenario involves straight simulation of the structure (i.e., $R_e = 0$) in order to determine a baseline for comparison.

Table 7.1: Properties of MPC and LQG controllers

Controller Name	Design Method	Penalty on States $\mathbf{W}_z$	Penalty on Control $\mathbf{W}_u$
MPC-1	Low Authority MPC	$1 \times 10^6 \times \mathbf{I}_2$	10
LQG-1	Low Authority LQG	$1 \times 10^6 \times \mathbf{I}_2$	10
MPC-2	High Authority MPC	$1 \times 10^6 \times \mathbf{I}_2$	1
LQG-2	High Authority LQG	$1 \times 10^6 \times \mathbf{I}_2$	1
aMPC	Adaptive MPC	$1 \times 10^6 \times \mathbf{I}_2$	*varies*

The theoretical control scenario is used to study the accuracy of the DACS models and verify the approach used to account for CSI. In the theoretical control scenario, the experimental restoring force is simulated using the analytical models of the EMD and UGV. The third control scenario, referred to as experimental, involves the full RTHS setup as described where the experimental restoring force is measured from the load cells.

Running in series with the hybrid simulator is the MPC formulation to determine the optimal position command for the EMD. In order to run in real-time, the C++ code generated using the ACADO toolkit is compiled into a shared library object which includes a wrapper function to be called at each time step. The wrapper function returns the optimal position command given the current state estimate and assigned values for any parameterized constraints or penalty weights. The shared library object is deployed on the cRIO and embedded in the real-time LabVIEW VI. Figure 7.7 depicts a schematic of the RTHS implementation and interface between the analytical and experimental substructures.

7.3.3 Results

Numerical study:

Figure 7.8a compares the uncontrolled displacement response of the SDOF structure with the controlled responses from the low authority MPC and LQG controllers as well as the adaptive model predictive control (aMPC) controller. The MPC-1 and LQG-1 controllers show comparable results with only slight improvement in performance from LQG-1 due to the restrictions on the

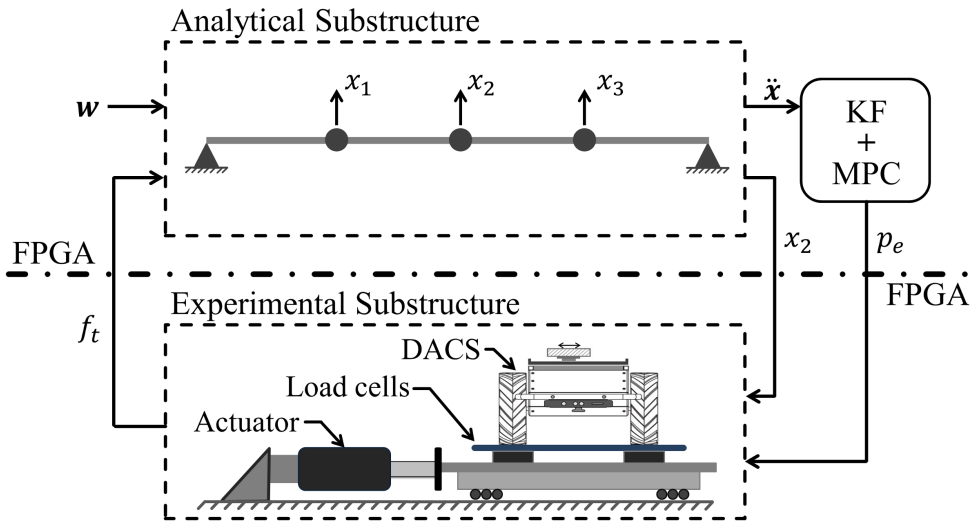

Figure 7.7: Schematic of RTHS implementation for full-scale pedestrian bridge

prediction horizon in MPC-1. Since the controllers have been tuned to avoid the EMD stroke and tire force constraints, the optimal EMD commands computed from LQG-1 and MPC-1 are consistent and achieve a peak reduction of approximately 28 % in the displacement response. This result verifies that real-time MPC formulations can achieve similar performance to LQG controllers in the absence of constraints. The adaptive MPC controller is initialized with the same penalty of $\mathbf{W}_u = 10$ on control effort. The algorithm detects low utilization at the beginning of the simulation with position commands confined to ±7 mm and gradually decreases the penalty weight on the control effort to increase the forces. The effect of decreasing the penalty is shown in Figure 7.8b which compares the EMD position commands for each controller. As shown, the aMPC controller generates much larger position commands relative to the LQG-1 and MPC-1 controllers thereby achieving a peak reduction of 46 % in the displacement response while still operating within the physical limitations. This result highlights the ability of an MPC controller to adapt in real-time to improve performance.

The performance of the high-authority LQG and MPC controllers are compared to the uncontrolled response in Figure 7.9a. The high authority LQG-2 controller appears to have superior performance relative to the corresponding MPC-2 controller; however, the LQG-2 controller has violated the EMD stroke constraint with position commands as large as 85 mm and therefore this level of performance is not physically possible with the prototype DACS. The importance

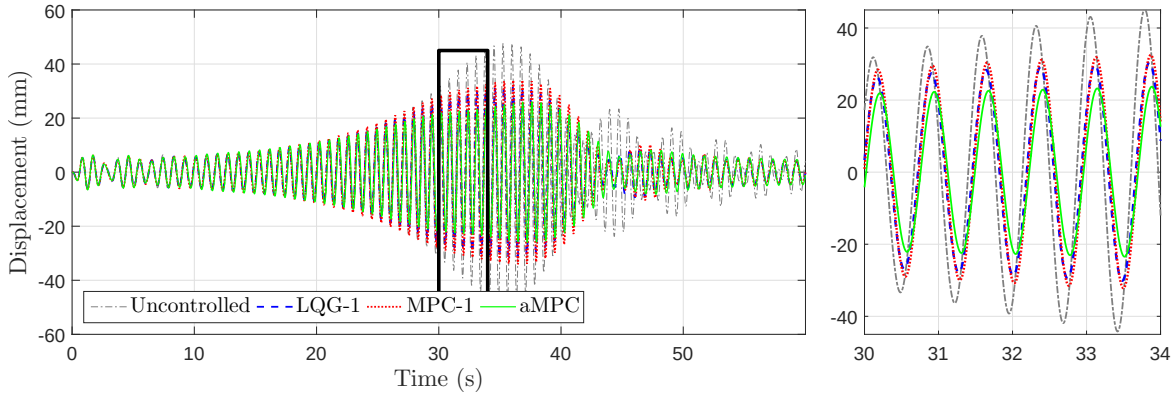

(a) Displacement response of SDOF system

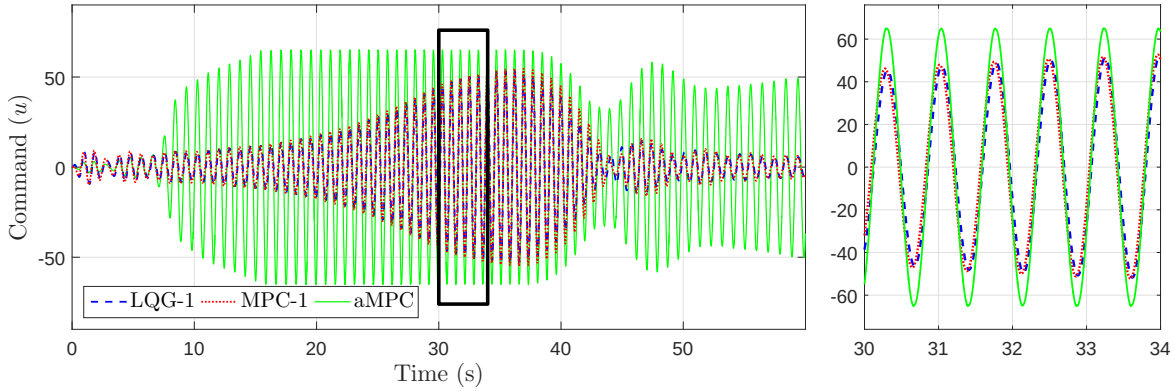

(b) EMD position commands

Figure 7.8: Comparison of low-authority LQG and MPC controllers

of constraint modelling for the prototype system is evident when comparing the optimal EMD position commands which are plotted in Figure 7.9b. The formalized method for addressing physical operating constraints allows the MPC-2 controller to yield similar position commands to the LQG-2 controller up to the prescribed threshold of ±65 mm. Beyond this point, the MPC-2 controller saturates the position command to avoid end-of-stroke collisions. Despite violating the EMD stroke constraint, neither controller generates tire forces in excess of 400 N. However, in the event the forces exceeded 300 N, the soft-constraint in the MPC-2 controller would be triggered to prevent tire slippage. Similar to the low-authority case, the aMPC controller detected under-utilization at the onset of the simulation and further decreased the control penalty. However, as the structural displacements increased, the EMD entered the high-utilization zone which led to an increase in the control penalty to avoid saturation. Although saturating the position command prevents collisions with the end-of-stroke limits, the sudden change in velocity can cause large instantaneous changes in acceleration which generate impulse-like forces. The effect of saturation is shown in Figure 7.9c where the estimated tire force under MPC-2 control sees large spikes coinciding with the saturation of the position command. In physical systems, these forces can cause slipping in the UGV tires and lead to undesirable control performance. The utilization-based algorithm for adaptive MPC is shown to avoid saturation by appropriately tuning the penalty on control input. The overall performance of the aMPC controller is slightly reduced relative to the MPC-2 controller however the negative effects of saturation are avoided.

Experimental study:

The RTHS experiments were successfully completed in real-time without computational delays. Figure 7.10 compares the displacement responses of the first and second nodes (i.e., quarter-span and mid-span) under the three different control scenarios. Both the theoretical scenario and experimental scenario demonstrate effective control performance by reducing the uncontrolled displacements by approximately 56 % and 62 % respectively at all DOFs in terms of the RMS value of the response. This validates the MPC controller design and successfully demonstrates real-time implementation. The experimental scenario yields slightly smaller displacements relative to the theoretical scenario suggesting the physical system generates slightly larger forces than estimated. This can be attributed to uncertainty in the prototype models or the accuracy of the shake-table in realizing the simulated displacements. Nevertheless, the consistently similar responses between the theoretical and experimental scenarios not only validates the modelling of the prototype components but also verifies the assumptions regarding the interaction effects.

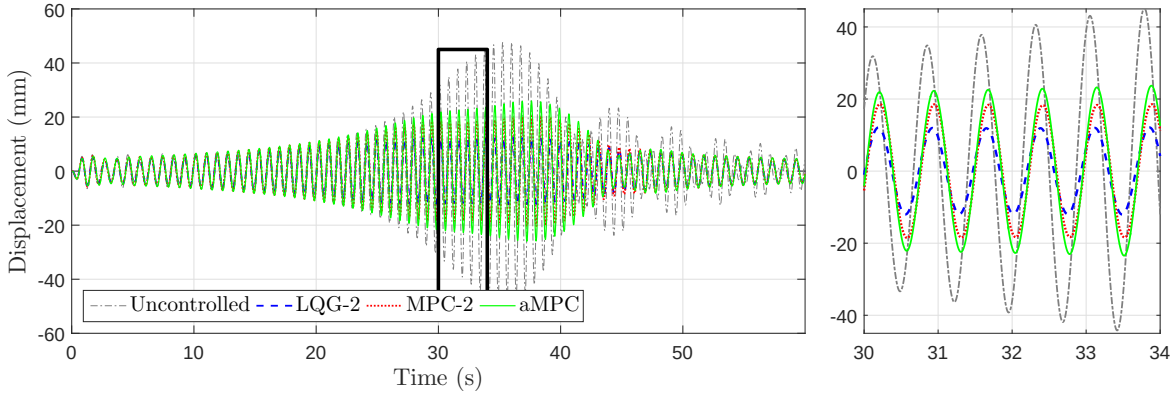

(a) Displacement response of SDOF system

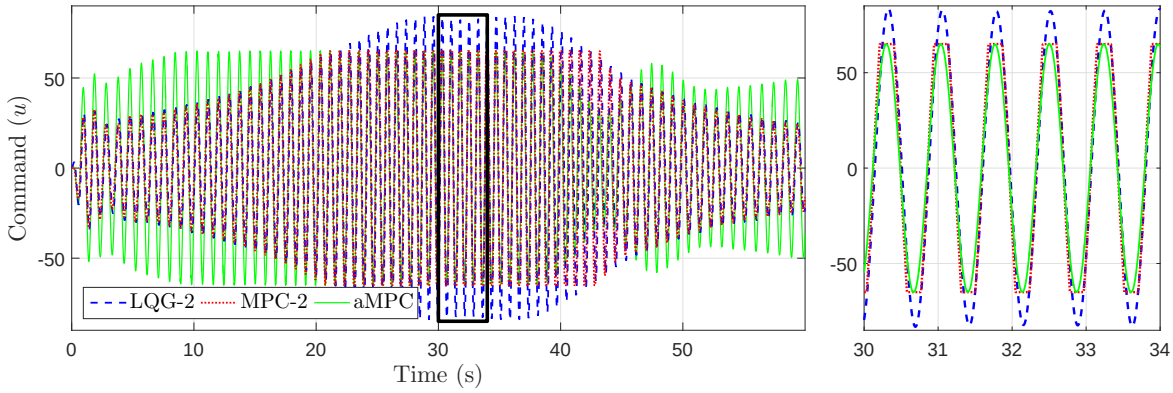

(b) EMD position commands

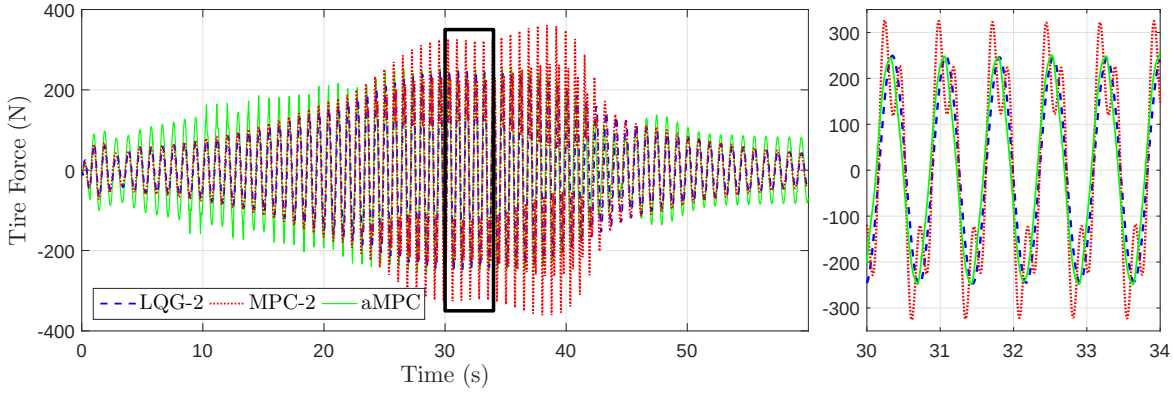

(c) Estimated UGV tire forces

Figure 7.9: Comparison of high-authority LQG and MPC controllers

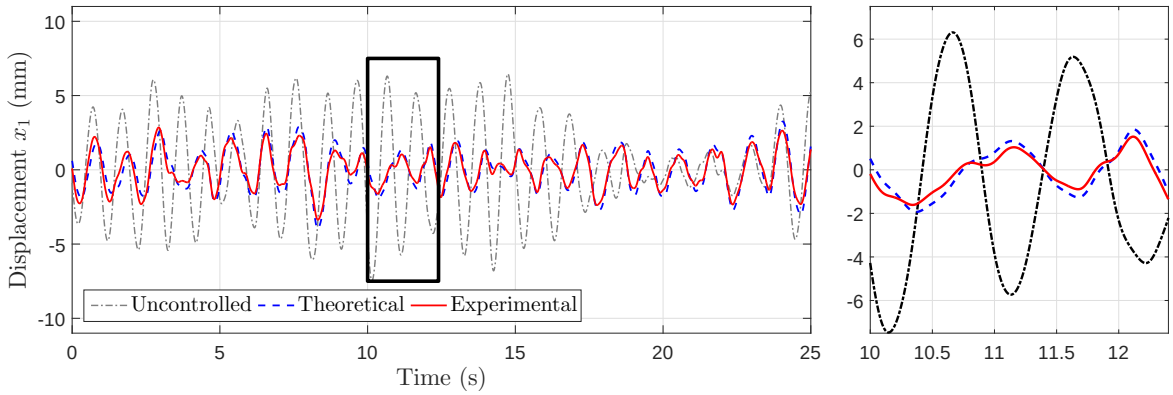

(a) Displacement responses at node 1 (quarter-span)

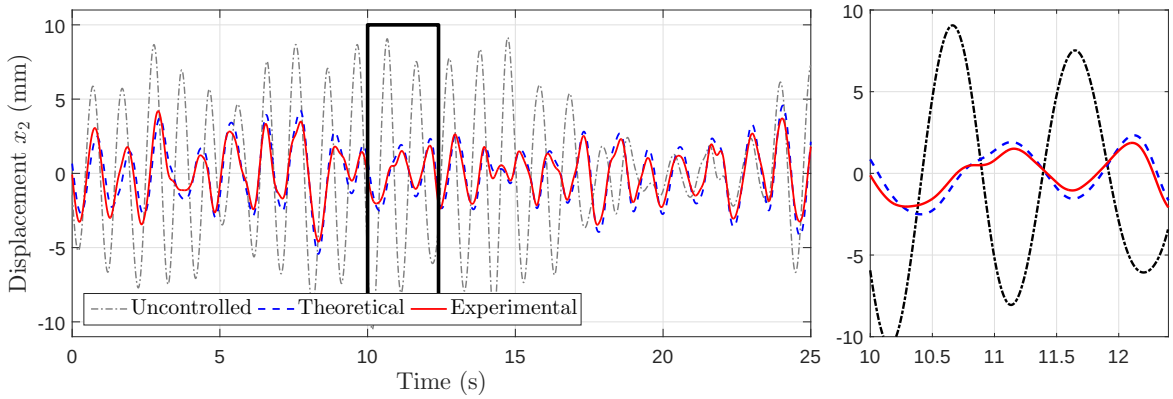

(b) Displacement responses at node 2 (mid-span)

Figure 7.10: RTHS displacement responses with MPC controller

It should be noted that physical control delays could also contribute to differences in the theoretical and experimental responses. Control delays could arise in the actuation of the shake table or tracking of the EMD position. To study these delays, Figure 7.11 compares the commanded and measured table displacements as well as commanded and measured EMD positions. A total delay of 16 ms is computed for the tracking of the shake table which is measured using the built-in LVDT and acquired through the FPGA. Similarly a delay of 17 ms is computed for the position tracking of the EMD which is consistent with previous studies on the prototype. These delays are expected to have negligible impact on the experimental results. The error in tracking of both signals over the first 5 seconds is attributed to a ramp function that scales all commanded output signals to avoid sharp initial motion.

7.4 H_∞ control performance

The performance of the robust H_∞ control formulation for the prototype DACS is evaluated through numerical simulations. The overarching objective of the study is to demonstrate the importance of addressing model uncertainty directly in the controller formulation. This is achieved by comparing the performance of a robust H_∞ controller with that of an H_∞ controller designed based on nominal system models. Robust performance is also studied in the context of uncertain structure models where the stiffness and damping parameters of a MDOF structure model are not known precisely but rather defined by a range of possible values. A description of the controlled system used in this study is provided next followed by the H_∞ controller design procedure and discussion of results.

7.4.1 System description

The structure model considered in the numerical simulations consists of a three-DOF simply-supported beam model. Figure 7.12 displays a schematic of the structure model which is defined by mass, damping, and stiffness parameters denoted m_s, c_s, and k_s respectively. The mass parameter is assumed to be known and equal to 750 kg however the damping and stiffness parameters are uncertain and estimated as 50 Ns/m and 75 kN/m respectively. The uncertainty associated with the damping and stiffness parameters is defined by ±20 % and ±10 % respectively. Table 7.2 summarizes the nominal values and uncertainty associated with the physical parameters.

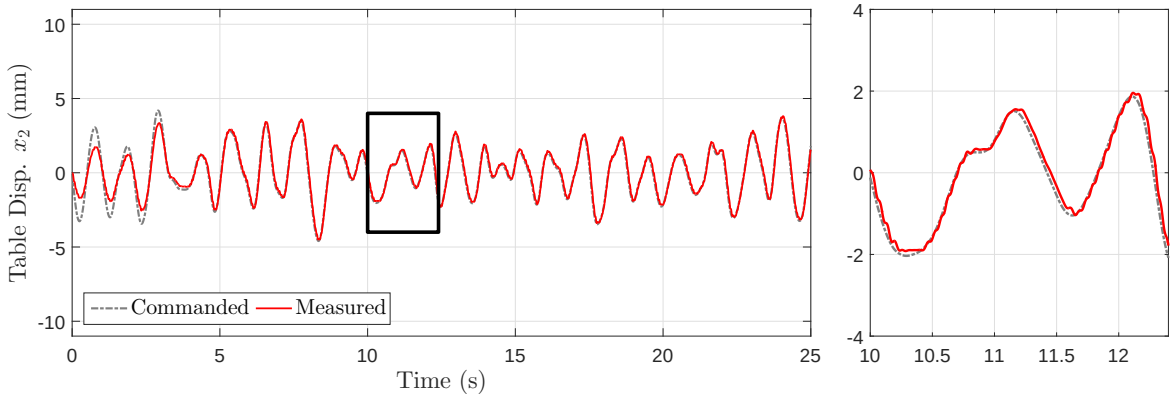

(a) Shake-table displacement tracking during RTHS

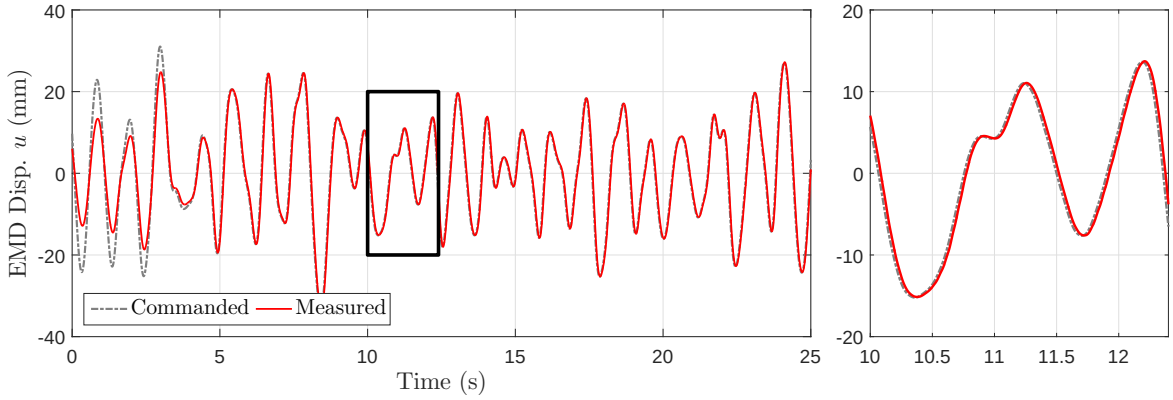

(b) EMD position tracking during RTHS

Figure 7.11: EMD and shake-table tracking during RTHS with MPC controller

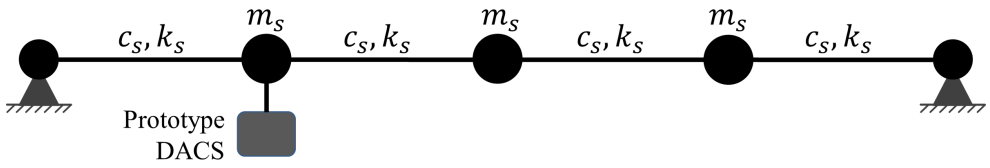

Figure 7.12: MDOF structure model with uncertain parameters

Table 7.2: Properties of uncertain MDOF structure model

Property	Parameter	Nominal value	Uncertainty
Mass	m_s	750 kg	-
Damping	c_s	50 Ns/m	±20% (±10 Ns/m)
Stiffness	k_s	75 kN/m	±10% (±7.5 kN/m)

The prototype DACS is deployed on the structure at quarter-span which corresponds to the first DOF. The uncertain UGV and EMD system models, shown in Figure 5.14 and Figure 5.15 respectively, are used to address the uncertainty in the prototype device directly in the H_∞ controller formulation.

7.4.2 Controller design

H_∞ controller design requires modelling the closed-loop system as a generalized plant with weighting sensitivities on the regulated output and exogenous input. The regulated output contains the structural state vector (i.e., nodal displacements and velocities) weighted by the sensitivity function $S_{\mathbf{y}_s}$ and control input vector weighted by the sensitivity function S_{p_c}. The output weighting sensitivity $S_{\mathbf{y}_s}$ is designed using a second-order low-pass filter with a frequency cut-off of 5 Hz and static gain parameter $\rho_{\mathbf{y}_s}$. Thus, all modes below 5 Hz – coinciding with the control bandwidth of the DACS prototype – will be considered in the optimization. Furthermore, a high-pass filter with a cut-off frequency of 4 Hz and static gain of ρ_{p_c}, is applied to the control input such that frequencies outside the EMD control bandwidth will be penalized heavily in the optimization. Balancing the trade-off between control performance and actuator effort is achieved through tuning the gain parameters $\rho_{\mathbf{y}_s}$ and ρ_{p_c}. Trial-and-error tuning is performed based on the described structure model and expected disturbance to ensure the DACS prototype operates within the physical constraints (i.e., EMD stroke limitations and maximum UGV tire forces). On the other hand, the exogenous input contains the external excitation applied at each DOF and disturbances (i.e., measurement noise) affecting the structure's output vector. The external excitation and measurement noise are weighted by the sensitivity functions S_ω and S_ν respectively. For this study, the external forces applied to the structure are assumed to be band-limited Gaussian excitation encompassing all three structural modes of vibration. As such, the

Table 7.3: Weighting sensitivity functions in H_∞ generalized plant model

Sensitivity Function		Filter Model	Cut-off Frequency	Gain Parameter
Input Sensitivity	S_ω	1^{st}-order low-pass	10 Hz	$\rho_\omega = 1$
Noise Sensitivity	S_ν	static gain	-	$\rho_\nu = 0.0005$
Control Sensitivity	S_{p_c}	1^{st}-order high-pass	4 Hz	$\rho_{p_c} = 1$
Output Sensitivity	S_{y_s}	2^{nd}-order low-pass	5 Hz	$\rho_{y_s} = 150$

input sensitivity function S_ω is modelled as a low-pass filter with a cut-off of 10 Hz and gain of ρ_ω. The sensitivity function weighting the measurement noise is simply modelled as a static gain denoted by ρ_ν to represent the assumption of additive white-noise affecting the measurements. Table 7.3 summarizes the details for each weighting sensitivity function in the generalized plant model.

Three different H_∞ controllers are synthesized from the same generalized plant model containing the prescribed weighting sensitivities functions. The first controller, denoted K_{nn} is designed without any consideration for uncertainty, that is, the controller is synthesized based on the nominal structure model, and nominal DACS model. The second controller, denoted K_{nr}, considers the uncertainty associated with the DACS model however assumes the structure model is known. Finally, the third controller, denoted K_{rr} is designed to be robust to both structure uncertainty and DACS uncertainty and therefore is synthesized based on the uncertain structure model, uncertain UGV model, and uncertain EMD model. Table 7.4 summarizes the three H_∞ controllers considered in this study. Each controller is synthesized using the Robust Control Toolbox in MATLAB R2015b. The generalized plant model for the first controller does not contain any uncertainty and as such is optimized directly using the standard two-Riccati equation method defined in Doyle et al. [111]. On the other hand, the controllers K_{nr} and K_{rr} are designed using μ-synthesis such that the singular value of the uncertain plant model, denoted by μ, is minimized. An automated D-K iteration procedure that provides an approximation to μ-synthesis is used to synthesize K_{nr} and K_{rr}. A brief overview of the D-K iteration procedure is provided in Appendix C and further details on μ-synthesis and the D-K iteration procedure can be found in the literature [139–142].

Table 7.4: Summary of H_∞ controllers and design methods

Controller Model	Structure Model	DACS Model	Design Method
K_{nn}	nominal	nominal	Riccati Equations
K_{nr}	nominal	uncertain	D-K synthesis
K_{rr}	uncertain	uncertain	D-K synthesis

7.4.3 Results

The performance of the various H_∞ controllers are studied through a series of numerical simulations. In each case, the structure model is excited by band-limited (i.e., 0 to 10 Hz) Gaussian excitation at each DOF and the prototype DACS is implemented at the first DOF. The aim of the first simulation is to establish a baseline for control performance by ignoring uncertainty and thus simulating the nominal structure model with the prototype device characterized by the nominal DACS model. Figure 7.13 compares the uncontrolled displacement response at each DOF against the controlled responses obtained using the nominal controller K_{nn} and robust controller K_{nr}. As expected, the controller K_{nn} designed based on the nominal structure and nominal DACS model (i.e., equal to the simulated system) outperforms the robust controller K_{nr} which is designed for the entire range of uncertain DACS models. Nevertheless, both controllers perform well; K_{nn} reduces the RMS of the response by over 75 % while K_{nr} achieves at least 70 % suppression in the RMS value. In both cases the prototype DACS operates within the physical limitations although the nominal controller output slightly larger control forces.

The importance of addressing the uncertainty associated with the DACS prototype is demonstrated through the second simulation which investigates the performance of the same two H_∞ controllers (i.e., K_{nn} and K_{nr}) for the case when the true dynamics of the prototype DACS are unknown. To simulate the effects of uncertain DACS dynamics, 20 realizations of the uncertain UGV and EMD models are extracted and simulated with the same nominal structure model. The displacement responses controlled by the robust K_{nr} controller are plotted for each DOF in Figure 7.14. For comparison, the controlled response based on the nominal DACS model and uncontrolled displacement response are also plotted for each DOF. Although the nominal K_{nn} controller achieves effective performance for realizations of the DACS model with small amounts

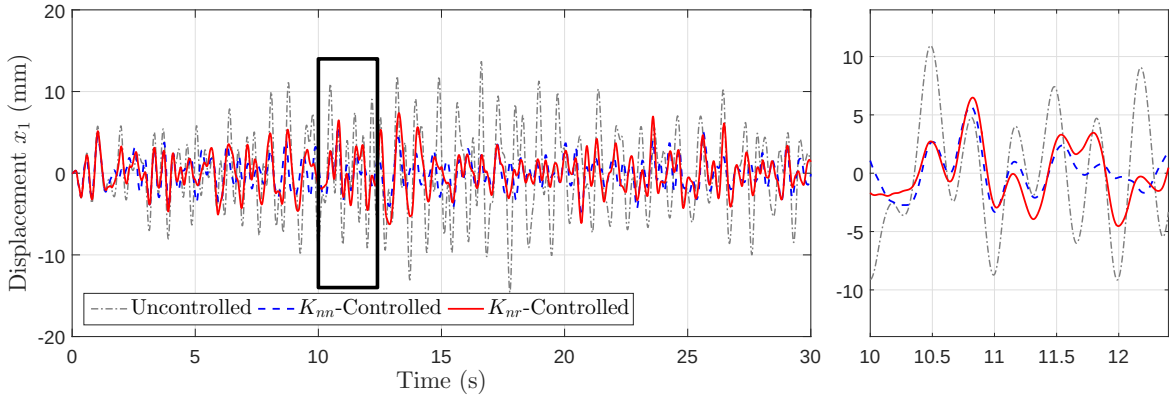

(a) Displacement at node 1 (quarter-span)

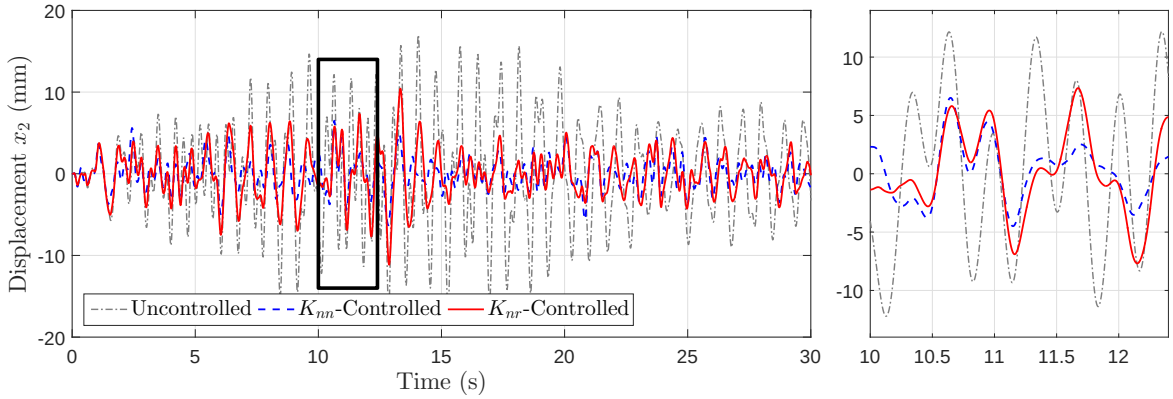

(b) Displacement at node 2 (mid-span)

Figure 7.13: Displacement responses under H_∞ control without structure or DACS uncertainty

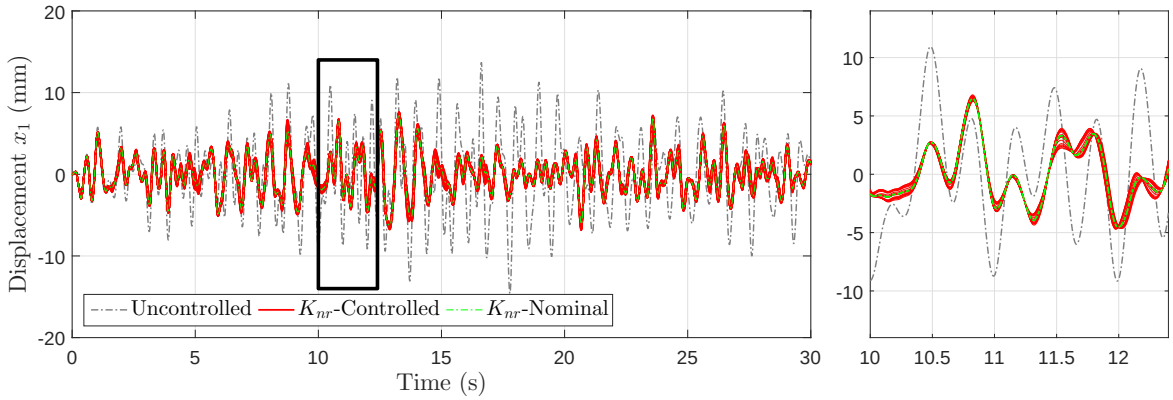

(a) Displacement at node 1 (quarter-span)

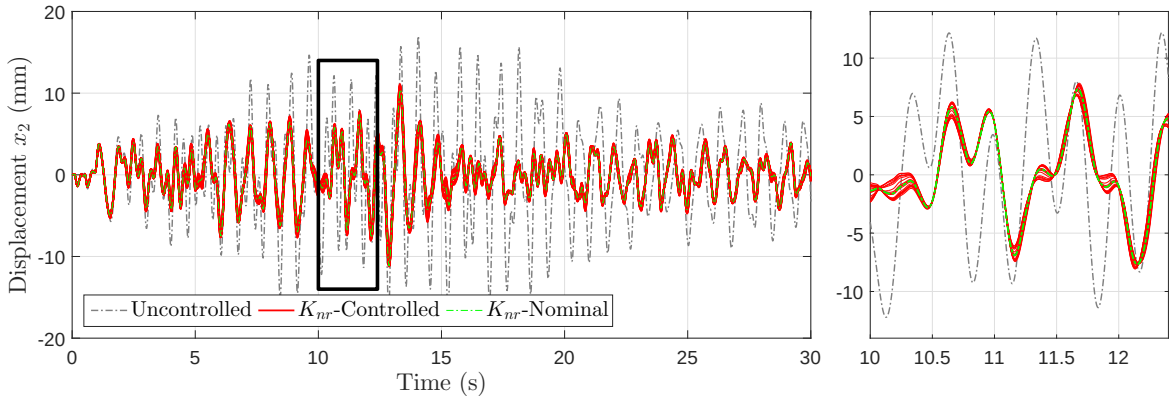

(b) Displacement at node 2 (mid-span)

Figure 7.14: Displacement responses under H_∞ control with uncertain DACS dynamics

of uncertainty, most realizations cause the closed-loop system to become unstable. On the contrary, the robust controller, designed specifically to address this uncertainty, yielded consistent performance for the range of DACS models. These results underscore the importance of addressing the uncertainty associated with the DACS prototype directly within the controller formulation. This is particularly important at control frequencies greater than 3 Hz where the UGV transfer function model varies considerably with different levels of control forces. The EMD position commands and resulting UGV tire forces for each realization are shown in Figure 7.15. As shown, the EMD operates within the physical stroke constraints of ± 75 mm and the UGV tire forces do not exceed the 400 N threshold. Although this simulation demonstrates robustness against

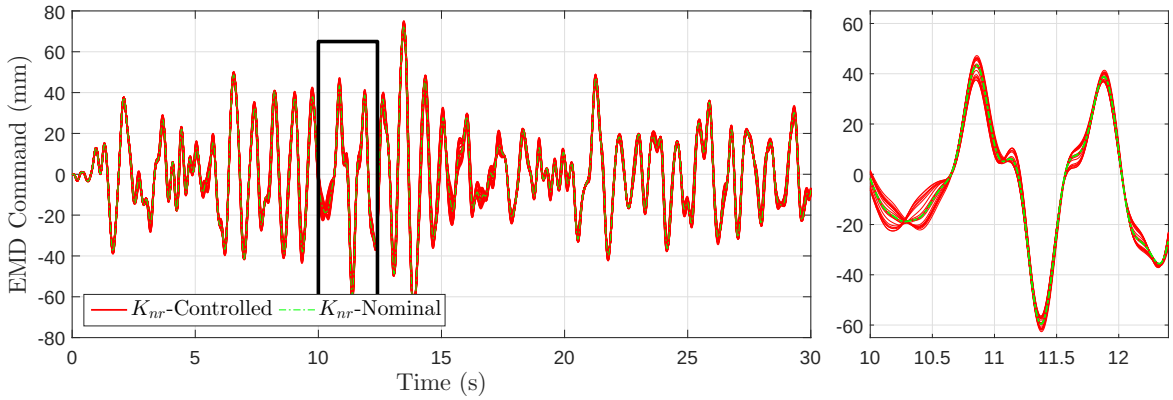

(a) EMD position commands

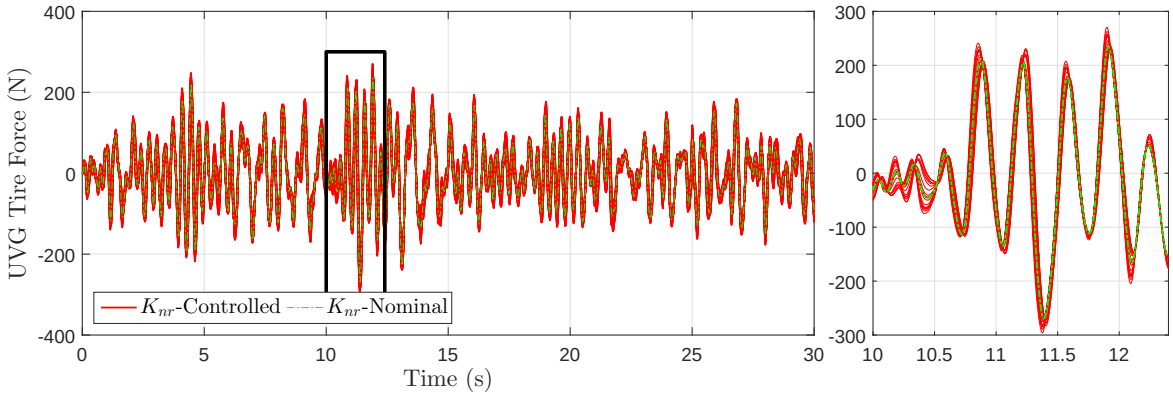

(b) UGV tire forces

Figure 7.15: Prototype input and output under H_∞ control with uncertain DACS dynamics

uncertainty in the DACS model, in many practical applications the true structure dynamics vary from those modelled for controller design which may reduce performance or lead to instabilities. As such, the effects of uncertain structure models are investigated in the third simulation.

A total of 20 realizations of the uncertain structure model (refer to Table 7.2) are randomly sampled and form the basis of the third simulation. Each realization is controlled using a realization of the uncertain DACS model randomly sampled from the uncertain UGV and EMD models. The two different H_∞ controllers considered in this case are K_{nr} and K_{rr}. Both models consider the uncertain DACS model in their formulation however only K_{rr} addresses uncertainty in the structure model. The controlled displacement responses from each controller are provided

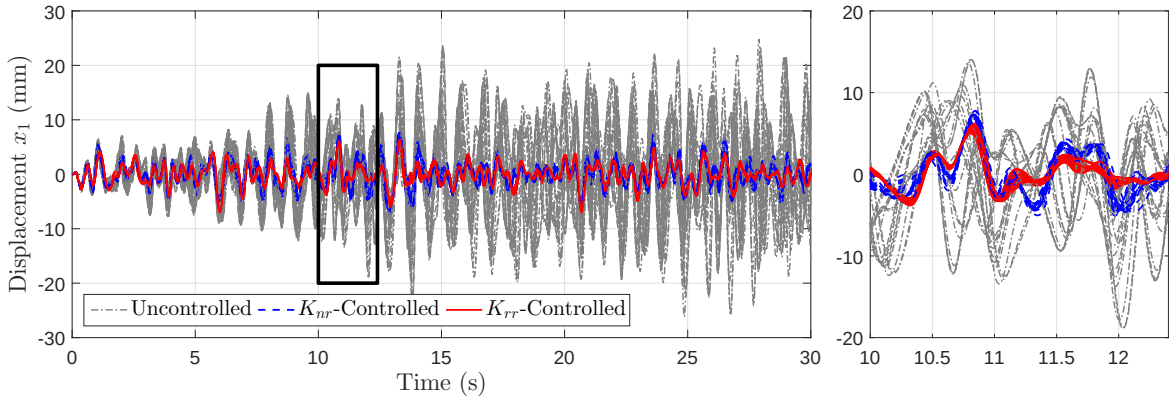

(a) Displacement at node 1 (quarter-span)

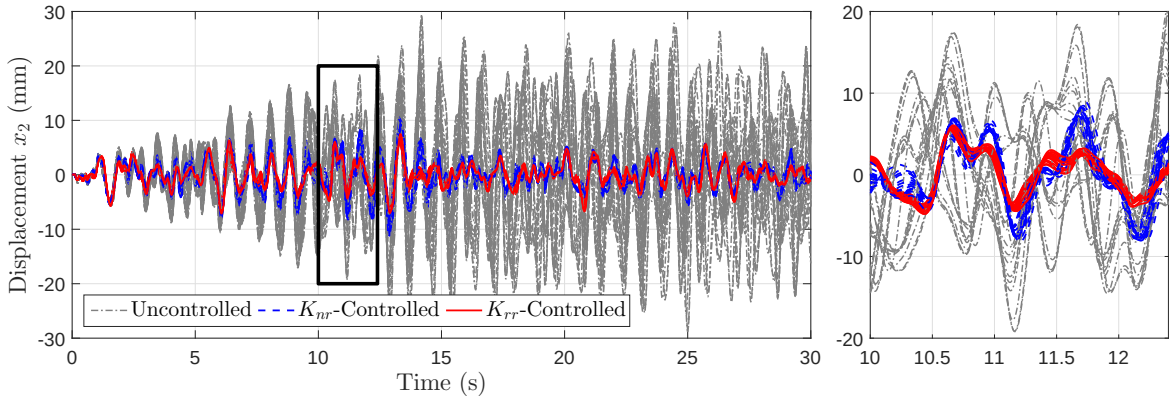

(b) Displacement at node 2 (mid-span)

Figure 7.16: Displacement responses under H_∞ control with uncertain structure dynamics

for each DOF in Figure 7.16. The range of uncontrolled structure responses is also plotted to illustrate the extent of the structure uncertainty. Although both controllers maintain closed-loop stability over the subset of realizations, the controller K_{rr}, designed to be robust to both structure and control device uncertainty, clearly outperforms the controller K_{nr} which is robust only to control device uncertainty. In addition to improved vibration suppression, the controller addressing structure uncertainty achieves a tighter banding of responses demonstrating consistent performance across the subset of realizations.

The results from these simulations verify the importance of addressing uncertainty associated with the DACS prototype directly in the control formulation and hence emphasize the benefits of

the H_∞ control formulation. It has been shown that neglecting uncertainty in the structure model and/or control device model results in degradation of the control performance at best and may lead to instabilities.

7.5 Impact of mobility on control performance

In the experimental studies conducted thus far, the prototype DACS has remained stationary at a single location on the given structure. As such, the numerical substructures for each case were formulated in the physical domain with a constant interface between the experimental and analytical substructures. The ability to reposition the active control force on a given structure is a key advantage of the DACS concept. This mobility allows a single device to change the mode in which it suppresses or control multiple modes simultaneously by navigating to the appropriate location. To demonstrate the impact of mobility as well as validate the EKF-based localization algorithm, two separate RTHS experimental programs are conducted based on the previously mapped full-scale pedestrian bridge. The need for two separate RTHS studies arises due to the fact that shake table testing does not permit physical mobility of the device and exciting the full-scale bridge in a controlled manner is expensive (i.e., requires multiple large-scale actuators). As such, the aim of the first study is to evaluate the localization performance of the prototype device and assess timing aspects associated with repositioning between various locations while the second study focuses on the verifying the overall control performance of the mobile device.

The fundamental differences between the two programs relate to the way the mobility of the device is handled and how the CSI effects are realized. In the first study – referred to as RTHS with physical mobility – the mobility of the device is physically tested by including the full-scale pedestrian bridge in both the experimental and analytical substructures. More specifically, the response of the bridge is determined through simulation in the numerical substructure while the physical bridge also forms part of the experimental substructure in order to allow the device to physically reposition itself. The limitation with this approach is that since the simulated bridge displacements are not realized in the experimental substructure, the true interaction effects cannot be studied. Nevertheless, this test methodology provides a means to accurately evaluate the localization aspect and approximate the control performance. The second study – referred to as RTHS with simulated mobility – forgoes physically localizing the robot by simulating the device positioning in the numerical substructure. In this case, the impact of mobility can be

evaluated with the prototype device on the shake table such that the simulated displacements from the numerical substructure are realized and the true interaction effects are included in the results. A brief summary of the full-scale pedestrian bridge used for testing is presented next followed by the test procedures and results from each study.

7.5.1 System description and substructuring

The test structures considered in these studies are two different lengths of the full-scale modular aluminum pedestrian bridge. For the first study, the bridge is constructed to span 16.76 m in order to be consistent with the bridge used to demonstrate EKF-SLAM. The second study increases the span to 22.9 m to leverage system models previously developed by Dey et al. [92]. The approaches used for substructuring are different for the two experimental programs and are described next.

RTHS with physical mobility: The experimental substructure in this case consists of the physical pedestrian bridge and prototype DACS. To facilitate localization, double-sided AR codes are placed on both sides of the bridge deck and aligned with the panel points to recreate the previously mapped environment. Thus, the EKF-based localization algorithm can be implemented with the map created from EKF-SLAM. For autonomous navigation the simple steering controller that was used for EKF-SLAM is expanded to include a simple proportional controller for the forward velocity command. The proportional controller determines the command velocity based on the distance away from the desired location with consideration for peak accelerations and maximum speeds. To measure the generated control force, the original bridge decking is replaced with an independent panel at mid-span and quarter-span of the bridge (i.e., coinciding with the first and second DOF). Two shear-type load cells are installed to measure for force transferred to these panels. Figure 7.17 shows the experimental substructure and independent panels. The purpose of including the pedestrian bridge as part of the experimental substructure is strictly to facilitate mobility. As a result, the bridge is also modelled analytically in the numerical substructure and simulated to determine the response. A numerical model of this bridge had been developed for RTHS testing of the MPC controllers and is used again here. The model – described by Equation 7.4 – is a three DOF lumped-mass system representing the lateral component of the bridge. In theory, the mobility aspect allows the control device to apply control forces at any position on the bridge; however, for experimental testing the control locations are constrained to the first and second DOFs which represent quarter-span and mid-span respectively. In light of this, two

(a) Overall setup (b) Prototype positioned at quarter-span

Figure 7.17: Experimental setup for modified RTHS of mobile control device

different LQG controllers are formulated based on the ICM approach to suppress the first and second mode of vibration respectively. The result is two sets of feedback gains that can be used interchangeably depending on the location of the device. Note that since the simulated responses are not realized on the physical bridge, the interaction dynamics are neglected in this case.

RTHS with simulated mobility: Since the device mobility is simulated numerically, the experimental substructure in this study consists only of the prototype device which is positioned atop four shear-type load cells on the hydraulic shake table. To address the case of spatially varying forces (i.e., moving pedestrian loads or mobile control forces), the numerical substructure is formulated in the modal domain according to Ashasi-Sorkhabi et al. [135]. The numerical model considers the first two lateral modes of vibration. Table 7.5 summarizes the modal characteristics of the 22.9 m pedestrian bridge that were identified by Dey et al. [92] through experimental testing and finite-element analysis. Further details on modelling the numerical substructure in the modal domain are provided in Appendix B. To control each of the first two modes, two different LQG controllers are formulated based on the ICM approach. The LQG controllers are designed in the modal domain and tuned through trial-and-error to ensure the prototype device operates within the prescribed limits.

Table 7.5: Modal properties and mode shapes of numerical substructure

Mode	Modal mass (kg)	Modal frequency (Hz)	Damping ratio (%)	Mode shape $f(x)$
1	867.5	1.29	3	$\sin\left(\frac{\pi x}{L}\right)$
2	694.0	2.37	1	$\sin\left(\frac{2\pi x}{L}\right)$

7.5.2 Test procedure

RTHS with physical mobility: To demonstrate the ability of the prototype device to autonomously position itself and control different modes of vibration, harmonic excitation is designed to resonate the structure in the each of the first two modes independently. The excitation consists of three 60 s segments exciting the first mode, second mode, and first mode, respectively. Each segment is separated by a 10 s transition phase resulting in an overall duration of 200 s. The positioning algorithm for the DACS is designed to be consistent with the excitation such that the device will navigate between mid-span and quarter-span to control the dominant mode. In this study, the dominant mode of vibration is determined based on the location of the peak acceleration. This crude approach is valid given the simple structure model and forced harmonic excitation. The positioning algorithm is executed alongside the LQG control algorithm in the real-time loop on the cRIO. When a change in the dominant mode is detected, a command is issued to pause the EMD and initiate the localization algorithm to reposition the device. After reaching the desired position a second command is issued to set the appropriate feedback gains and resume control. It should be noted that the numerical substructure in this case contains two separate restoring force inputs corresponding to the first and second DOFs.

RTHS with simulated mobility: To showcase the ability to handle spatially varying loads, a Fourier series pedestrian load model is adopted to simulate the forces induced by walking pedestrians. The model uses dynamic load factors of 0.1 and 0.05 for the first and second mode respectively and assumes a pedestrian weight of 700 N and step frequency of 1.2 Hz. The pedestrians are assumed to travel at a constant speed and enter the bridge as soon as the previous pedestrian exits the bridge (i.e., only a single pedestrian is on the bridge at any given time). Further details on the pedestrian load model are provided in Appendix B. The lateral response of the bridge is computed by superimposing the first and second vibration modes which are simulated independently. Although the numerical substructuring framework also permits spatially varying

control forces (i.e., the device can be positioned at any location on the bridge), the positioning algorithm for the DACS is simplified to choosing from a set of predefined locations. Since only the first two modes are considered, the predefined control locations include quarter-span, mid-span and three-quarter-span. A simple algorithm based on the location of the peak acceleration is used to decide which mode to control and which position to control from. The simulation consists of three operational stages: sensing, positioning, and control. At the onset of the test, the sensing stage is active and the response of the bridge is continuously monitored to determine the desired control location. Once the control location has been identified, the system transitions to the positioning stage where the mobility of the device is simulated in the numerical substructure. Arrival at the desired location triggers the control stage where the appropriate LQG gains are used to determine the optimal control force.

7.5.3 Results

RTHS with physical mobility: The control performance and impact of mobility is shown in Figure 7.18 which compares the uncontrolled and controlled responses at mid-span and quarter-span. At the start of the experiment, the prototype device is positioned at an arbitrary location between the two control locations and immediately instructed to navigate to mid-span. This positioning required approximately 20 s and is reflected in the consistency between the controlled and uncontrolled responses (i.e., no control effect) in Figure 7.18. After reaching mid-span, the LQG controller is initiated and the resulting control forces effectively suppressed the displacement response by over 70 %. After the positioning algorithm determined the second mode is dominating the response, the DACS suspends control operations and begins navigating to quarter-span. Upon arrival, vibration control resumes with new feedback gains leading to a 40 % reduction in peak displacement at quarter-span. Finally, the third segment of excitation causes the device to return to mid-span where it yields a similar control effect to that demonstrated during the first segment. Table 7.6 compares the RMS value of the uncontrolled and controlled responses at mid-span and quarter-span. The RMS value is computed for a 30 s window in each segment to separate the control performance of the different modes. The effective control performance across all three segments demonstrates the ability of the prototype device to control different modes of vibration by repositioning itself on the structure and updating the control algorithm.

RTHS with simulated mobility: At the onset of the test, the sensing stage identified quarter-

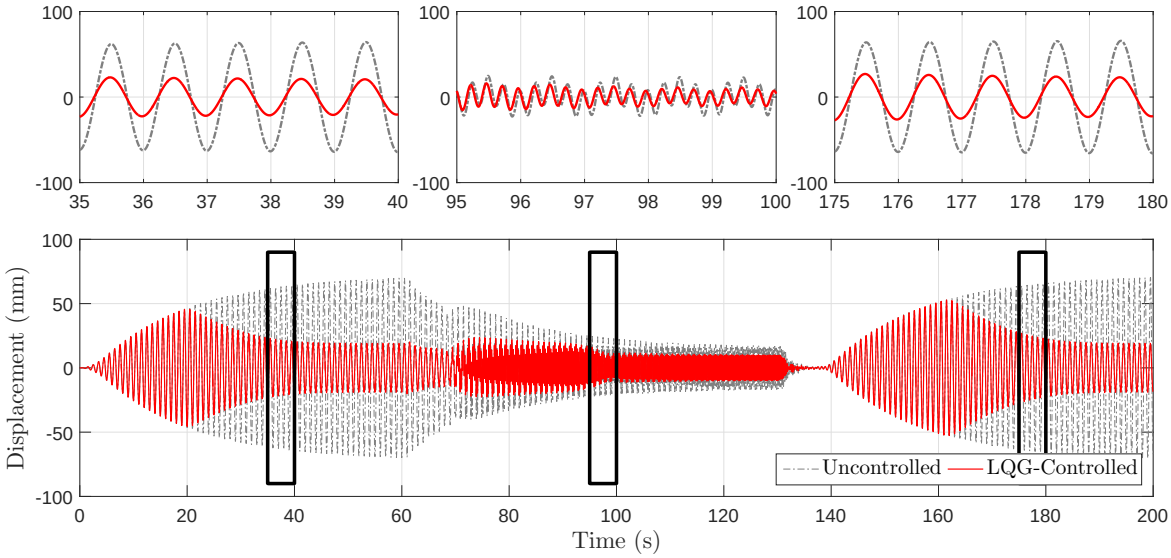

(a) Displacement responses at quarter-span

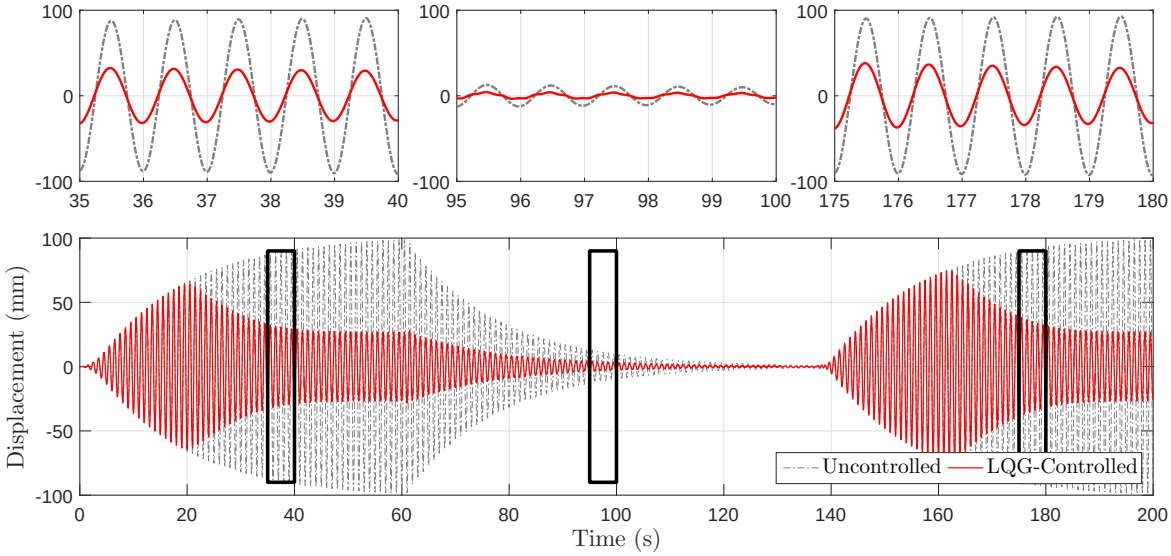

(b) Displacement responses at mid-span

Figure 7.18: Uncontrolled and controlled displacement responses using a mobile DACS

Table 7.6: Effectiveness of DACS under forced harmonic excitation

Segment	Quarter-span Response (m)			Mid-span Response (m)		
	Uncontrolled RMS	Controlled RMS	Reduction %	Uncontrolled RMS	Controlled RMS	Reduction %
1	0.0465	0.0148	68	0.0658	0.0209	68
2	0.0115	0.0069	40	0.0036	0.0011	69
3	0.0473	0.0162	66	0.0670	0.0229	66

span as the optimal control location. Since the device is assumed to start at end of the bridge, the positioning stage involves simulating the navigation of the device to quarter-span. Upon transitioning to the control stage, the LQG controller feedback gains corresponding to the second mode are used in conjunction with a compensator block to determine the desired EMD position commands which are applied to the prototype device. The control effect is shown in Figure 7.19 which compares the uncontrolled and controlled responses of the 22.9 m pedestrian bridge subjected to a single moving pedestrian load. With the prototype device positioned at quarter-span and designed specifically to suppress the second mode of vibration, response reduction is expected at the quarter-span and three-quarter-span with minimal impact on the displacement at mid-span. The RMS of the displacement response is reduced by approximately 30 % at quarter-span and three-quarter-span while a slight increase in the response is observed at mid-span due to modal-spillover.

The demonstrated control performance taking into account the CSI dynamics motivates the use of mobile control devices capable of repositioning at desired locations on the structure.

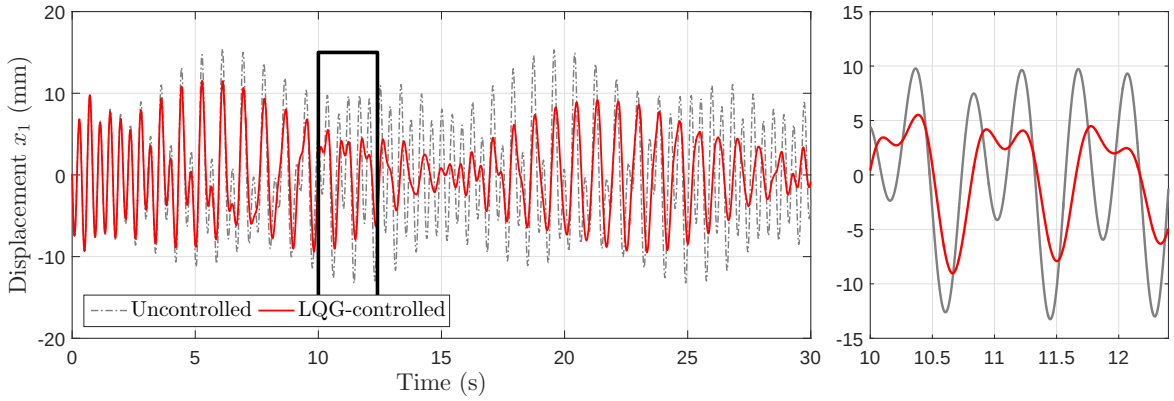

(a) Displacement responses at quarter-span

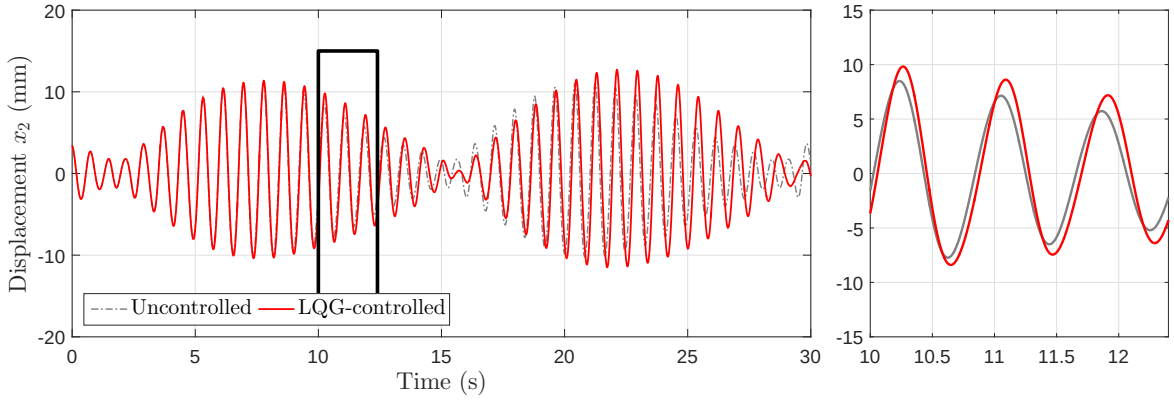

(b) Displacement responses at mid-span

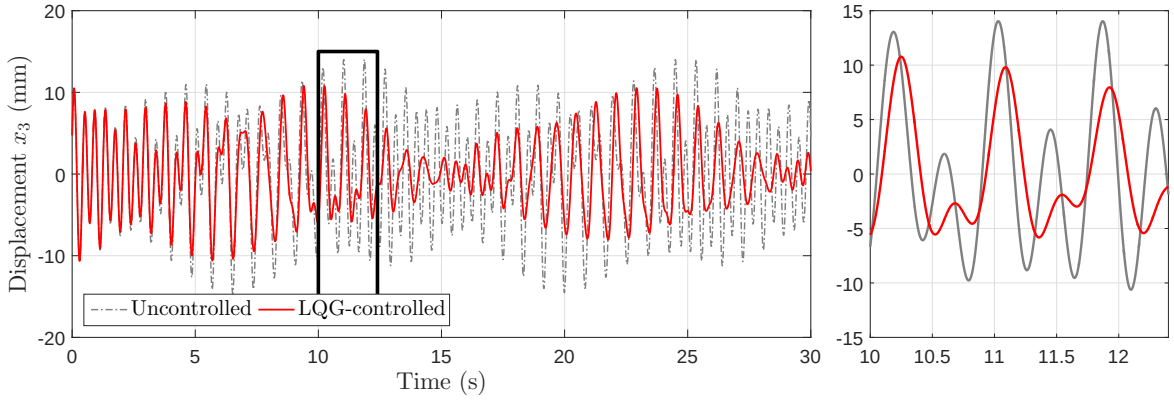

(c) Displacement responses at three-quarter-span

Figure 7.19: Control performance of prototype on pedestrian bridge under pedestrian loading

Chapter 8

Conclusions

The concept of deployable, autonomous vibration control systems for civil infrastructure is introduced for the first time and explored thoroughly in this dissertation. Given the requirements for deployability and autonomy, a prototype device is constructed to study the effects of CSI and evaluate various controller formulations in the presence of operating constraints and model uncertainty. Both numerical simulations and full-scale experimental tests are conducted to demonstrate the potential for DACSs in immediate, short-term control applications. This section summarizes the significant contributions from this research, discusses the key conclusions, and proposes several directions for future study.

8.1 Significant contributions

The research presented in this thesis has led to several notable contributions which are summarized below. Several of these contributions have been disseminated in peer-reviewed journals or conference proceedings already, with more forth-coming. A complete listing of the publications that have resulted directly from this work is provided in Appendix A.

1. The novel concept of a DACS is established and assessed using a prototype device which represents the first application of a robotic platform for structural control applications. Development of this prototype involved forming a framework for experimental and theoretical system modelling of DACS components and quantifying the associated uncertainty.

2. The mobility provided by the UGV marks the first application of a mobile control system for structural control applications. Achieving mobility required the implemented of a SLAM solution suitable for navigating a range of bridges with sparse and/or repeated features. The advantages and capabilities of a mobile control system were demonstrated through full-scale experimental testing and the application of a novel RTHS algorithm.

3. The performance of any DACS relies on the ability to properly account for the dynamic interaction between the structure and prototype control system. This thesis addresses the CSI effects by adopting position feedback control for the actuator and incorporating an acceleration feedback loop for the UGV dynamics. The validity of this methodology requires accurate position tracking of the EMD under base excitation and assumes the UGV can be modelled as a SDOF system. Both of these requirements were verified experimentally.

4. The development of the prototype DACS introduced new physical operating constraints that must be accounted for in the control formulation. Contained in this thesis is a novel adaptive MPC control formulation that accounts for both hard and soft constraints on the position command and UGV tire force respectively. A framework for implementing real-time MPC on full-scale structures is also presented and demonstrated through experimental RTHS.

5. A robust controller was formulated based on H_∞ theory where controller model errors – introduced by approximated the UGV as a linear system – are treated as uncertainty in the control formulation. The controller was also shown to be robust to errors in the plant model which is advantageous for deploying the device on structures without high-fidelity models.

8.2 Conclusions

The comprehensive assessment of the prototype device has produced several key findings with respect to the advantages, limitations, and potential impact of DACS. These observations are summarized in several key conclusions:

1. The concept of DACSs was shown to be a favourable alternative to existing control devices when targeting immediate, short-term, vibration control applications. The deployability

aspect facilitates rapid implementation on a range of structures while the autonomy aspect provides the required adaptability to control a wide bandwidth of vibrations and respond to changes in the dynamic response. As demonstrated through the development of a small-scale prototype device, the concepts of deployability and autonomy can be achieved by integrating a mobile platform, actuation device, and computational hardware.

2. Experimental testing on the prototype device revealed that modest control forces can be achieved without relying on a rigid or fixed connection to the underlying structure. This finding proved to be central in achieving mobility which allows the device to readily reposition itself on the structure. Furthermore, the implementation of an EKF-SLAM algorithm demonstrated the capacity of such systems to navigate autonomously. This ability provides the opportunity to augment the control algorithm to include the location of the control force as an additional parameter in the optimization.

3. A framework for addressing the interaction effects between the prototype DACS and underlying structure was presented and validated experimentally. The use of a position-feedback controller for the EMD was shown to reject base disturbances and thus allow the separation of the EMD dynamics from the overall device model. The resulting interaction dynamics, derived analytically assuming a SDOF system model for the UGV, were shown to be an acceleration feedback loop scaled by the mass of the prototype device. The accuracy of the overall system model accounting for interaction effects was validated experimentally through RTHS.

4. The use of a UGV as a mobile platform and EMD as an active control device introduced new challenges for controller design including model uncertainty and physical operating constraints. The key operating constraints were shown to be the stroke limitation of the EMD and peak tire force in the UGV (i.e., to prevent slipping). Traditional linear quadratic control methods such as LQG do not systematically address these constraints and were designed by tuning the weighting matrices through trial and error to ensure the specified limits are not exceeded. In general, this may lead to conservative controller designs. An MPC algorithm was implemented for the prototype device and shown to effectively address the physical operating constraints. A framework for real-time implementation was provided and demonstrated through RTHS of a full-scale pedestrian bridge. In an effort to address model uncertainty, a robust H_∞ controller was designed for the prototype device. A

numerical study demonstrated effective control performance and robustness to uncertainty in both the DACS model and underlying structure model.

5. The impact of mobility on control performance was shown through a combination of full-scale experimental testing and RTHS. The ability of the device to reposition itself at prescribed locations on the structure was key in effectively suppressing different modes of vibration using a single device.

8.3 Directions for future study

Throughout the course of this thesis work, many aspects and limitations with DACS were uncovered. Possible directions for future work to bring this concept into a workable technology are summarized below:

Robust controller formulation with constraints: The MPC formulation and H_∞ robust controller presented herein were shown to effectively address the presence of operating constraints and model uncertainty respectively. A current limitation with the presented MPC algorithm is the inability to address model uncertainty directly in the formulation and thus robustness can only be measured after the controller has been designed. Furthermore, although the H_∞ robust control formulation handles uncertainty in both the controller model and plant model efficiently, the frequency-dependent weighting functions do not permit direct modelling of time-domain constraints such as EMD position or UGV tire force. In light of this, one immediate direction for future work is to formulate and implement a robust, constrained controller such that both model uncertainty and physical operating constraints are directly accounted for in the optimization.

Optimizing device location: A number of solutions have been presented in the literature for determining the optimal location of fixed control devices for structural control. However, the mobility aspect of DACSs adds an additional layer to this problem by providing the capability to reposition over time. As such, the optimal location of the device can be time-varying and depend on many factors including the external excitation, structural response, and control objective. Although the traditional methods for determining the location of the control device (i.e., position near the peaks of the desired mode shape to control) remain valid for DACSs, the ability to augment the controller formulation to optimize the position of the device has the potential to

improve overall performance. Developing control algorithms for the simultaneous positioning of multiple devices in order to achieve a common objective is also a project worth undertaking.

Incorporating system identification: The mobility provided by the UGV combined with the force generation of the EMD, presents an opportunity to collect input-output data for system identification purposes. Incorporating system identification procedures into the overall system reduces the accuracy requirement on *a priori* modelling and has the potential to facilitate the deployment of a DACS on a completely unknown structure.

Nonlinear control: In modelling the prototype device, a linear model was used to approximate the inherently non-linear UGV dynamics. Although the potential model-errors were addressed through a robust controller formulation, there is merit in fitting non-linear models for the UGV dynamics and implementing corresponding non-linear control algorithms. This will lead to a better understanding of the performance limitations for the different modelling approaches and overall device.

Enhancing prototype capabilities: The prototype device was developed using a number of readily available components (i.e., UGV, EMD, and cRIO) with minimal customization. This was intended to demonstrate the range of systems that can be integrated in order to achieve deployability and autonomy. A potential area of future work involves customizing the device for a particular implementation (i.e., pedestrian bridges). Customization could include adding actuators to control the vertical component of pedestrian bridges, replacing the rubber tires with solid wheels, or transitioning to a rail-mounted vehicle.

References

[1] J. J. Connor. *Introduction to structural motion control*. Prentice Hall, 2003.

[2] B. F. Spencer Jr and S. Nagarajaiah. State of the art of structural control. *Journal of Structural Engineering*, 129(7):845–856, 2003.

[3] G. W. Housner, L. A. Bergman, T. K. Caughey, A. G. Chassiakos, R. O. Claus, S. F. Masri, R. E. Skelton, T. T. Soong, B. F. Spencer Jr, and J. T. P. Yao. Structural control: past, present, and future. *Journal of Engineering Mechanics*, 123(9):897–971, 1997.

[4] F. Yi and S. J. Dyke. Structural control systems: performance assessment. *Proceedings of the 2000 American Control Conference*, pages 14–18. IEEE, 2000.

[5] T. T. Soong and B. F. Spencer Jr. Supplemental energy dissipation: state-of-the-art and state-of-the-practice. *Engineering Structures*, 24(1):243–259, 2002.

[6] T. K. Datta. A state-of-the-art review on active control of structures. *Journal of Earthquake Technology*, 40(1):1–17, 2003.

[7] F. Casciati, J. Rodellar, and U. Yildirim. Active and semi-active control of structures - theory and applications: A review of recent advances. *Journal of Intelligent Material Systems and Structures*, 23(11):1181–1195, 2012.

[8] C. T. Georgakis and N. G. Jorgensen. Change in mass and damping on vertically vibrating footbridges due to pedestrians. *Topics in Dynamics of Bridges, Volume 3*, pages 37–45. Springer, 2013.

[9] B. F. Spencer Jr and M. K. Sain. Controlling buildings: A new frontier in feedback. *IEEE Control Systems*, 17(6):19–35, 1997.

[10] T. T. Soong and B. F. Spencer Jr. Active, semi-active and hybrid control of structures. *Bulletin of the New Zealand Society for Earthquake Engineering*, 33(3):387–402, 2000.

[11] J. H. Koo, M. Ahmadian, M. Setareh, and T. Murray. In search of suitable control methods for semi-active tuned vibration absorbers. *Modal Analysis*, 10(2):163–174, 2004.

[12] J. Q. Sun, M. R. Jolly, and M. A. Norris. Passive, adaptive and active tuned vibration absorbers—a survey. *Journal of Mechanical Design*, 117(2):234–242, 1995.

[13] M. D. Symans and M. C. Constantinou. Semi-active control systems for seismic protection of structures: a state-of-the-art review. *Engineering Structures*, 21(6):469–487, 1999.

[14] S. J. Dyke, B. F. Spencer Jr, M. K. Sain, and J. D. Carlson. Experimental verification of semi-active structural control strategies using acceleration feedback. *Proceedings of the 3^{rd} International Conference on Motion and Vibration Control*, pages 291–296, 1996.

[15] X. Cahis, L. Bozzo, and L. Torres. Experimental studies of various innovative energy dissipation devices. *Proceedings of the 11^{th} European Conference on Earthquake Engineering*. A.A. Balkema, 1998.

[16] J. T. P. Yao. Concept of structural control. *Journal of the Structural Division*, 98(7): 1567–1574, 1972.

[17] T. E. Saaed, G. Nikolakopoulos, J. E. Jonasson, and H. Hedlund. A state-of-the-art review of structural control systems. *Journal of Vibration and Control*, 21(5):919–937, 2015.

[18] T. T. Soong and G. P. Cimellaro. Future directions in structural control. *Structural Control & Health Monitoring*, 16(1):7–16, 2009.

[19] M. Setareh and R. D. Hanson. Tuned mass dampers to control floor vibration from humans. *Journal of Structural Engineering*, 118(741):741–762, 1992.

[20] I. Kourakis. *Structural systems and tuned mass dampers of super-tall buildings: case study of Taipei 101*. PhD. Thesis, Massachusetts Institute of Technology, 2007.

[21] P. Dallard, A. J. Fitzpatrick, A. Flint, S. Le Bourva, A. Low, R. M. Smith, and M. Willford. The London Millenium Footbridge. *The Structural Engineer*, 79(22):17–35, 2001.

[22] M. Kitagawa. Technology of the Akashi Kaikyo bridge. *Structural Control & Health Monitoring*, 11(2):75–90, 2004.

[23] K. Yamamoto and M. Kawahara. Structural oscillation control using tuned liquid damper. *Computers & Structures*, 71(4):435–446, 1999.

[24] R. H. Zhang and T. T. Soong. Seismic design of viscoelastic dampers for structural applications. *Journal of Structural Engineering*, 118(5):1375–1392, 1992.

[25] S. W. Park. Analytical modeling of viscoelastic dampers for structural and vibration control. *Journal of Solids and Structures*, 38(44):8065–8092, 2001.

[26] T. T. Soong. *Active structural control: theory and practice*. Longman Scientific and Technical, Essex, UK, 1990.

[27] R. Alkhatib and M. F. Golnaraghi. Active structural vibration control: A review. *Shock and Vibration Digest*, 35(5):367–383, 2003.

[28] T. Kobori, N. Koshika, K. Yamada, and Y. Ikeda. Seismic-response-controlled structure with active mass driver system. Part 1: Design. *Earthquake Engineering & Structural Dynamics*, 20(2):133–149, 1991.

[29] C. Zhang and J. Ou. Control strategies and experimental verifications of the electromagnetic mass damper system for structural vibration control. *Earthquake Engineering & Engineering Vibration*, 7(2):181–192, 2008.

[30] F. Ubertini, I. Venanzi, and G. Comanducci. Considerations on the implementation and modeling of an active mass driver with electric torsional servomotor. *Mechanical Systems and Signal Processing*, 58(1):53–69, 2015.

[31] H. P. Gavin, R. D. Hanson, and F. E. Filisko. Electrorheological dampers, part I: Analysis and design. *Journal of Applied Mechanics*, 63(3):669–675, 1996.

[32] S. J. Dyke, B. F. Spencer Jr, M. K. Sain, and J. D. Carlson. Modeling and control of magnetorheological dampers for seismic response reduction. *Smart Materials and Structures*, 5(1):565–575, 1996.

[33] A. Kareem, T. Kijewski, and Y. Tamura. Mitigation of motions of tall buildings with specific examples of recent applications. *Wind and Structures*, 2(3):201–251, 1999.

[34] A. Nishitani and Y. Inoue. Overview of the application of active/semiactive control to building structures in Japan. *Earthquake Engineering & Structural Dynamics*, 30(11): 1565–1574, 2001.

[35] J. P. Lynch. *Active Structural Control Research at Kajima Corporation*. The National Science Foundation's Summer Institute in Japan Program, Research Project, 1998.

[36] B. D. Anderson and J. B. Moore. *Optimal control: linear quadratic methods.* Dover Publications Inc., Mineola, New York, 2007.

[37] R. E. Kalman. A new approach to linear filtering and prediction problems. *Journal of Basic Engineering*, 82(1):35–45, 1960.

[38] J. P. Conte and B. F. Peng. Fully nonstationary analytical earthquake ground-motion model. *Journal of Engineering Mechanics*, 123(1):15–24, 1997.

[39] M. Gutierrez Soto and H. Adeli. Recent advances in control algorithms for smart structures and machines. *Expert Systems*, 34(2):12205, 2017.

[40] E. F. Camacho and C. Bordons. *Model predictive control*. Springer Science and Business Media, London, UK, 2013.

[41] J. Rodellar, A. H. Barbat, and J. M. Martin-Sanchez. Predictive control of structures. *Journal of Engineering Mechanics*, 113(6):797–812, 1987.

[42] F. Lopez-Almansa, R. Andrade, J. Rodellar, and A. M. Reinhorn. Modal predictive control of structures I: Formulation. *Journal of Engineering Mechanics*, 120(8):1743–1760, 1994.

[43] C. E. Garcia, D. M. Prett, and M. Morari. Model predictive control: theory and practice - a survey. *Automatica*, 25(3):335–348, 1989.

[44] G. Mei, A. Kareem, and J. C. Kantor. Real-time model predictive control of structures under earthquakes. *Earthquake Engineering & Structural Dynamics*, 30(7):995–1019, 2001.

[45] G. Mei, A. Kareem, and J. C. Kantor. Model predictive control of structures under earthquakes using acceleration feedback. *Journal of Engineering Mechanics*, 128(5): 547–585, 2002.

[46] G. Mei, A. Kareem, and J. C. Kantor. Model predictive control of wind-excited building: benchmark study. *Journal of Engineering Mechanics*, 130(4):459–465, 2004.

[47] E. A. Johnson, W. M. Elhaddad, and S. F. Wojtkiewicz. Performance and robustness of hybrid model predictive control for controllable dampers in building models. *Proceedings of Sensors and Smart Structures Technologies for Civil, Mechanical, and Aerospace Systems*. SPIE, 2016.

[48] C. W. Yang, L. Chung, L. Wu, and N. Chung. Modified predictive control of structures with direct output feedback. *Structural Control & Health Monitoring*, 18(8):922–940, 2011.

[49] L. L. Chung. Modified predictive control of structures. *Engineering Structures*, 21(12): 1076–1085, 1999.

[50] H. Peng, F. Li, S. Zhang, and B. Chen. A novel fast model predictive control with actuator saturation for large-scale structures. *Computers & Structures*, 187(1):35–49, 2017.

[51] Y. Chen, S. Zhang, H. Peng, B. Chen, and H. Zhang. A novel fast model predictive control for large-scale structures. *Journal of Vibration and Control*, 23(13):2190–2205, 2017.

[52] G. Takács and B. Rohal'-Ilkiv. Model predictive control algorithms for active vibration control: a study on timing, performance and implementation properties. *Journal of Vibration and Control*, 20(13):2061–2080, 2014.

[53] K. Zhou, J. C. Doyle, and K Glover. *Robust and optimal control*. Prentice Hall, New Jersey, NY., 1996.

[54] J. Suhardjo. *Frequency domain techniques for control of civil engineering structures with some robustness considerations*. PhD. Thesis, University of Notre Dame, 1990.

[55] B. F. Spencer Jr, J. Suhardjo, and M. K. Sain. Frequency domain optimal control strategies for aseismic protection. *Journal of Engineering Mechanics*, 120(1):135–158, 1994.

[56] W. E. Schmitendorf, F. Jabbari, and J. N. Yang. Robust control techniques for buildings under earthquake excitation. *Earthquake Engineering & Structural Dynamics*, 23(5): 539–552, 1994.

[57] H. A. Smith and J. G. Chase. Robust disturbance rejection using H_∞ control for civil structures. *Proceedings of the 1st World Conference on Structural Control*, pages 33–42. International Association for Structural Control, 1994.

[58] J. Suhardjo, B. F. Spencer Jr, and A. Kareem. Frequency domain optimal control of wind-excited buildings. *Journal of Engineering Mechanics*, 118(12):2463–2481, 1992.

[59] S. G. Wang, P. N Roschke, and H.Y. Yeh. Robust control for structural systems with uncertainties. *Smart Systems for Bridges, Structures, and Highways*. Smart Structures and Materials, 1999.

[60] Z. Li and H. Adeli. New discrete-time robust H_2/H_∞ algorithm for vibration control of smart structures using linear matrix inequalities. *Engineering Applications of Artificial Intelligence*, 55(1):47–57, 2016.

[61] Z. Zhou, M. Wang, and T. Liang. H_∞ model predictive control of discrete-time constrained singular piecewise-affine systems with time delay. *Proceedings of the 4th International Conference on Instrumentation and Measurement Computer, Communication, and Control*, pages 447–461. IEEE, 2014.

[62] M. P. Singh, E. E. Matheu, and L. E. Suarez. Active and semi-active control of structures under seismic excitation. *Earthquake Engineering & Structural Dynamics*, 26(2):193–213, 1997.

[63] R. Adhikari and H. Yamaguchi. Sliding mode control of buildings with ATMD. *Earthquake Engineering & Structural Dynamics*, 26(4):409–422, 1997.

[64] A. R. Zare and M. Ahmadizadeh. Modified sliding mode design of passive viscous fluid control systems for nonlinear structures. *Engineering Structures*, 162(1):245–256, 2018.

[65] M. Soleymani, A. H. Abolmasoumi, H. Bahrami, A. Khalatbari, E. Khoshbin, and S. Sayahi. Modified sliding mode control of a seismic active mass damper system consid-

ering model uncertainties and input time delay. *Journal of Vibration and Control*, 24(6): 1051–1064, 2018.

[66] L. M. Jansen and S. J. Dyke. Semiactive control strategies for MR dampers: comparative study. *Journal of Engineering Mechanics*, 126(8):795–803, 2000.

[67] N. H. McClamroch and H. P. Gavin. Closed loop structural control using electrorheological dampers. *Proceedings of the 1995 American Control Conference*, pages 4173–4177. IEEE, 1995.

[68] Z. Wu and T. T. Soong. Modified bang-bang control law for structural control implementation. *Journal of Engineering Mechanics*, 122(8):771–777, 1996.

[69] I. Chang and J. Bentsman. Constrained discrete-time state-dependent Riccati equation technique: a model predictive control approach. *Proceedings of the 52nd Conference on Decision and Control*, pages 5125–5130. IEEE, 2013.

[70] A. L. Materazzi and F. Ubertini. Robust structural control with system constraints. *Structural Control & Health Monitoring*, 19(3):472–490, 2012.

[71] J. Mongkol, B. K. Bhartia, and Y. Fujino. On linear saturation control of buildings. *Earthquake Engineering & Structural Dynamics*, 25:1353–1371, 1996.

[72] I. Venanzi. A review on adaptive methods for structural control. *The Open Civil Engineering Journal*, 10(1):653–667, 2016.

[73] S. J. Dyke, B. F. Spencer Jr, P. Quast, and M. K. Sain. Role of control-structure interaction in protective system design. *Journal of Engineering Mechanics*, 121(2):322–338, 1995.

[74] M. Battaini, G. Yang, and B. F. Spencer Jr. Bench-scale experiment for structural control. *Journal of Engineering Mechanics*, 126(2):140–148, 2000.

[75] I. Venanzi, L. Ierimonti, and F. Ubertini. Effects of control-structure interaction in active mass driver systems with electric torsional servomotor for seismic applications. *Bulletin of Earthquake Engineering*, 15(4):1543–1557, 2017.

[76] C. Zhang and J. Ou. Control structure interaction of electromagnetic mass damper system for structural vibration control. *Journal of Engineering Mechanics*, 134(5):428–437, 2008.

[77] G. M. Stewart and M. A. Lackner. The effect of actuator dynamics on active structural control of offshore wind turbines. *Engineering Structures*, 33(5):1807–1816, 2011.

[78] J. Liu, H. J. Liu, and S. J. Dyke. Control-structure interaction for micro-vibration structural control. *Smart Materials and Structures*, 21(10), 2012.

[79] C. Haas, M. Skibniewski, and E. Budny. Robotics in civil engineering. *Computer-Aided Civil and Infrastructure Engineering*, 10(5):371–381, 1995.

[80] J. Valls Miro, F. De Bruijn, G. Dissanayake, O. Boisard, and P. Ton. Robot-assisted inspection of concrete box girders in bridges. *Proceedings of the 8^{th} Austroads Bridge Conference*. Austroads Ltd., 2011.

[81] H. M. La, R. S. Lim, B. B. Basily, N. Gucunski, J. Yi, A. Maher, F. A. Romero, and H. Parvardeh. Autonomous robotic system for high-efficiency non-destructive bridge deck inspection and evaluation. *ASME Transactions on Mechatronics*, 18(6):1655–1664, 2013.

[82] N. Charron, E. McLaughlin, S. Phillips, K. Goorts, S. Narasimhan, and S. L. Waslander. Automated bridge inspection using mobile ground robotics. *Journal of Structural Engineering*, In Press, Accepted Feb. 26, 2019.

[83] M. N. Gillins, D. T. Gillins, and C. Parrish. Cost-effective bridge safety inspections using unmanned aircraft systems. *Proceedings of the 2016 Geotechnical and Structural Engineering Congress*, pages 1931–1940. ASCE, 2016.

[84] A. Ellenberg, A. Kontsos, F. Moon, and I. Bartoli. Bridge deck delamination identification from unmanned aerial vehicle infrared imagery. *Automation in Construction*, 72(1):155–165, 2016.

[85] A. Khaloo, D. Lattanzi, K. Cunningham, R. Dell'Andrea, and M. Riley. Unmanned aerial vehicle inspection of the Placer River Trail ridge through image-based 3D modelling. *Structure and Infrastructure Engineering*, 14(1):124–136, 2018.

[86] S. Thrun, W. Burgard, and D. Fox. *Probabilistic robotics*. MIT Press, 2005.

[87] H. Durrant-Whyte, D. Rye, and E. Nebot. Localization of autonomous guided vehicles. *Robotics Research*, pages 613–625. Springer, London, 1996.

[88] H. Durrant-Whyte and T. Bailey. Simultaneous localization and mapping: Part I. *IEEE Robotics & Automation Magazine*, 13(2):99–110, 2006.

[89] R. Smith, M. Self, and P Cheeseman. Estimating uncertain spatial relationships in robotics. I. J. Cox and G. T. Wilfon, editors, *Autonomous Robot Vehicles*, pages 167–193. Springer, 1990.

[90] J. Aulinas, Y. Petillot, J. Salvi, and X. Llado. The SLAM problem: A survey. *Proceedings of the International Conference of the Catalan Association for Artificial Intelligence*, pages 363–371. IOS Press, 2008.

[91] Maadi Group Inc. MakeABridge. *Catalog*, 2015. URL www.makeabridge.com/pdf/catalog{_}en.pdf.

[92] P. Dey, S. Narasimhan, and S. Walbridge. Evaluation of design guidelines for the serviceability assessment of aluminum pedestrian bridges. *Journal of Bridge Engineering*, 22(1): 04016109, 2016.

[93] Maadi Group Inc. MakeABridge military testing, 2016. URL http://www.maadigroup.com.

[94] C. A. Jones, P. Reynolds, and A. Pavic. Vibration serviceability of stadia structures subjected to dynamic crowd loads: A literature review. *Journal of Sound and Vibration*, 330(8):1531–1566, 2011.

[95] E. J. Hudson, P. Reynolds, M. Nelson, N. Christie, and V. Salcedo. Active control of concert-induced vibrations. *Proceedings of the 2016 Geotechnical and Structural Engineering Congress*, pages 1729–1741. ASCE, 2016.

[96] Clearpath Robotics. Husky: Unmanned ground vehicle. *Brochure*, 2014.

[97] K. Goorts, A. Ashasi-Sorkhabi, and S. Narasimhan. Deployable active mass dampers for vibration mitigation in lightweight bridges. *Journal of Structural Engineering*, 143(12): 04017159, 2017.

[98] Test Dynamics. National Instruments cRIO-9035 Controller, 2018. URL http://www.testdynamics.co.za/ProductPage.php?id=NI9035.

[99] C. T. Chi, Y. T. Wang, S. T. Cheng, and C. A. Shen. Robot simultaneous localization and mapping using a calibrated kinect sensor. *Sensors and Materials*, 26(5):353–364, 2014.

[100] C. Zhang and J. Ou. Modeling and dynamical performance of the electromagnetic mass driver system for structural vibration control. *Engineering Structures*, 82(1):93–103, 2015.

[101] S. J. Moon, T. Y. Chung, C. W. Lim, and D. H. Kim. A linear motor damper for vibration control of steel structures. *Mechatronics*, 14(10):1157–1181, 2004.

[102] P. Zhang. *Advanced industrial control technology*. William Andrew, 2010.

[103] R.M. Hessabi and O. Mercan. Phase and amplitude error indices for error quantification in pseudo dynamic testing. *Earthquake Engineering & Structural Dynamics*, 41(10): 1347–1364, 2012.

[104] S. J. Dyke, B. F. Spencer Jr, P. Quast, D. C. Kaspari, and M. K. Sain. Implementation of an active mass damper using acceleration feedback control. *Microcomputers in Civil Engineering*, 11(5):305–323, 1996.

[105] B. F. Spencer Jr, M. K. Sain, C. Won, D. C. Kaspari, and P. M. Sain. Reliability-based measures of structural control robustness. *Structural Safety*, 15(1):111–129, 1994.

[106] G. Takács and B. Rohal'-Ilkiv. *Model predictive vibration control: efficient constrained MPC vibration control for lightly damped mechanical structures.* Springer Science and Business Media, London, UK, 2012.

[107] D. Ariens, B. Houska, H. Ferreau, and F. Logist. ACADO: Toolkit for automatic control and dynamic optimization. *Optimization in Engineering Center (OPTEC)*, 2014.

[108] B. Houska, H. J. Ferreau, and M. Diehl. An auto-generated real-time iteration algorithm for nonlinear MPC in the microsecond range. *Automatica*, 47(10):2279–2285, 2011.

[109] H. J. Ferreau, C. Kirches, A. Potschka, H. G. Bock, and M. Diehl. qpOASES: A parametric active-set algorithm for quadratic programming. *Mathematical Programming Computation*, 6(4):327–363, 2014.

[110] A. A. Stoorvogel. *The H_∞ control problem: a state space approach*. University of Michigan, Ann Arbor, USA, 2000.

[111] J. C. Doyle, K. Glover, P. Khargonekar, and B. Francis. State space solutions to standard H_2 and H_∞ control problems. *IEEE Transactions on Automatic Control*, 34(8):831–847, 1989.

[112] P. Apkarian, L. Ravanbod-Hosseini, and D. Noll. Time domain constrained H_∞ synthesis. *International Journal of Robust and Nonlinear Control*, 21(2):197–217, 2011.

[113] P. E. Orukpe, I. M. Jaimoukha, and H. M. El-Zobaidi. Model predictive control based on mixed H_2/H_∞ control approach. *Proceedings of the 2007 American Control Conference*, pages 6147–6150. IEEE, 2007.

[114] H. Chen, P. Y. Sun, and K. H. Guo. Constrained H_∞ control of active suspensions: an LMI approach. *Proceedings of the 2002 International Conference on Control and Automation*, pages 157–157. IEEE, 2002.

[115] K. Morris and S. Yang. Comparison of actuator placement criteria for control of structures. *Journal of Sound and Vibration*, 352(1):1–18, 2015.

[116] M. I. Frecker. Recent advances in optimization of smart structures and actuators. *Journal of Intelligent Material Systems and Structures*, 14(4):207–216, 2003.

[117] S. L. Padula and R. K. Kincaid. *Optimization strategies for sensor and actuator placement*. National Aeronautics and Space Administration Langley Research Center, Langley, Virginia, 1985.

[118] P. Skrzypczynski. Simultaneous localization and mapping: A feature-based probabilistic approach. *International Journal of Applied Mathematics and Computer Science*, 19(4): 575–588, 2009.

[119] D. Pazderski, K. Kozlowski, and W. E. Dixon. Tracking and regulation control of a skid steering vehicle. *Proceedings of the 10^{th} International Topical Meeting on Robotics and Remote Systems*, pages 369–376. American Nuclear Society, 2004.

[120] H. Wang, J. Zhang, J. Yi, D. Song, S. Jayasuriya, and J. Liu. Modeling and motion stability analysis of skid-steered mobile robots. *Proceedings of the 2009 International Conference on Robotics and Automation*, pages 4112–4117. IEEE, 2009.

[121] K. Kozlowski and D. Pazderski. Modeling and control of a 4-wheel skid-steering mobile robot. *International Journal of Applied Mathematics & Computer Science*, 14(4):477–496, 2004.

[122] S. N. Dermitzakis and S. A. Mahin. *Development of substructuring techniques for on-line computer controlled seismic performance testing*. Report UBC/EERC-85/04, Earthquake Engineering Research Center, University of California, Berkeley, CA., 1985.

[123] M. Nakashima, M. Kato, and E. Takaoka. Development of real-time pseudo-dynamic testing. *Earthquake Engineering & Structural Dynamics*, 21(1):14, 1992.

[124] T. Horiuchi, M. Inoue, T. Konno, and Y. Namita. Real-time hybrid experimental system with actuator delay compensation and its application to a piping system with energy absorber. *Earthquake Engineering & Structural Dynamics*, 28(10):1121–1141, 1999.

[125] O. Mercan and J. M. Ricles. Experimental studies on real-time testing of structures with elastomeric dampers. *Journal of Structural Engineering*, 135(9):1124–1133, 2009.

[126] J. E. Carrion, B. F. Spencer Jr, and B. M. Phillips. Real-time hybrid simulation for structural control performance assessment. *Earthquake Engineering & Engineering Vibration*, 8(4): 481–492, 2009.

[127] R. Christenson, Y. Z. Lin, A. Emmons, and B. Bass. Large-scale experimental verification of semi-active control through real-time hybrid simulation. *Journal of Structural Engineering*, 134(4):522–534, 2008.

[128] National Instruments. *FPGA fundamentals*. NI White Papers, 2018. URL http://www.ni.com/white-paper/55015/en/.

[129] A. Blakeborough, M. S. Williams, A. P. Darby, and D. M. Williams. The development of real-time substructure testing. *Philosophical Transactions of the Royal Society of London*, 359(1):1869–1891, 2001.

[130] H. M. Hilber, T. J. R. Hughes, and R. L. Taylor. Improved numerical dissipation for time integration algorithms in structural dynamic. *Earthquake Engineering & Structural Dynamics*, 5(3):283–292, 1977.

[131] N. M. Newmark. A method of computation for structural dynamics. *Journal of Engineering Mechanics*, 85:67–94, 1959.

[132] Y. Liu, K. Goorts, A. Ashasi-Sorkhabi, O. Mercan, and S. Narasimhan. A state space-based explicit integration method for real-time hybrid simulation. *Structural Control & Health Monitoring*, 23(4):641–658, 2016.

[133] Y. F. Zhang, R. Sause, J. M. Ricles, and C. J. Naito. Modified predictor-corrector numerical scheme for real-time pseudo dynamic tests using state-space formulation. *Earthquake Engineering & Structural Dynamics*, 34(3):271–288, 2005.

[134] M. L. Brodersen, G. Ou, J. Hogsberg, and S. J. Dyke. Analysis of hybrid viscous damper by real-time hybrid simulations. *Engineering Structures*, 126(1):675–688, 2016.

[135] A. Ashasi-Sorkhabi, K. Goorts, O. Mercan, and S. Narasimhan. Mitigating pedestrian bridge motions using a deployable autonomous control system. *Journal of Bridge Engineering*, 24(1):04018101, 2018.

[136] T. L. Karavasilis, J. M. Ricles, R. Sause, and C. Chen. Experimental evaluation of the seismic performance of steel MRFs with compressed elastomer dampers using large-scale real-time hybrid simulation. *Engineering Structures*, 33(6):1859–1869, 2011.

[137] F. Zhu, J. T. Wang, F. Jin, and L. Q. Lu. Seismic performance of tuned liquid column dampers for structural control using real-time hybrid simulation. *Journal of Earthquake Engineering*, 20(8):1370–1390, 2016.

[138] J. O'Callahan. System equivalent reduction expansion process (SEREP). *Proceedings of the 7^{th} International Modal Analysis Conference*, pages 29–37. Union College, 1989.

[139] G. J. Balas and J. C. Doyle. Robust control of flexible modes in the controller crossover region. *AIAA Journal of Guidance, Dynamics and Control*, 17(2):370–377, 1994.

[140] R. Lind, G. J. Balas, and A. K. Packard. Evaluating DK iteration for control design. *Proceedings of the 1994 American Control Conference*, pages 2792–2797. IEEE, 1994.

[141] A. N. Moser. Designing controllers for flexible structures with H_∞/μ-synthesis. *IEEE Control Systems*, 13(2):79–89, 1993.

[142] M. R. Bai and W. Liu. Control design of active vibration isolation using μ-synthesis. *Journal of Sound and Vibration*, 257(1):157–175, 2002.

[143] J. Blanchard, B. L. Davies, and J. W. Smith. Design criteria and analysis for dynamic loading of footbridges. *Proceedings of the 1977 Symposium on Dynamic Behaviour of Bridges*, pages 90–106. Transport and Road Research Laboratory Report No. 275, 1977.

[144] J. O. Smith. *Introduction to Digital Filters with Audio Applications*. W3K Publishing, 2007.

APPENDICES

Appendix A

List of Publications

The following is a list of journal publications and conference papers resulting from this work contained in this thesis:

Publications in Referred Journals:

- **K. Goorts** and S. Narasimhan. Adaptive model predictive control for deployable control systems with constraints. *Journal of Structural Engineering*. In Press, Accepted: Feb. 22, 2019.
- A. Ashasi-Sorkhabi, **K. Goorts**, O. Mercan, and S. Narasimhan. Mitigating pedestrian bridge motions using a deployable autonomous control system. *Journal of Bridge Engineering*. 24(1): 04018101, 2019.
- **K. Goorts** and S. Narasimhan. Adopting robotic systems to enhance vibration control of footbridges. *Structural Engineering International*. 28(4): 435-447, 2018.
- **K. Goorts**, S. Phillips, A. Ashasi-Sorkhabi, and S. Narasimhan. Structural control using a deployable autonomous control system. *International Journal of Intelligent Robotics and Applications*. 1(3): 306-326, 2017.
- **K. Goorts**, A. Ashasi-Sorkhabi, and S. Narasimhan. Deployable active mass dampers for vibration mitigation in lightweight bridges, *Journal of Structural Engineering*. 143(12): 04017159, 2017.

- Y. Liu, **K. Goorts**, A. Ashasi-Sorkhabi, O. Mercan, and S. Narasimhan. A state space-based explicit integration method for real-time hybrid simulation. *Structural Control and Health Monitoring*, 23(4):641-658, 2016

Conference Proceedings - Full paper

- **K. Goorts** and S. Narasimhan. Model predictive control for deployable, autonomous control systems. *Proceedings of the 7^{th} World Conference on Structural Control and Monitoring*, Qingdao, China, 2018.
- **K. Goorts** and S. Narasimhan. The role of control-structure interaction in deployable autonomous control systems. *Proceedings of the 36^{th} International Modal Analysis Conference (IMAC)*, Orlando, FL. USA, 2018
- **K. Goorts** and S. Narasimhan. Towards deployable, autonomous, vibration control systems for lightweight footbridges. *Proceedings of Footbridge Berlin 2017*, Berlin, Germany, 2017.
- **K. Goorts** and S. Narasimhan. Modeling and controller design for deployable autonomous control systems. *Proceedings of the 13^{th} International Workshop on Advanced Smart Materials and Smart Structures Technology*. Tokyo, Japan, 2017.

Publications under preparation:

- **K. Goorts** and S. Narasimhan. Addressing robustness in the controller formulation for deployable control systems. *Journal of Structural Engineering* (30-pages).

Appendix B

RTHS with spatially varying forces

This appendix summarizes the numerical substructuring approach presented in Ashasi-Sorkhabi et al. [135] to address spatially varying forces in RTHS. This framework was used to evaluate the performance of the prototype DACS in controlling a full-scale pedestrian bridge subjected to pedestrian loads.

B.1 Numerical substructuring framework

Consider a modular aluminum pedestrian bridge of length L which is to be modelled as the numerical substructure for RTHS. To handle spatially varying loads, the bridge is modelled in the modal domain such that each mode can be simulated separately. The bridge is assumed to remain in the linear elastic range under external loading such that superposition techniques can be used in the modal decomposition. The equation of motion for the n^{th} mode of the bridge response is given by:

$$m_n \ddot{y}_n(t) + c_n \dot{y}_n(t) + R_{a,n}(t) + R_{e,n}(t) = f_n(t) \tag{B.1}$$

where y_n, m_n, and c_n denote the modal displacement, mass, and damping of the n^{th} node respectively and f_n represents the corresponding modal force. $R_{a,n}$ and $R_{e,n}$ denote the modal restoring forces captured from the analytical substructure and experimental substructure respectively. Given the analytical substructure is assumed to remain linear elastic, the analytical restoring force is

proportional to the modal stiffness and can be written as:

$$R_{a,n}(t) = k_n y_n(t) \tag{B.2}$$

where k_n is the modal stiffness in the n^{th} mode. The experimental restoring force corresponding to the n^{th} mode is determined from the physical restoring force (R_e) measured in the experimental substructure according to:

$$R_{e,n}(t) = \int_0^L \delta(x - x_e)\varphi_n(x)R_e(t)dt \tag{B.3}$$

where φ_n denotes the n^{th} mode shape, δ is the Dirac delta function, x is the location measured along the length of the bridge, and x_e represents the location of the interface between the analytical and experimental substructures (i.e., location of the DACS on the bridge). Assuming the lateral component of the bridge dynamics behaves as a simply supported beam, the mode shapes can be idealized as:

$$\varphi_n(x) = \sin\left(\frac{n\pi x}{L}\right) \tag{B.4}$$

Substituting Equations B.2, B.3, and B.4 into Equation B.1 yields the following equation of motion for a given mode:

$$m_n\ddot{y}_n(t) + c_n\dot{y}_n(t) + k_n y_n(t) + R_e(t)\sin\left(\frac{n\pi x_e}{L}\right) = f_n(t) \tag{B.5}$$

Expressing the modal equation of motion in state-space yields:

$$\dot{\boldsymbol{z}}_n(t) = \mathbf{A}_n\boldsymbol{z}_n(t) + \mathbf{B}_n\left[f_n(t)\,,\ R_e\sin\left(\frac{n\pi x_e}{L}\right)\right]^T \tag{B.6a}$$

$$y_n(t) = \mathbf{C}_n\boldsymbol{z}_n(t) + \mathbf{D}_n\left[f_n(t)\,,\ R_e\sin\left(\frac{n\pi x_e}{L}\right)\right]^T \tag{B.6b}$$

where the state vector $\dot{\boldsymbol{z}}_n = \left[y_n(t)\ \dot{y}_n(t)\right]^T$ and the state, input, output, and feed-through matrices are given by:

$$\mathbf{A}_n = \begin{bmatrix} 0 & 1 \\ \frac{-k_n}{m_n} & \frac{-c_n}{m_n} \end{bmatrix}\ ,\ \mathbf{B}_n = \begin{bmatrix} 0 & 0 \\ \frac{1}{m_n} & \frac{-1}{m_n} \end{bmatrix}\ ,\ \mathbf{C}_n = \begin{bmatrix} 1 & 0 \end{bmatrix}\ ,\ \mathbf{D}_n = \begin{bmatrix} \mathbf{0} \end{bmatrix} \tag{B.7}$$

Notice the output of interest in this framework is the modal displacement such that the physical displacement can be determined through superposition and applied to the experimental substructure.

The discrete state space formulation (DSSF) presented in Liu et al. [132] is adopted for implementation purposes. Assuming an integration time step of T and setting $t_0 = kT$, $t = (k+1)T$, the (DSSF) is given by:

$$\dot{\boldsymbol{z}}_n[(k+1)T] = \mathbf{A}_{d,n}\boldsymbol{z}_n[kT] + \mathbf{B}_{d,n}\left[f_n[kT]\,,\ R_{e,n}[kT]\right]^T \tag{B.8a}$$

$$y_n[kT] = \mathbf{C}_{d,n}\boldsymbol{z}_n[kT] + \mathbf{D}_{d,n}\left[f_n[kt]\,,\ R_{e,n}[kT]\right]^T \tag{B.8b}$$

where $\mathbf{A}_{d,n}$, $\mathbf{B}_{d,n}$, $\mathbf{C}_{d,n}$, and $\mathbf{D}_{d,n}$ are the discrete system matrices for the n^{th} mode.

The procedure is repeated for all vibrational modes considered during RTHS. Within each iteration (i.e., time step), the computed modal state vectors are combined using the corresponding mode shape functions to obtain the physical response along the bridge. The computed displacement at the location of the control device can then be issued to the experimental substructure.

B.2 Pedestrian load modelling

Given the bridge is modelled in the modal domain, spatially varying loads such as walking pedestrians can be included in the simulation. Consider the following Fourier series pedestrian load model for simulating forces induced by walking pedestrians [143]:

$$F(t) = F_0 + \sum_{i=1}^{n} w_p \alpha_i \sin\left(2\pi i f_s t + \psi_i\right) \tag{B.9}$$

where w_p and f_s denote the pedestrian weight and step frequency respectively, α_i and ψ_i are the dynamic load factor and phase for the i^{th} harmonic and F_0 is the mean lateral force. Given the load model, the n^{th} modal force is given by:

$$f_n(t) = \int_0^L \delta\left(x - vt\right)\psi_n(x)F(t)dx \tag{B.10}$$

where v denotes he pedestrian speed. If the pedestrian is assumed to move at a constant speed, the term vt represents the pedestrian's location on the bridge at any time t. Furthermore, given the mode shapes in Equation B.4, the pedestrian load for the n^{th} mode can be expressed as:

$$f_n(t) = F(t)\sin\left(\frac{n\pi vt}{L}\right) \tag{B.11}$$

Appendix C

Relevant Formulations

C.1 State estimation using Kalman filtering

In many applications of state-feedback control, the states of the system are not readily available and must be estimated. The Kalman filter, first published in Kalman [37], addresses the problem of estimating the state vector z_k given knowledge of the following linear discrete time process:

$$z_k = \mathbf{A}_{k-1} z_{k-1} + \mathbf{B}_{k-1} \boldsymbol{u}_{k-1} + \boldsymbol{\omega}_{k-1} \tag{C.1}$$

and measurements of the system given by:

$$\boldsymbol{y}_k = \mathbf{C}_k z_k + \mathbf{D}_k \boldsymbol{u}_k + \boldsymbol{\nu}_k \tag{C.2}$$

The matrices $\mathbf{A}_{k-1}$, $\mathbf{B}_{k-1}$, $\mathbf{C}_k$, and $\mathbf{D}_k$ contain the discrete time system equations and $\boldsymbol{u}_k$ is the input vector at the k^{th} time step. The process noise $\boldsymbol{\omega}_k$ and measurement noise $\boldsymbol{\nu}_k$ are assumed to be zero mean, white, uncorrelated, and have known covariances of $\mathbf{Q}_k$ and $\mathbf{R}_k$ respectively. The Kalman filter uses a two-step prediction-correction scheme. As such, define the following two estimates of the state vector z_k:

$$\hat{z}_{k|k-1} = E\left[z_k | \boldsymbol{y}_1, \boldsymbol{y}_1, \ldots, \boldsymbol{y}_{k-1}\right] \tag{C.3a}$$

$$\hat{z}_{k|k} = E\left[z_k | \boldsymbol{y}_1, \boldsymbol{y}_1, \ldots, \boldsymbol{y}_{k-1}, \boldsymbol{y}_k\right] \tag{C.3b}$$

where $\hat{z}_{k|k-1}$ and $\hat{z}_{k|k}$ are known as the *a priori* and *a posteriori* estimates respectively and the corresponding *a priori* and *a posteriori* estimate errors are defined by:

$$\epsilon_{k|k-1} = z_k - \hat{z}_{k|k-1} \tag{C.4a}$$

$$\epsilon_{k|k} = z_k - \hat{z}_{k|k} \tag{C.4b}$$

It follows that the covariance of the estimation errors $\mathbf{P}_{k|k-1}$ and $\mathbf{P}_{k|k}$ are given by:

$$\mathbf{P}_{k|k-1} = E\left[\left(z_k - \hat{z}_{k|k-1}\right)\left(z_k - \hat{z}_{k|k-1}\right)^T\right] \tag{C.5a}$$

$$\mathbf{P}_{k|k} = E\left[\left(z_k - \hat{z}_{k|k}\right)\left(z_k - \hat{z}_{k|k}\right)^T\right] \tag{C.5b}$$

The *a priori* state estimate propagates with time according to:

$$\hat{z}_{k|k-1} = \mathbf{A}_{k-1}\hat{z}_{k-1|k-1} + \mathbf{B}_{k-1}\boldsymbol{u}_{k-1} \tag{C.6}$$

which is referred to as the prediction update. By computing the *a priori* state estimation error with the estimate $\hat{z}_{k|k-1}$, it follows that the expectation in Equation C.5a becomes:

$$\mathbf{P}_{k|k-1} = \mathbf{A}_{k-1}\mathbf{P}_{k-1|k-1}\mathbf{A}_{k-1}^T + \mathbf{Q}_{k-1} \tag{C.7}$$

The *a posteriori* state estimate is determined based on a weighted residual – often referred to as innovation – which is defined by the difference between the actual measurement $\boldsymbol{y}_k$ and the measurement predicted by the *a priori* state estimate.

$$\hat{z}_{k|k} = \hat{z}_{k|k-1} + \mathbf{K}_k\left[\boldsymbol{y}_k - \left(\mathbf{C}_k\hat{z}_{k|k-1} + \mathbf{D}_k\boldsymbol{u}_k\right)\right] \tag{C.8}$$

where the weighting or gain matrix $\mathbf{K}_k$ is determined by minimizing the *a posteriori* error covariance in Equation C.5b and thus computed as:

$$\mathbf{K}_k = \mathbf{P}_{k|k-1}\mathbf{C}_k^T\left(\mathbf{C}_k\mathbf{P}_{k|k-1}\mathbf{C}_k^T + \mathbf{R}_k\right)^{-1} \tag{C.9}$$

Substituting this result into Equation C.5b leads to the *a posteriori* state estimate error covariance given by:

$$\mathbf{P}_{k|k} = \left(\mathbf{I} - \mathbf{K}_k\mathbf{C}_k\right)\mathbf{P}_{k|k-1} \tag{C.10}$$

The Kalman filter algorithm is summarized below:

Initialization:

$$\hat{z}_{0|0} = E\left[z_0\right] \tag{C.11a}$$

$$\mathbf{P}_{0|0} = E\left[\left(z_0 - \hat{z}_{0|0}\right)\left(z_0 - \hat{z}_{0|0}\right)^T\right] \tag{C.11b}$$

Prediction Step:

$$\hat{z}_{k|k-1} = \mathbf{A}_{k-1}\hat{z}_{k-1|k-1} + \mathbf{B}_{k-1}\boldsymbol{u}_{k-1} \tag{C.12a}$$

$$\mathbf{P}_{k|k-1} = \mathbf{A}_{k-1}\mathbf{P}_{k-1|k-1}\mathbf{A}_{k-1}^T + \mathbf{Q}_{k-1} \tag{C.12b}$$

Correction Step:

$$\mathbf{K}_k = \mathbf{P}_{k|k-1}\mathbf{C}_k^T\left(\mathbf{C}_k\mathbf{P}_{k|k-1}\mathbf{C}_k^T + \mathbf{R}_k\right)^{-1} \tag{C.13a}$$

$$\hat{z}_{k|k} = \hat{z}_{k|k-1} + \mathbf{K}_k\left[\boldsymbol{y}_k - \left(\mathbf{C}_k\hat{z}_{k|k-1} + \mathbf{D}_k\boldsymbol{u}_k\right)\right] \tag{C.13b}$$

$$\mathbf{P}_{k|k} = \left(\mathbf{I} - \mathbf{K}_k\mathbf{C}_k\right)\mathbf{P}_{k|k-1} \tag{C.13c}$$

C.2 Minimum-phase / all-pass filter decomposition

A linear, time-invariant system is said to be minimum-phase if the system and its inverse are causal and stable. Thus, all poles and zeros of a minimum phase system are contained in the closed left-half plane. Every causal stable system $H(s)$ with no zeros on the origin can be factored into a minimum-phase system in cascade with a causal stable all-pass system [144]:

$$H(s) = H_{min}(s)H_{ap}(s) \tag{C.14}$$

where H_{min} is minimum phase and H_{ap} is a stable all-pass filter. This can be shown by induction. Consider a single zero ζ on the right-half plane of $H(s)$. Factoring out the unstable zero yields:

$$H(s) = H_1(s)\,(1 - \zeta s) \tag{C.15}$$

The goal is to reflect the unstable zero onto the left-half plane. Thus, multiplying by

$$1 = \frac{(1 + \zeta s)}{(1 + \zeta s)} \tag{C.16}$$

gives

$$H(s) = \underbrace{H_1(s)\,(1 + \zeta s)}_{\textit{minimum phase}} \underbrace{\frac{(1 - \zeta s)}{(1 + \zeta s)}}_{\textit{all-pass}} \tag{C.17}$$

Thus, $H(s)$ has been decomposed into the product of a minimum-phase system and stable all-pass filter. This procedure can be repeated for each unstable zero in $H(s)$. In summary, when decomposing a stable, causal system, the resulting minimum-phase system will contain all stable poles and zeros of the original system (i.e., poles and zeros on the left-half plane) as well as the conjugate of any zeros in the original system that lie in the right-half plane. The all-pass filter will contain the original unstable zeros and poles at the location of each reflected zero. An important property of this decomposition is that the amplitude response of $H(s)$ is preserved entirely in the minimum phase system; however, recovering the phase of $H(s)$ requires the all-pass filter. Nevertheless, this decomposition is commonly used to estimate a stable, and causal inverse of $H(s)$ where the inverse is approximated using the inverse of the minimum phase system.

The above induction applies directly when $H(s)$ is a proper transfer function where the relative degree between the order of the numerator polynomial and order of the denominator polynomial

is zero (i.e., the number of zeros equals the number of poles). For the special case when $H(s)$ is strictly proper (i.e., the number of zeros is less than the number of poles), following the same approach will yield a strictly-proper minimum-phase component that by definition is not a minimum phase system since the inverse is an improper transfer function and thus non-causal. Nevertheless, all poles and zeros of the minimum-phase component are stable (i.e., within the left-half plane) and thus a stable and casual inverse can be obtained by adding a low-pass filter. Consider the following illustrative example for a strictly-proper system $H(s)$:

Given

$$H(s) = \frac{(s-1)(s+2)}{(s+3)(s+4)(s+5)} \tag{C.18}$$

factoring out the unstable zero at $s = 1$ gives:

$$H(s) = \frac{(s+2)}{(s+3)(s+4)(s+5)} \quad (s-1) \tag{C.19}$$

and multiplying by $1 = \frac{(s+1)}{(s+1)}$ yields:

$$H(s) = \underbrace{\frac{(s+1)(s+2)}{(s+3)(s+4)(s+5)}}_{\textit{minimum-phase component}} \quad \underbrace{\frac{(s-1)}{(s+1)}}_{\textit{all-pass filter}} \tag{C.20}$$

As shown, the minimum phase component of $H(s)$ is a strictly-proper system which leads to a non-causal inverse. To approximate $H^{-1}(s)$, a first-order low-pass filter with frequency cut-off ω_c is appended to the inverse of the minimum-phase component:

$$H^{-1}(s) = \frac{(s+3)(s+4)(s+5)}{(s+1)(s+2)} \quad \frac{\omega_c}{(s+\omega_c)} \tag{C.21}$$

C.3 Linear fractional transformations

A linear fractional transformation (LFT) is defined as a mapping $F : \mathbb{C} \mapsto \mathbb{C}$ of the form

$$F(s) = \frac{a + bs}{c + ds} \tag{C.22}$$

where a, b, c, and $d \in \mathbb{C}$. LFTs of this form can be generalized for the matrix case [53]. Consider the complex matrix $\mathbf{M}$ partitioned as:

$$\mathbf{M} = \begin{bmatrix} \mathbf{M}_{11} & \mathbf{M}_{12} \\ \mathbf{M}_{21} & \mathbf{M}_{22} \end{bmatrix} \in \mathbb{C}^{(p_1+p_2)\times(q_1+q_2)} \tag{C.23}$$

and let $\Delta_\ell \in \mathbb{C}^{q_2\times p_2}$ and $\Delta_u \in \mathbb{C}^{q_1\times p_1}$ be two other complex matrices. The *lower* LFT with respect to Δ_ℓ is defined as the map:

$$\mathcal{F}_\ell(\mathbf{M}, \bullet) : \mathbb{C}^{q_2\times p_2} \mapsto \mathbb{C}^{p_1\times q_1} \tag{C.24}$$

with

$$\mathcal{F}_\ell(\mathbf{M}, \Delta_\ell) = \mathbf{M}_{11} + \mathbf{M}_{12}\Delta_\ell \left(\mathbf{I} - \mathbf{M}_{22}\Delta_\ell\right)^{-1} \mathbf{M}_{21} \tag{C.25}$$

Similarly, the *upper* LFT with respect to Δ_u is defined as:

$$\mathcal{F}_u(\mathbf{M}, \bullet) : \mathbb{C}^{q_1\times p_1} \mapsto \mathbb{C}^{p_2\times q_2} \tag{C.26}$$

with

$$\mathcal{F}_\ell(\mathbf{M}, \Delta_\ell) = \mathbf{M}_{22} + \mathbf{M}_{21}\Delta_u \left(\mathbf{I} - \mathbf{M}_{11}\Delta_u\right)^{-1} \mathbf{M}_{12} \tag{C.27}$$

The *lower* and *upper* LFTs are represented graphically in Figure C.1. From the diagrams it becomes clear that $\mathcal{F}_\ell(\mathbf{M}, \Delta_\ell)$ and $\mathcal{F}_u(\mathbf{M}, \Delta_u)$ are transformations obtained from closing the *lower* and *upper* loops of the matrix $\mathbf{M}$ respectively. As such, the *lower* LFT represents the following set of equations:

$$\begin{bmatrix} \boldsymbol{z}_1 \\ \boldsymbol{y}_1 \end{bmatrix} = \begin{bmatrix} \mathbf{M}_{11} & \mathbf{M}_{12} \\ \mathbf{M}_{21} & \mathbf{M}_{22} \end{bmatrix} \begin{bmatrix} \boldsymbol{\omega}_1 \\ \boldsymbol{u}_1 \end{bmatrix} \tag{C.28a}$$

$$\boldsymbol{u}_1 = \Delta_\ell \boldsymbol{y}_1 \tag{C.28b}$$

while the *upper* LFT represents:

$$\begin{bmatrix} \boldsymbol{y}_2 \\ \boldsymbol{z}_2 \end{bmatrix} = \begin{bmatrix} \mathbf{M}_{11} & \mathbf{M}_{12} \\ \mathbf{M}_{21} & \mathbf{M}_{22} \end{bmatrix} \begin{bmatrix} \boldsymbol{u}_2 \\ \boldsymbol{\omega}_2 \end{bmatrix} \tag{C.29a}$$

$$\boldsymbol{u}_2 = \Delta_u \boldsymbol{y}_2 \tag{C.29b}$$

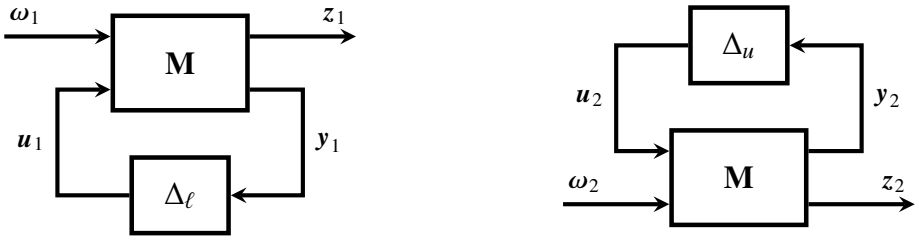

(a) *lower* LFT (b) *upper* LFT

Figure C.1: Block diagram representations of matrix linear fractional transformations

C.4 Robust controller synthesis using D-K iterations

Consider the generalized plant model in Figure C.2.

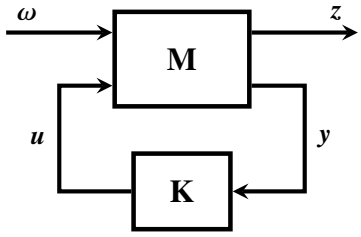

Figure C.2: Generalized plant model for robust controller synthesis

Designing a controller $\mathbf{K}$ for either robust stability, robust performance, or both, leads to the following μ-synthesis problem [53]:

$$\min_{\mathbf{K}} \|\mathcal{F}_\ell(\mathbf{M}, \mathbf{K})\|_\mu \tag{C.30}$$

The D-K iteration method yields a reasonable estimate of μ by iteratively solving for $\mathbf{K}$ and $\mathbf{D}$ in the following:

$$\min_{\mathbf{K}} \inf_{\mathbf{D},\mathbf{D}^{-1}\in H_\infty} \left\|\mathbf{D}\mathcal{F}_\ell(\mathbf{M}, \mathbf{K})\mathbf{D}^{-1}\right\|_\infty \tag{C.31}$$

where $\mathbf{D}$ is a minimum phase scaling matrix. For a fixed scaling transfer matrix $\mathbf{D}$, the expression

$$\min_{\mathbf{K}} \left\|\mathbf{D}\mathcal{F}_\ell(\mathbf{M}, \mathbf{K})\mathbf{D}^{-1}\right\|_\infty \tag{C.32}$$

is a standard H_∞ optimization problem. On the other hand, given a stabilizing controller $\mathbf{K}$,

$$\inf_{\mathbf{D},\mathbf{D}^{-1}\in H_\infty} \left\|\mathbf{D}\mathcal{F}_\ell(\mathbf{M}, \mathbf{K})\mathbf{D}^{-1}\right\|_\infty \tag{C.33}$$

is a standard convex optimization problem and can be solved point-wise in the frequency domain as

$$\sup_{\omega} \inf_{\mathbf{D}_\omega\in\mathcal{D}} \bar{\sigma}\left[\mathbf{D}_\omega\mathcal{F}_\ell(\mathbf{M}, \mathbf{K})(j\omega)\mathbf{D}_\omega^{-1}\right] \tag{C.34}$$

D-K iterations involve sequentially solving this two-parameter minimization. More specifically, each iteration involves minimizing over $\mathbf{K}$ with $\mathbf{D}_\omega$ fixed and subsequently minimizing point-wise over $\mathbf{D}_\omega$ with $\mathbf{K}$ fixed. A summary of the key steps is provided below [53]:

Overview of D-K iteration method:

1. Determine an initial estimate of the scaling matrix $\mathbf{D}_\omega$ point-wise across frequency.

2. Find scalar transfer functions $d_i(s), d_i^{-1}(s) \in \mathcal{R}H_\infty$ for $i = 1, 2, \ldots, (n-1)$ where n is the dimension of $\mathbf{M}$. This can be achieved using interpolation theory or graphical matching.

3. Let
$$\mathbf{D}(s) = \text{diag}\,(d_1(s)\mathbf{I}, \ldots, d_{n-1}(s)\mathbf{I}, \mathbf{I})$$
Construct a state space model for the system:
$$\hat{\mathbf{M}}(s) = \begin{bmatrix} \mathbf{D}(s) & \\ & \mathbf{I} \end{bmatrix} \mathbf{M}(s) \begin{bmatrix} \mathbf{D}^{-1}(s) & \\ & \mathbf{I} \end{bmatrix}$$

4. Solve an H_∞-optimization problem to minimize
$$\left\| \mathcal{F}_\ell(\hat{\mathbf{M}}, \mathbf{K}) \right\|_\infty$$
over all stabilizing $\mathbf{K}$'s. Note that a scaled version of $\mathbf{M}$ is used in this optimization and let the minimizing controller be denoted by $\hat{\mathbf{K}}$.

5. Minimize over $\mathbf{D}_\omega$ point-wise across frequency:
$$\bar{\sigma}\left[\mathbf{D}_\omega \mathcal{F}_\ell(\mathbf{M}, \hat{\mathbf{K}})(j\omega) \mathbf{D}_\omega^{-1} \right]$$
Note that this evaluation uses the minimizing $\hat{\mathbf{K}}$ from the previous step but that $\mathbf{M}$ is unscaled. This minimization leads to a new scaling function denoted by $\hat{\mathbf{D}}_\omega$.

6. Compare $\hat{\mathbf{D}}_\omega$ with the previous estimate $\mathbf{D}_\omega$. If they are within a specified tolerance, the iteration concludes, otherwise the initial estimate for $\mathbf{D}_\omega$ is set to $\hat{\mathbf{D}}_\omega$ and the iteration repeats from step 2.

For implementation purposes, the Robust Control toolbox in MATLAB includes the function *dksyn* which automates the D-K iterations.